Title
Coupled Multiscale Modeling of Aortic Valve Tissue

Author
Bakhaty, Ahmed

Publication Date
2018

Peer reviewed|Thesis/dissertation

Coupled Multiscale Modeling of Aortic Valve Tissue

by

Ahmed A Bakhaty

A dissertation submitted in partial satisfaction of the

requirements for the degree of

Doctor of Philosophy

in

Engineering - Civil and Environmental Engineering

and the Designated Emphasis

in

Computational Science and Engineering

in the

Graduate Division

of the

University of California, Berkeley

Committee in charge:

Professor Sanjay Govindjee, Chair
Professor Mohammad Mofrad
Professor Robert Taylor

Spring 2018

Coupled Multiscale Modeling of Aortic Valve Tissue

Abstract

Coupled Multiscale Modeling of Aortic Valve Tissue

by

Ahmed A Bakhaty

Doctor of Philosophy in Engineering - Civil and Environmental Engineering

University of California, Berkeley

Professor Sanjay Govindjee, Chair

Recent studies have uncovered the pivotal role that valvular interstitial cells play in the aortic valve system. The valvular interstitial cells regulate the extracellular matrix, maintain homeostasis, and modulate pathology, among other vital functions. The inherent connection between the aortic valve as an organ and its constituent cells may explain the shortcoming of traditional biomechanical modeling, particularly when the goal is to understand the cause, evolution, treatment, and prevention of disease.

Multiscale modeling of aortic valves has recently emerged, but is relatively nascent and much is missing from the literature. Most notably is the lack of a coupled multiscale model of the aortic valve, wherein the biomechanics of the aortic valve organ and its constituent cells impact one another. In this work, we investigate a novel multiscale approach to modeling aortic valve tissue that is coupled, i.e., biomechanical events occurring at disparate length scales are simultaneously captured.

We begin by presenting a model of aortic valve tissue that explicitly accounts for the collagen fibers that make up its microstructure and is consistent with experimental data. We then apply this model in an FE^2 (computational homogenization) framework to model the aortic valve tissue as an organ and its constituent valvular interstitial cells. We show the validity of such an approach and use it to argue the necessity of 3D multiscale modeling. Finally, we apply the multiscale model to a calcified aortic valve to study the mechanical behavior of the valvular interstitial cells in pathological tissue.

"The reason I'm here today is because I never gave up." -Future

Contents

List of Figures

List of Tables

Acknowledgments

First, I am grateful to my advisors, Professor Sanjay Govindjee and Professor Mohammad Mofrad, for all the knowledge, help, guidance, and most importantly, patience. None of this would have been possible otherwise.

Much of the analysis I have done over the last few years was done with FEAP, developed originally by Professor Robert Taylor. I am fortunate to have had his help with modifying the source code and have him on my dissertation committee.

Also, none of this would be possible without the rest of my qualifying examination committee: Professor Khalid Mosalam, Professor Shaofan Li, and Professor James Demmel. And of course, the countless other professors at Cal that taught me.

I am thankful for the assistance and support of the Govindjee Lab family and the Mofrad Lab family. I am also thankful for the handful of undergraduate research assistants that helped me implement little details here and there.

A special shout out to the fam that contributed one way or another to this long and arduous process.

Finally, thank you Maggie and Dr. Bakhaty, Sr.

Bles up.

Chapter 1

Introduction

We begin by introducing the physiology of the aortic valve (AV) system and discuss diseases and treatments. The emphasis of this chapter is on the application of computational modeling to AV tissue mechanics and we highlight models that link physical processes (multiphysics) and multiple length scales (multiscale) together. This chapter is not intended to be a comprehensive review of AVs and so we point the reader to a multitude of references throughout.

This chapter is organized as follows. First, we present an overview of heart valve function, disease, and existing treatment methods. Next, we discuss existing methods for modeling tissue mechanics which are primarily continuum models that do not explicitly consider cellular and molecular processes. We expand this discussion by including studies at the cellular and molecular scales and modeling that links the macro and micro-scales together. To contextualize these models, we present several applications related to identifying and treating diseased valves. Finally, we conclude with an outlook on future trends in the computational modeling of valve tissue.

1.1 Background

Heart valve disease is the cause of over 20,000 deaths per year in the United States alone [60]. This growing public health concern has prompted much research on heart valves, but the pathobiology of valve disorders is yet to be fully understood. Studies of the pathogenesis of valve disease have established a link between biomechanical events at the cellular and molecular scales with valve function at the organ and tissue scales [104, 168, 183]. Thus, understanding heart valve cellular and molecular biomechanics, and more importantly, their interaction with the organ and tissue scales, can lead to further advances in treatment and prevention measures for valve disease.

Experimental investigation at the cellular and molecular scales is, however, difficult, costly, and often impossible, particularly for *in vivo* studies. Alternatively, numerical simulation offers a way of simulating the native condition of heart valves, from the organ to the

molecular scale, in a cost-effective manner. Limitations in computational capabilities in the past have hindered the applicability of numerical simulation to heart valves, which exhibit inherently nonlinear and anisotropic material response, [146] distinct heterogeneous features at the various length scales, [139] and complex geometries that vary from person to person, over time, and with pathological conditions. With the advent of modern high-performance computing, it has become possible to simulate heart valve systems using fewer simplifying assumptions, and account for the interaction of the different processes and scales [80, 172]. These models can help further our understanding of valve disease and aid in developing novel treatment and prevention methods.

Because about 67% of heart valve disease is attributed to the aortic valve, [60] much of the effort dedicated to computational modeling of heart valves has been focused on the AV [32, 152]. In particular, there has been continued effort in characterizing the material response of the AV, as it is fundamental to capturing the physical response of the AV system.

1.2 Structure and function of the aortic valve

An understanding of the physiology and biomechanics of the AV is necessary to properly develop numerical models that properly represent AV tissue behavior. In this section, we present a brief summary of the structure and function of healthy and diseased AVs. We present this overview as a background on heart valves and restrict the discussion to features important to modeling valve tissue behavior. For further details on the biomechanics of heart valves, the reader is referred to the review by Sacks and Yoganathan [139].

Healthy aortic valves

Blood flow through the heart is controlled passively by four valves: the pulmonary valve between the right ventricle and pulmonary artery, the aortic valve between the left ventricle and the aorta, the tricuspid valve between the right ventricle and right atrium, and the mitral valve between the left ventricle and left atrium. These valves open and close in response to pressure changes to allow blood to flow between the chambers and prevent retrograde flow. During ventricular systole, the ventricles contract to increase the pressure, opening the AV and allowing blood to flow into the aorta. The ventricles relax during ventricular diastole when the pressure equilibrates, closing the AV. The closing of the valve is referred to as coaptation.

The AV has distinct biomechanical features and function at different length scales (Fig. 1.1). At the organ scale, a healthy AV consists of three leaflets, or cusps[1], that fully open and fully seal in response to blood pressure [83]. At the tissue scale, the valve leaflets are composed of three layers: the ventricularis, the spongiosa, and the fibrosa with a total combined thickness of 0.2-2.0 mm [146]. The fibrosa, comprised of an organized collagen structure, is the main load-bearing component. The ventricularis is the thinnest layer lining the inflow

[1]We use the term cusp and leaflet interchangeably throughout.

surface and it consists primarily of a dense network of collagen fibers and some elastin. In the middle is the gel-like spongiosa, composed of proteoglycans, which functions as a cushion to absorb the tension and friction between the two layers [73, 142]. and serves to resist fatigue in the leaflet under the cyclic flexural cyclic loading caused by opening and closing of the AV. At the cellular scale, two main cell types are embedded in the tissue matrix: interstitial cells, which are thought to be responsible for maintaining the matrix and modulating disease pathology [104] and endothelial cells, which line the blood-facing surfaces. At the molecular scale is a sponge-like fibrous matrix of elastin which surrounds bundles of collagen fiber [158]. Both collagen and elastin are kinked fibers that demonstrate large extension at low stresses until straightened, where they require large stresses for small extensions. Collagen is the main load-bearing component and elastin serves to return the collagen to its undeformed state [165].

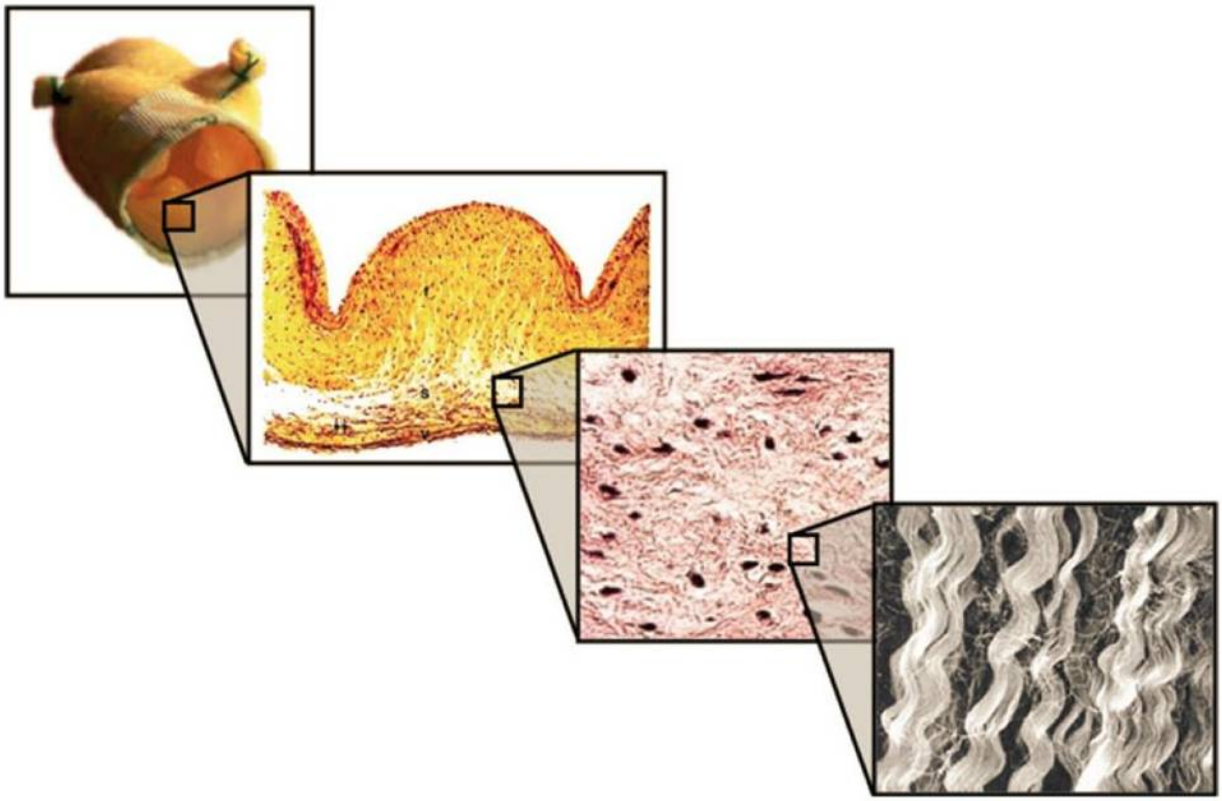

Figure 1.1: Representation of the multiscale nature of heart valve mechanics: organ-, tissue-, cell-, and molecular-scale features.[174]

The cardiac cycle results in large, cyclic deformation in heart valve tissue, whose structure is capable of withstanding the rapidly varying stress and strain states that persist throughout the lifetime of a healthy species. Diseased valves can develop different stress and strain states that can lead to fatal secondary complications, such as thromobosis [30, 87, 94, 147].

Consequently, identifying stress and strain states associated with a diseased valve can help in diagnosis and treatment.

Aortic valve disease and treatment

Valve pathology is inextricably linked to valve biomechanics. An understanding of the biomechanical function of the valve at different scales can potentially lead to effective management of valve disease. There are various diseases that impact the AV. The most common of them is aortic stenosis which affects about 0.4% of the US population and about 3% of those over 75 years of age [60]. It is characterized by the failure of the valve to fully open and it is attributed to age-related wear, rheumatic disease, and stiffening of the valve leaflets due to development of calcified nodes [59]. Aortic stenosis resulting from extensive calcification, known as calcific aortic stenosis (CAS), affects about 2% of the population over age 65 [103]., [126] Patients with symptomatic CAS are at risk for heart failure unless the calcified AV is replaced [18]. Other AV diseases include aortic regurgitation (when the AV does not fully close) and bicuspid AV (a congenital disease in which the AV has two leaflets instead of three [160]).

Approximately 40% of patients with severe aortic stenosis undergo valve replacement surgery and 10% undergo valve repair cardiothoracic surgeries [60]. The remainder do not undergo surgery due to perioperative risk, age, lack of symptoms, or refusal [8]. Recently, transcatheter AV replacement (TAVR) has come forward as a promising technique [7]. Computational methods can potentially improve techniques like this by monitoring tissue stresses in TAVR with inverse finite element modeling (i.e., computing the tissue stress state based on deformations measured from images) and the design of nano drug delivery devices [48].

1.3 Tissue-scale continuum modeling

There have been several efforts undertaken to characterize the mechanical properties of heart valve tissue using standard uniaxial, biaxial, and bending tests [27, 44, 114, 146, 166]. These experiments have demonstrated a distinct nonlinear, inhomogeneous, and anisotropic response of AV tissue. It is important (and arguably standard practice) to model the anisotropy of valve tissue leaflets [89]. In addition, experiments conducted at physiological strain rates demonstrated low levels of viscoelasticity that has rendered elastic constitutive models of valve tissue to be accepted [65].

Continuum mechanics provides a suitable framework for capturing the general stress-strain characteristics of valve tissue [76]. Hyperelastic models, in which the material stress is obtained by differentiating a strain energy function with respect to the current state of strain, are typically used:

$$\boldsymbol{S} = 2\frac{\partial W}{\partial \boldsymbol{E}}. \tag{1.1}$$

Strain energy functions are constructed by summing up elementary strain energy functions that account for the extracellular matrix (ECM) and fiber behavior, [56]

$$W = \sum_i W_i. \tag{1.2}$$

Once constructed, parameters are fit to experimental data to achieve the desired material response. For proper implementation into finite element (FE) methods, [153] these functions must also be numerically well behaved. This generally requires certain properties of the strain energy function to guarantee the existence of a nonlinear solution [13]. For computational efficiency, valve tissue is often modeled in FE simulations using shell elements [88, 129]., These elements, however, do not capture the through-thickness heterogeneity of the the tissue. A more detailed treatment of continuum mechanics theory and FE analysis is presented in Chapter 2.

Multilayer models at the tissue-scale have generally included only the fibrosa and ventricularis, as they bear the majority of the load [28]. The three leaflet layers have different compositions and mechanical properties, but they act as a single unit, resulting in the observed mechanical response. Experimental complications make it difficult to validate hypotheses regarding the mechanical function of the glycosaminoglycan (GAG)-rich spongiosa. To address this concern, Buchanan and Sacks [21] considered the addition of the spongiosa layer in the computational modeling of AV tissue mechanics. Their study suggests that the three layers function as a bonded structure in low-strain flexure, with physical sliding prohibited between the layers due to a large number of collagen fibers interconnecting the fibrosa and the ventricularis.

Exponential fiber stress functions are used to match the observed experimental response of valve tissue (Fig. 1.2a). This behavior is attributed to the lack of extensibility with increasing force as the collagen fibers become uncrimped. Fibers in the radial and circumferential directions exhibit remarkably distinct response (Fig. 1.2b), with a strong mechanical coupling between the two [139]. This behavior can be captured by accounting for the distribution, angle, and rotation of the fibers in the tissue layers [16].

These anisotropic properties are attributed to the collagen structure and alignment at the cellular and molecular scales [136]. It is hypothesized that this alignment is a result of contractile forces generated by the valvular interstitial cells (VICs), which express myofibroblast phenotype markers. [55, 149, 155, 164, 180] The mechanical loading, and subsequent change in the internal state of strain, triggers collagen fiber remodeling (synthesis and degradation) [15]. Driessen at al. developed a theory and computational model of valve tissue that accounts for this remodeling [39, 38, 40, 41]. This model assumes that collagen fibers align with the principal stretch directions. As the stretch increases, fibers rotate into alignment with the principal directions. The recruitment phenomenon is captured by a rate law that governs the evolution of collagen fibers. Since the mechanical properties of valve tissue are dependent on the collagen structure, type, thickness, orientation, and cross-linking, capturing the changes (i.e., remodeling) in the collagen fiber is important for obtaining the proper material response.

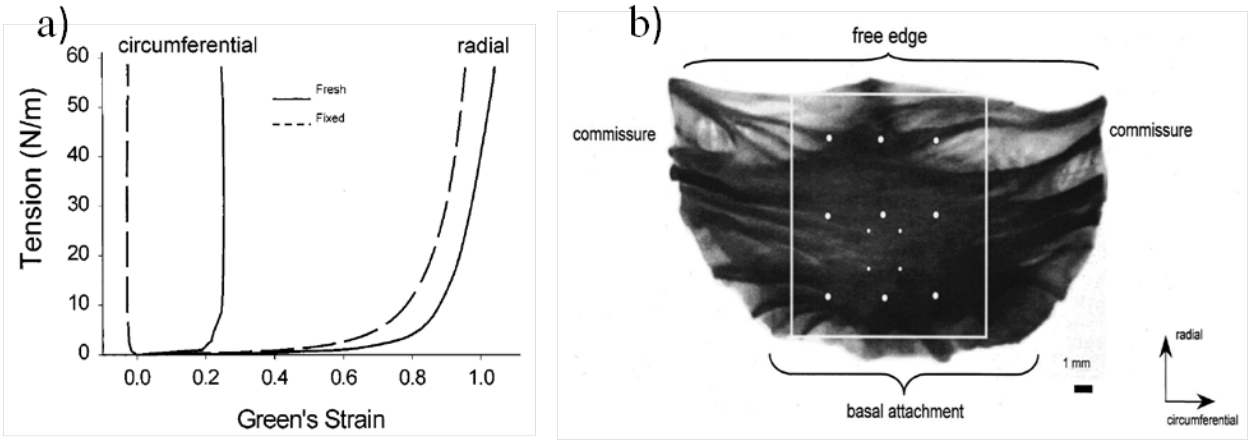

Figure 1.2: a) Representative circumferential and radial stress-strain curves demonstrating valve tissue anisotropy. b) AV cusp demonstrating fibrous structure and biaxial directions. The white circles indicate where strain measurements were taken by Billiar and Sacks [16]. Refer to Fig. 3.4 for a 3D representation of the cusp.

1.4 Aortic valve tissue modeling across multiple scales

The observed mechanical properties represented by the strain energy functions of the continuum models are a consequence of the microstructure, but macro-scale continuum models typically do not explicitly model the microstructure. They are sufficient for obtaining the aggregate macroscopic material response, but not for capturing microscopic mechanical events. In this section, we discuss the importance of biomechanical events occurring at the cellular and molecular scales and modeling that attempts to link them to the continuum tissue-scale models.

Valvular interstitial cells (VICs) have garnered attention recently due to their role in maintaining the leaflet tissue matrix and modulating disease pathology [98, 104]. VICs, characterized as myofibroblasts, exhibit a plastic and reversible phenotype, becoming activated and contractile in remodeling and diseased valves [130]. The behavior and role of VICs in healthy and diseased valves has prompted several experimental investigations to measure the mechanical behavior of VICs [26, 50, 115]. For instance, Liu et al. used atomic force microscopy (AFM) to quantify the elastic moduli of VICs [105] and Huang developed an elastic constitutive model [79].

Isolated VICs have been observed to respond to their mechanical environment and engage in cell-ECM communications [97, 123, 158]. These interactions are speculated to regulate tissue homeostasis, but the nature of these mechanisms is not yet understood. Computational models that account for these interactions can further our understanding of these mechanisms. For instance, a combined experimental-FE analysis revealed that the distribution of collagen fibers and VIC nuclei play a role in tissue stress mitigation [81]. This study is in line with other FE studies that demonstrated the dependence of tissue stress distribution on

the collagen fiber distribution, [89, 101, 106, 119], but differs from by including the VICs to clarify the force-transfer mechanism between the ECM and VICs.

Continuum models of the cells tend to be simplified, missing important aspects of the cellular structure. For instance, the filamentous structure of the cytoskeleton is not considered [84]. These fibers can be modeled, in a manner similar to the tissue models, to obtain more refined cellular behavior [163]. Another issue with continuum models is the representation of a continuous interface with the ECM. Studies have demonstrated that cells are attached to the ECM dynamically at discrete points known as focal adhesions [118, 158]. Modeling these discrete attachments (Fig. 1.3) is important for capturing the cell-ECM interactions properly. Alternatively, tensegrity models [84] can be used in treating the unit cell or the "representative volume element" (RVE). Tensegrity models capture the structure of the cytoskeleton by modeling the force transfer through the filaments by tensile elements and struts. This captures the discrete nature of the cellular structure.

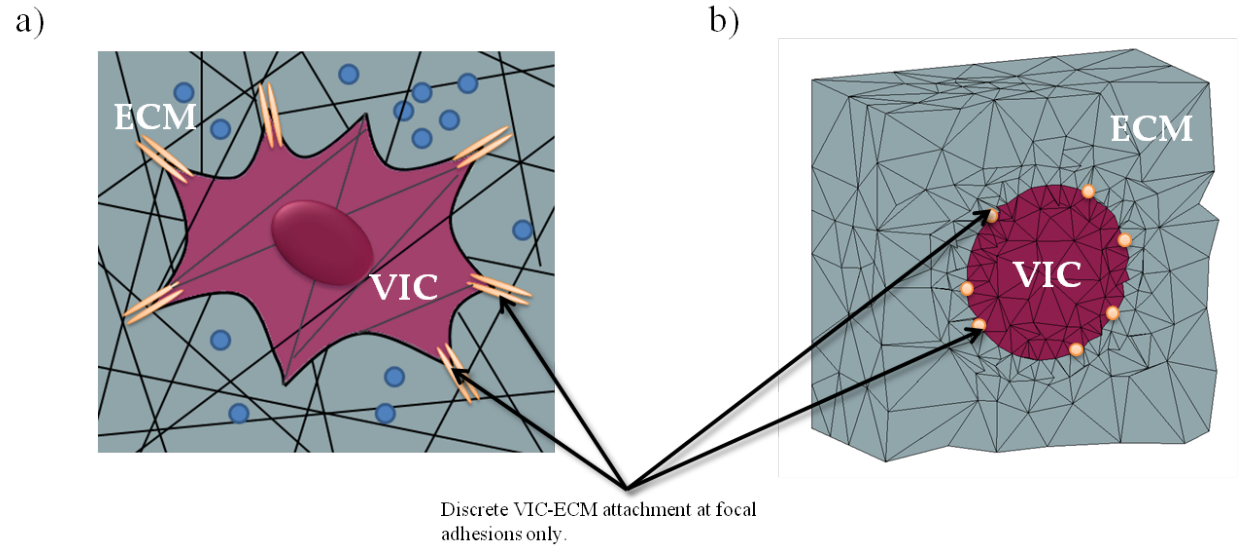

Figure 1.3: a) Cell attachment to substrate (ECM) at focal adhesions. b) Schematic of valvular interstitial cell (VIC) interface with extracellular matrix (ECM) in continuum model.

The process of cells responding to mechanical stimuli, and, in turn, initiating various cellular processes is known as mechanotransduction and it can underlie morphogenesis, differentiation, determination, development, and pathology [90]. At the molecular and atomic scales, continuum modeling is not appropriate due to the discrete and stochastic nature of the chemical interactions. The interactions of atoms in proteins, and other biomolecules, are computed with molecular dynamics (MD). Application of these models in heart valve biomechanics is still a work in progress, but similar studies with direct applications exist [128, 133, 140]. One significant challenge is linking molecular scale simulation with continuum modeling. The core of the challenge lies in efficiently reconciling the disparate time and length

scales involved in the nanoscale molecular dynamics of the biochemical processes with the macroscopic mechanics [85, 187].

Multiscale models that link valve tissues to VICs have recently emerged [35]. Weinberg and Mofrad developed a 3D AV model that combined organ, tissue, and cellular scales [172]. Kinematic results computed at the larger scales were passed down as boundary conditions to the successive smaller scale, allowing organ scale events to be translated to VIC deformations (Fig. 1.4). This model was further applied to study aging and calcification of the AV [23]. The model did not, however, translate cellular scale events to tissue response. It is important to extend this model to account for the bidirectional communication to achieve true multiscale coupling.

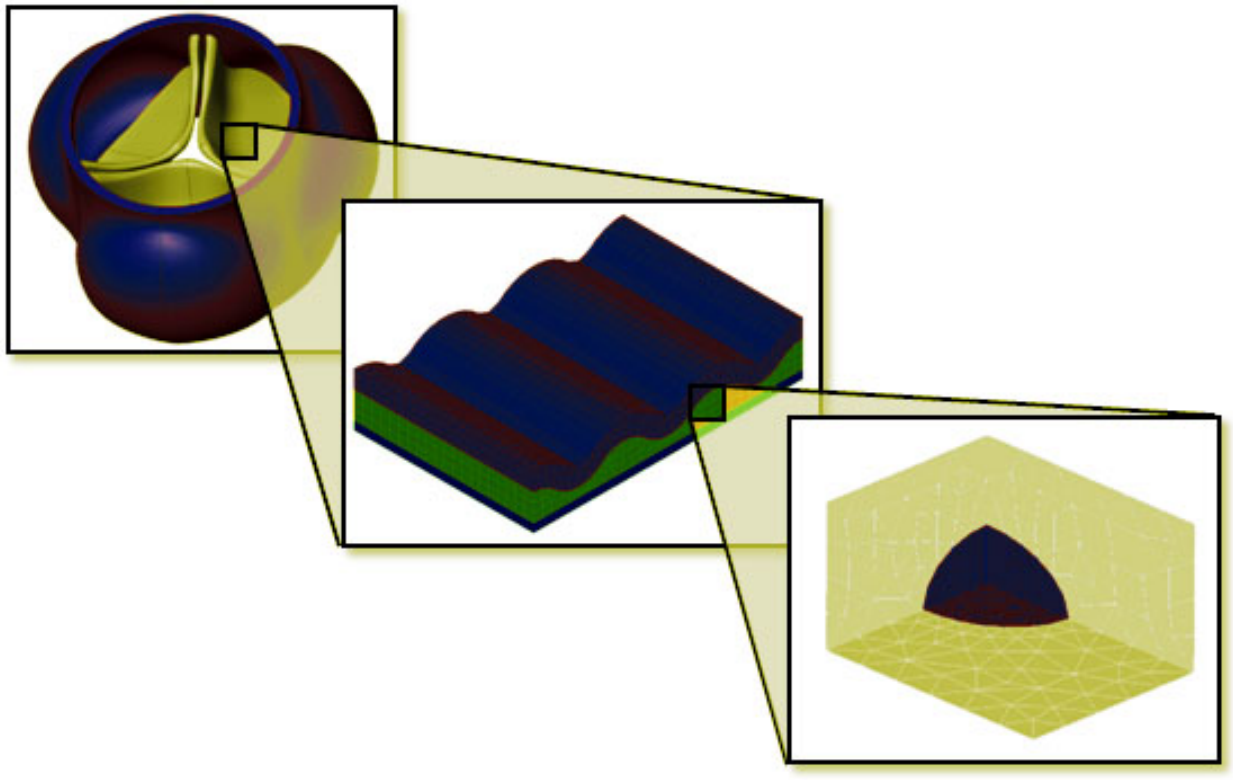

Figure 1.4: Multiscale model ranging over organ, tissue, and cellular scales [172].

One technique that achieves this coupling is computational homogenization [29, 116, 150]. In this method, a system is modeled using FE, but rather than using a mathematical relationship (material law) for the material response, a separate FE model of the periodic (or random) microstructure, the representative volume element (RVE) (see Fig. 1.5), is used to determine the material response. One disadvantage of this method is the computational cost of solving an embedded FE problem, particularly for the complex geometry of heart valves. Several approaches have been developed to speed up computations, such as databases of pre-computed microstructural responses [185] or simplified models of the RVE [184]. Care

must be taken in modeling the embedded cellular scale to assure tractability of the problem. In Chapter 3 and 4, we will use computational homogenization to couple the model proposed by Weinberg and Mofrad.

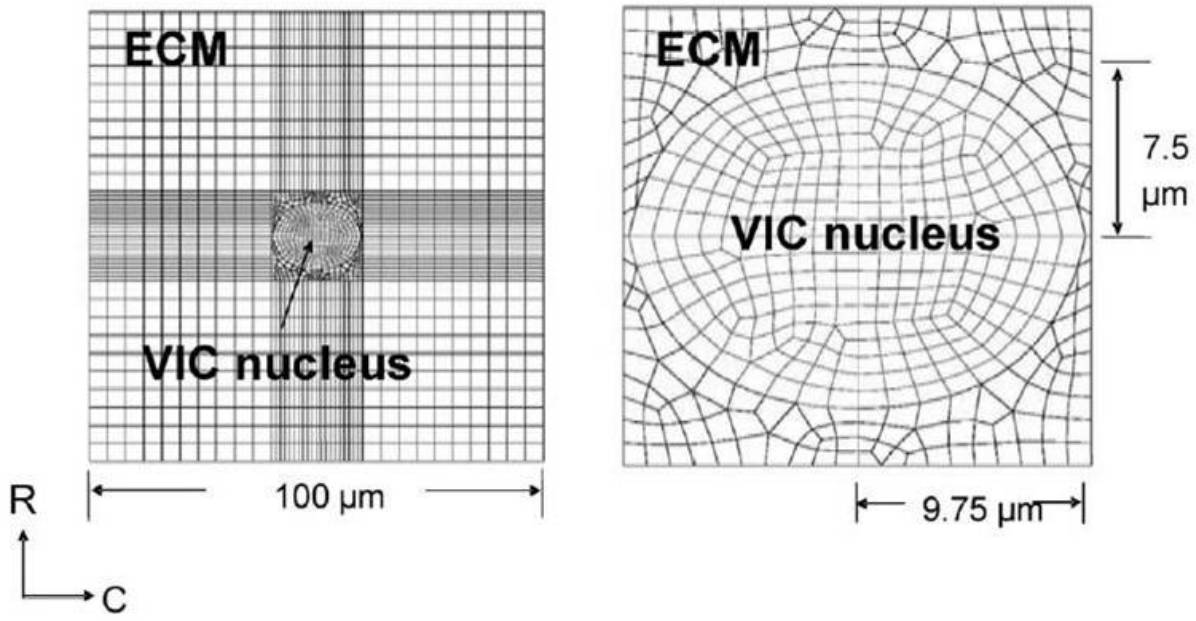

Figure 1.5: Representative volume element (RVE) of heart valve tissue: valvular interstitial cell embedded in the extracellular matrix [80].

Huang et al. used computational homogenization in 2D to link valve tissue behavior with VICs [80]. To our best knowledge, 3D computational homogenization models of valve tissue have not yet been developed. The technique has been applied to tissue-engineering [24, 178] and other soft-tissue modeling applications [61, 107]. For instance, Chan et al. used homogenization to model tissue-engineering scaffolds and account for the nanoscale [24]. Quantum mechanical computations are used at the nanoscale to compute the total energy from applying strains to the RVE [17]. The stress-strain response of the scaffold can consequently be predicted [2]. It may be promising to apply a similar approach to factor in molecular processes that occur in VIC mechanotransduction.

1.5 Applications of aortic valve models

To put these computational models into context, we present several applications. These include studying disease pathology, designing valve prosthetics, tissue-engineering, and aiding in surgical procedures. We limit our discussion to models that are concerned with tissue response of AVs.

Aortic valve disease

Computational models have been used to study bicuspid aortic valve (BAV), a congenitally occurring disorder characterized by an AV with two leaflets instead of three [126, 160]. FE analysis revealed large changes in the leaflet stress/strain distribution [4] and excessive strains when the BAV is opening [87]. FE studies also indicated morphological changes, such as a greatly reduced orifice area [86]. Although it is hypothesized that these morphological and stress/strain differences directly impact the cellular-scale events that lead to, for instance, calcification, multiscale studies have shown that the stresses and strains are not directly translated to the VICs [171]. Instead, the abnormal hemodynamics caused by the BAV has emerged as the probable cause of the induced diseases [14]. For example, dilation and thinning of the ascending aorta downstream of the BAV is marked by smooth muscle cell depletion, elastic fiber degeneration and abnormal ECM remodeling [154]. These findings have been supported by computational studies that demonstrate tissue sensitivity to shear stress abnormalities [4]. Nevertheless, studies maintain that BAV is linked with secondary complications such as aortic regurgitation and stenosis, particularly, calcified aortic stenosis (CAS) [49].

CAS is characterized by stiffening of the AV leaflets due to the development of calcified nodules. The disease is relatively common but the pathogenesis is not currently known. It is theorized that the key to the progression of CAS lies in the VICs [100]. Multiscale computational studies have supported this theory, maintaining the importance of the cell-ECM interaction on CAS [171]. Lipid-lowering pharmaceutical therapy has not demonstrated effectiveness in halting the progression of aortic stenosis, [177] but there is potential for inhibition at the cellular and molecular scales in the case of CAS [122]. This emphasizes the need for multiscale studies that couple cellular-level mechanics and biochemistry driving the calcification growth process [173]. In Chapter 4, we take a look at applying our multiscale framework to calcified AV leaflets.

Assessment and design of artificial valves

AVs with compromised function are typically replaced. FE models can help identify regions of large stresses for the design of more efficient replacement valves that reproduce the native stress configuration [88, 92]. An understanding of the native tissue structure and function is crucial to developing an adequate replacement. The collagen and elastin fiber structure of the leaflet tissue acts as a stress-reducing mechanism to prevent tearing and calcification. Prosthetic valves that are designed with a similar microstructure are potentially more durable [22]. FE models can aid in the design of these valves by determining areas of stress concentrations such that the appropriate fiber distribution is chosen and by simulating long-term effects, such as fatigue [111, 93].

Tissue engineering

Complications associated with prosthetic valves, [34, 67] primarily, thrombogenecity and durability, have shifted artificial valve research towards tissue engineering as an alternative approach for heart valve replacement. Sun *et al.* categorize the application of computation to tissue engineering, or computer aided tissue engineering (CATE), as follows: (1) anatomical modeling, (2) design/manufacturing, and (3) tissue implantation [151]. The first consists of using noninvasive imaging techniques, namely computed tomography (CT), X-RAY, and magnetic resonance imaging (MRI), to construct 3D anatomical models to identify and classify tissues, traumas, and tumors. The second is concerned with fabricating physical models of hard tissues, tissue scaffolds, and custom-made tissue implant prostheses. The third involves applying anatomical and physical modeling for surgical purposes (e.g., implantations of prostheses).

In tissue engineering, cells are seeded onto treated scaffolds, which are subsequently subjected to mechanical stimulation in a bioreactor to grow tissue with the desired mechanical properties. Computational models can be a powerful tool for quantifying the mechanical stimuli in the bioreactors. Computational fluid dynamics models can be used to determine the average shear stresses on the engineered tissue sample, which are directly related to its mechanical properties [45]. On the other hand, mechanochemical models can be used to model tissue growth by explicitly modeling the chemical processes (e.g., nutrient diffusion) that result in growth [96].

The appropriate mechanical loading required to recreate the appropriate tissue fiber structure, however, is not currently known. It is hypothesized that the density, arrangement, diameter, and cross-linking of the collagen fibers are correlated with regions of varying stress in the tissue. Computational models have been used to compute the stress distribution during a cardiac cycle and correlate it with the fiber structure. This information can be used to tailor loading protocols for tissue-engineering and optimize scaffold design for engineering adequate leaflet tissue replacements [46].

Surgical Intervention

Characterization of leaflet stresses and optimal placement of valves with patient-specific models can help improve success rates of valve insertion, repair, and replacement operations, whereas post-operative modeling can avoid future complications and increase longevity of valve replacements [7, 66, 156, 162, 179]. Inverse finite element approaches can be used to back-calculate the stress state in the tissue from medical imagery [54, 81, 82, 134]. Computational models can provide insight on the optimal prosthetic design and insertion procedure in a predictive sense.

Grande et al. developed a FE model of the aortic root, including the AV leaflets, to study the effects of aortic root dilatation [62]. The change in geometry of the ascending aorta is associated with AV incompetence [63]. One treatment option consists of replacing the aortic root with a synthetic graft, while preserving the AV [36]. Grande et al. used their model

to study the stress distribution in the AV leaflets compared to native, healthy condition for these valve-sparing procedures to determine the optimal graft and insertion position [64]. Using a similar modeling approach, Soncini et al. compared different valve-sparing aortic root replacement techniques [145].

AV replacement treatments involve surgical insertion of a valve prosthetic. Auricchio et al. considered patient-specific modeling of the aortic root to aid in the pre-operative planning of the surgical insertion of a prosthetic [5]. The patient-specific FE model was used to study the stress distribution and coaptation area resulting from different prosthetics and their attachment. They further considered the effect of the prosthetic leaflet material, namely the fiber reinforcement distribution, on the AV implant [6]. Similar investigations were carried out by other researchers on stentless prosthetic valves in an effort to characterize the optimal prosthetic and insertion procedure [162]. Additionally, Auricchio et al. simulated transcatheter AV replacement (TAVR) [7]. In TAVR, a balloon-expandable prosthetic valve is surgically implanted via a catheter [31]. The model was used to predict stresses in the aortic root for various positioning of the stent implant (Fig. 1.6).

For AVs that are not too severely diseased, particularly in the case of regurgitation, AV leaflet surgical repair may be performed [112, 177] Labrosse et al. developed FE models to study the impact of different repair techniques on insufficient AVs [95]. The model was validated against in vitro experimental data and conclusions were compared to short-term and mid-term clinical experience. Such models can be used to explore the effectiveness of various and novel repair procedures.

1.6 Summary and future directions

Biological tissue exhibits complex behavior that is often hard to model precisely. In particular, heart valve tissue is inhomogeneous, nonlinear, and anisotropic. Continuum elasticity models are typically used with the addition of fiber recruitment and alignment, leading to acceptable agreement with experimental data. These unique properties, however, are a consequence of the microstructure of valve tissue: the valvular interstitial cells (VICs) and the extracellular matrix (ECM). It has further been shown that the VICs, and their interactions with the ECM, play a significant role in regulating valve pathology.

Understanding and modeling these interactions has potential to halt disease progression at the cellular level [169]. For instance, calcific aortic disease is strongly associated with the appearance of myfibroblasts as a cellular phenotype [130]. Myofibroblasts engage in tissue healing by remodeling the ECM but persistence of myofibroblasts can lead to fibrosis and matrix protein disorganization [74, 175]. Additionally, an osteoblast-like phenotype of VICs has been observed in calcified valve tissue, [132] with corresponding ossification in severely calcified valve tissue satins [120]. The regulation of VIC phenotypes is associated with biomolecular interactions with the ECM, [20] hence, molecular-scale modeling is important for understanding AV disease.

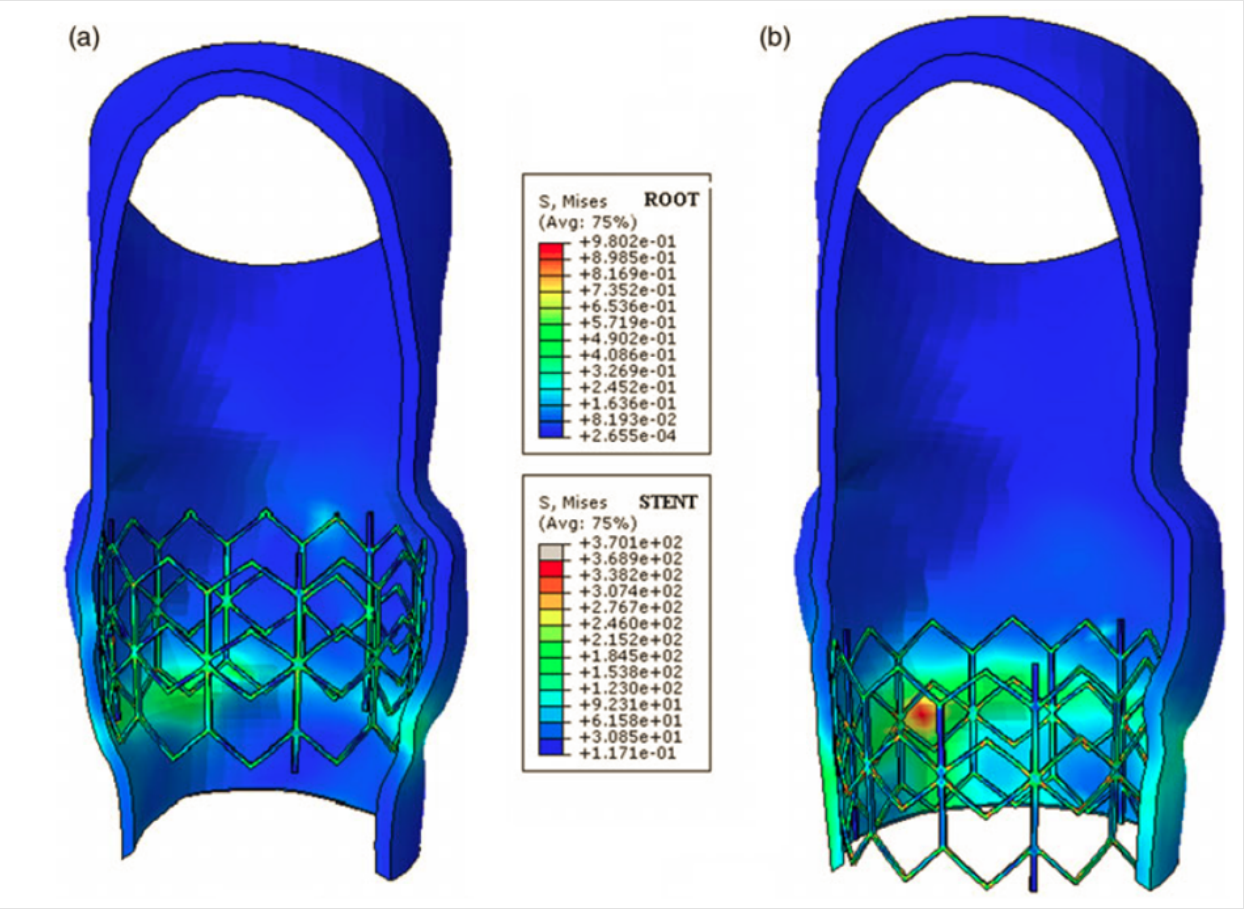

Figure 1.6: Finite element model used to compute stresses for two different stent configurations in an aortic stent insertion operation [5].

One important aspect of any type of model that needs careful consideration is proper validation. Typically, models have been validated with in vitro data [23, 42]. Samples are excised and tested to produce stress and strain data to compare the models to. In vivo data is, however, difficult to obtain. Noninvasive medical imaging techniques, such as X-RAY, echocardiography, magnetic resonance imaging (MRI), and computed tomography (CT), offer a powerful means of obtaining in vivo data of physiological conditions [71, 117, 186]. Combining the images with inverse finite element models can reproduce in vivo stress-strain data to validate models against.

We conclude this chapter with an outlook on future directions in heart valve computational modeling.

Patient-specific modeling

The current trend in biomedical modeling is to develop patient-specific models from imaging data. The aim is to use these models to aid the clinician in diagnosis, customizing treatment plans, and planning surgical procedures. This requires the development of databases that the biomedical engineer, or ideally, the clinician can use to identify aberrances. For instance, Doppler echocardiography signatures can be used to detect, calcification, regurgitation, and stenosis by looking for irregular patterns. The reader is referred to the review by Votta et al. for more on patient-specific modeling [167].

Intra-operative surgical modeling

An important next step for patient-specific models of heart valve computational models is to develop intra-operative models to aid the surgeon by monitoring tissue and fluid stresses during valve surgery [143]. Xu et al. developed such a framework that combines imaging, echocardiography, and FE modeling to assess the in vivo stress of the mitral valve [176]. Other examples of this include the real-time surgical electromechanical model of pulmonary valve replacement surgeries and the intra-operative ultrasound magnetic navigation of transcatheter implantation of AVs [108]. This is still largely a work in progress since, as Labrosse et al. demonstrated, computational time per cycle can be too long to be practical for intra-operative simulation [95]. Mansi et al., however, were able to achieve computational runtimes that are adequate for real-time simulations [110]. The concept of intra-operative systems is to develop a system similar to an existing system that is used for detecting coronary arterial disease in real time with computational fluid dynamics [125, 157, 186].

Engineered valve replacements

Analysis-based design is becoming the standard in all industries, biomedical engineering notwithstanding. Advances in tissue engineering, polymer science and computational techniques have led to the design of robust, versatile, durable, and cost-effective biomaterials and biomedical devices that mimic human tissue. Ongoing studies are aiming to develop bioprosthetic replacement heart valves that mimic human tissue structure (see for instance Argento et al. for a multiscale study of tissue-engineered scaffolds [2]) with the use of novel materials, such as nanocomposite polymers [131]. Nanomanufactored engineered tissues show great promise for achieving this, and thus, there is a need for developing nanoscale simulation techniques to aid in design and assessment [37].

Coupled multiscale modeling

There is a need to develop multiscale models that account for the interaction of the different length and time scales. This is crucial for accurately capturing the macroscopic behavior of materials, which is a consequence of their microstructure, to study the effect of macroscopic

events on, for instance, VICs. Furthermore, incorporating nanoscale modeling is essential for the future of heart valve simulations due to the important role of the interstitial cells and collagen fiber network on the observed material properties, regulation, function, and pathologies of tissue.

The remainder of this will work is focused on coupled multiscale modeling. We will introduce the multiscale model in Chapter 3 and apply it to calcific aortic disease in Chapter 4. But first, we will lay down the foundation for the continuum biomechanics modeling of AV tissue in Chapter 2. Finally, we will conclude in Chapter 5 with limitations of our approach and future directions for building on our methodology.

Chapter 2

Aortic Valve Tissue Biomechanics

Aortic valve tissue exhibits highly nonlinear, anisotropic, and heterogeneous material behavior due to its complex microstructure. A thorough understanding of these characteristics permits us to develop numerical models that can shed insight on the function of the aortic valve in health and disease. In this chapter, we take a closer look at consistently capturing the observed physical response of aortic valve tissue in a continuum mechanics framework. Such a treatment is the first step in developing the multiscale models in the sequel.

2.1 Introduction

Aortic valve (AV) disease is a public health concern with no effective treatment options available, due in part to our incomplete understanding of the complex biological system. Computational modeling is a promising approach for us to gain insight on AVs and to develop viable prevention and treatment modalities. However, such modeling must first accurately reproduce the known before we can use it to probe the unknown. Our focus here is to discuss critical aspects of developing a continuum biomechanical model of AV tissue that is consistent with available experimental data. This basic material specification is a fundamental building block for more complex and comprehensive AV studies, such as multiscale and multiphysics simulations.

Background

AV tissue is comprised of three layers: the fibrosa, the ventricularis, and the spongiosa. The fibrosa and the ventricularis are the main load-bearing layers and they consist of organized networks of collagen and elastin fibers. The crimped collagen fibers align, uncrimp and quickly stiffen in response to loading, resulting in the observed anisotropic, exponential stress-strain behavior. The highly compliant spongiosa serves as a buffer between the other two layers and is composed of proteoglycans. Little data is available on the mechanical behavior of the spongiosa, but the three layers act together as a single unit [139].

Typical continuum models of AV tissue assume homogeneous materials that aim to capture the gross mechanical response; see e.g. [87, 95, 173, 171, 172], as well as [9] and [174] for reviews. Fewer studies look at the heterogeneous nature of the trilayer AV structure (see for instance [172] and [21]). This heterogeneity is essential for correct multiscale modeling efforts [165, 138, 80]. Such models rely upon layer-scale (and possibly finer scale) measurements that can be incorporated into detailed composite models that predict the behavior of intact AV tissue. The consistency of the layer level response model and the composite tissue model is essential for the validity of the entire exercise and a major goal of this paper.

Aortic valve tissue biomechanics

To understand the heterogeneous layer-scale and composite AV tissue behavior, Stella and Sacks [146] subjected excised AV tissue samples to equibiaxial tractions along the "circumferential" and "radial" axes[1]. The layers (fibrosa and ventricularis) were then separated and tested individually. The average load-response curve for each layer and the AV composite tissue is reproduced in Fig. 2.1. We highlight the following from the experiments:

1. The tissue is highly anisotropic: the circumferential response being significantly stiffer than the radial (due to the gross alignment of the collagen fibers in the circumferential direction [11]). Additionally, the fibrosa is significantly stiffer than the ventricularis.

2. At the layer-scale, we observe a "kickback" behavior in the circumferential direction, characterized by a *decrease* in stretch with increasing load.

3. After separation, the fibrosa expands, while the ventricularis contracts, indicating the existence of a prestress in the native AV tissue.

4. Interconnecting fibers that run transmurally (longitudinally/axially) are believed to cause the AV tissue composite to act as a single unit (see also Buchanan *et al.* [21]).

5. The composite AV response in the radial direction is *stiffer* than the individual layers in the same direction. Note the stiffness in Fig. 2.1 may be misleading due to the use of membrane stress, but when correcting for the relative size of the individual and composite samples, the conclusion remains.

Our aim is to develop a model that captures the observed mechanical response of the AV tissue composite within a continuum mechanics framework, based upon layer-scale models which are calibrated to layer-scale measurements.

We restrict our attention to the equibiaxial data presented in Stella and Sacks, as opposed to more general biaxial experiments[2] [16]. The latter study lacks data on the individual layers and it is our goal here to capture layer-scale consistency. We do, however, consider the bending experiment of Sacks [137] to calibrate the small-strain response of the material.

[1] These directions orient the tissue sample with respect to the valve organ; c.f [146]. or [138]

[2] See Sec. 2.5 for a discussion.

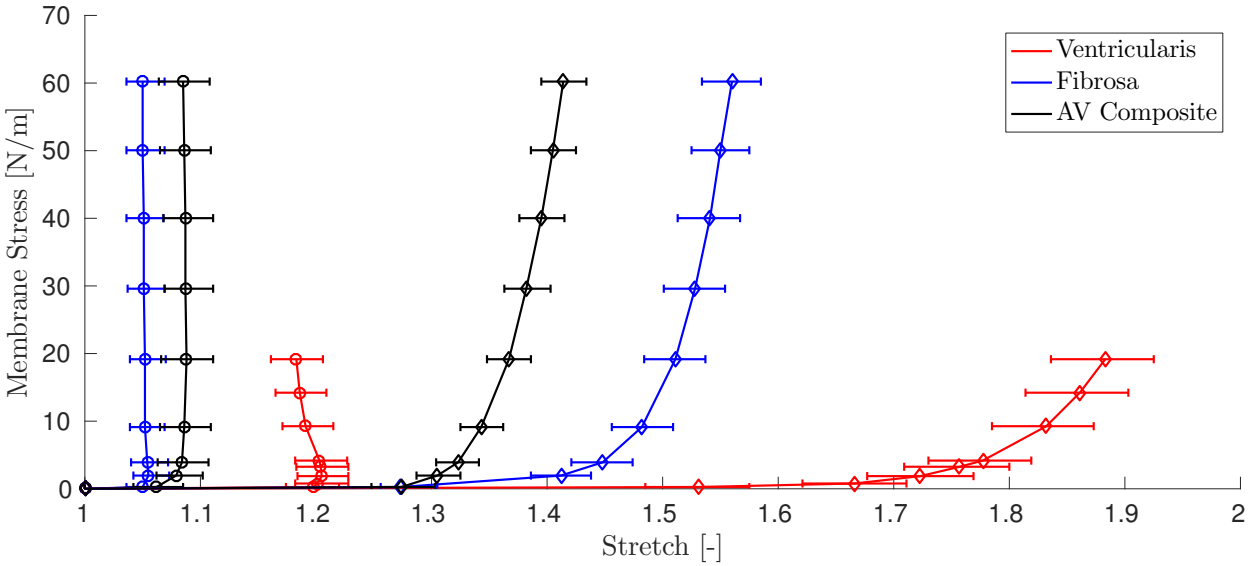

Figure 2.1: Aortic valve layer equibiaxial stretch response via [146]. Circles indicate circumferential response and diamonds indicate radial response.

Outline

This chapter is outlined as follows. In Sec. 2.2 we introduce the continuum mechanics framework. In Sec. 2.3 we detail the model which we calibrate to existing experimental data in Sec. 2.4. We conclude with a discussion, including limitations, in Sec. 2.5.

2.2 Continuum mechanics framework

Continuum mechanics framework

We model the AV tissue within a classical continuum mechanics framework (see e.g., [75]), wherein we seek to solve the governing equations of motion for a body (manifold with boundaries) subject to boundary conditions (tractions and displacements). We define a one parameter (time t) family of finite deformation maps $\boldsymbol{\varphi}_t : \mathbb{R}^3 \mapsto \mathbb{R}^3$ of a hyperelastic body from a reference configuration ($\mathcal{B}_0$) to a current configuration ($\mathcal{B}_t$) (see Fung [56] or Holzapfel [75]). Namely, $\mathcal{B}_t = \boldsymbol{\varphi}_t(\mathcal{B}_0)$.

We define the deformation gradient $\boldsymbol{F} = \nabla\boldsymbol{\varphi}$. Note that $\boldsymbol{F}$ is a 2-point tensor mapping vectors from the reference manifold to the deformed manifold. We define the left and right Cauchy-Green deformation tensors by $\boldsymbol{C} = \boldsymbol{F}^T\boldsymbol{F}$ and $\boldsymbol{b} = \boldsymbol{F}\boldsymbol{F}^T$, respectively. We further define the associated strain tensors: the Green-Lagrange strain tensor $\boldsymbol{E} = \frac{1}{2}(\boldsymbol{C} - \boldsymbol{I})$ for the reference configuration and the Almansi strain tensor $\boldsymbol{e} = \frac{1}{2}(\boldsymbol{I} - \boldsymbol{b}^{-1})$ for the current configuration. $\boldsymbol{I}$ is the identity tensor for vectors in $\mathbb{R}^3$.

The equilibrium deformation map at time t is the one that minimizes the potential energy (Π) of the elastic system subject to conservative traction loading $\bar{\boldsymbol{t}}_t$:

$$\boldsymbol{\varphi}_t^{eq} = \arg\inf_{\boldsymbol{\varphi}_t} \Pi(\boldsymbol{\varphi}_t; \bar{\boldsymbol{t}}_t). \tag{2.1}$$

Under the assumption of hyperelasticity, the 1st Piola-Kirchhoff stress of the system, $\boldsymbol{P}$, is obtained from the Helmholtz free energy, $\hat{\psi}$, of the material:

$$\boldsymbol{P} = \frac{\partial \hat{\psi}}{\partial \boldsymbol{F}}. \tag{2.2}$$

Although the solution to (2.1) is in general not unique, polyconvexity (in the sense of Ball [12]) of the energy function guarantees the existence of a solution. We solve the problem with a standard Finite Element (FE) numerical procedure (Sec. 2.2). Our challenge is to specify $\hat{\psi}$ such that the FE model is consistent with the observed experimental response.

We can further define two additional stress tensors: the 2nd Piola-Kirchhoff stress tensor $\boldsymbol{S}$ and the Cauchy stress tensor $\boldsymbol{T}$. The relationship between the stress tensors is

$$\boldsymbol{T} = J^{-1}\boldsymbol{F}\boldsymbol{P} = J^{-1}\boldsymbol{F}\boldsymbol{S}\boldsymbol{F}^T, \tag{2.3}$$

where $J = \det(\boldsymbol{F})$ is the Jacobian (of the deformation gradient).

Polyconvexity

A sufficient condition for the existence of $\boldsymbol{\varphi}_t^{eq}$ in (2.1) is the quasi-convexity of $\hat{\psi}$ [121]. A more tractable condition (that implies quasi-convexity) is the notion of polyconvexity, in the sense of Ball [12].

$\boldsymbol{F} \mapsto \hat{\psi}(\boldsymbol{F})$ is polyconvex *if and only if* there exists a function $G : \mathbb{R}^{19} \mapsto \mathbb{R}$ such that

$$\hat{\psi}(\boldsymbol{F}) = G\big(\boldsymbol{X}\big), \tag{2.4}$$

where $X = (\boldsymbol{F}, \operatorname{Adj}\boldsymbol{F}, \det\boldsymbol{F})$, $\operatorname{Adj}\boldsymbol{F}$ is the transpose of the cofactor matrix of $\boldsymbol{F}$, $\det\boldsymbol{F}$ is the determinant of $\boldsymbol{F}$ and $G : \mathbb{R}^{19} \mapsto \mathbb{R}$ is convex $\forall \boldsymbol{X} \in \mathbb{R}^{19}$. Quasi-convexity implies rank-1 convexity[3], which in turn implies (for smooth, twice differentiable ψ, as we have) the Legendre-Hadamard condition [33]:

$$\exists c > 0 \ \forall \boldsymbol{F} \in \mathbb{R}^{3\times3}, \ \forall \boldsymbol{a}, \boldsymbol{b} \in \mathbb{R}^3 \setminus \{0\} \mid D^2\psi(\boldsymbol{F})[\boldsymbol{a}\otimes\boldsymbol{b}, \boldsymbol{a}\otimes\boldsymbol{b}] \geq c||\boldsymbol{a}||^2||\boldsymbol{b}||^2. \tag{2.5}$$

Thus, polyconvexity of an energy function implies ellipticity of the acoustic tensor for all deformation, which is a sufficient condition to guarantee the material wave speed is real and positive [144].

[3]Rank-1 convexity: $f(t) := \psi(\boldsymbol{F} + t\boldsymbol{a}\otimes\boldsymbol{b})$ is convex $\forall \boldsymbol{a}, \boldsymbol{b} \in \mathbb{R}^3$, and $\forall \boldsymbol{F} \mid \det\boldsymbol{F} > 0$.

Finite element modeling

We use an FE approach to solve (2.1). Let $\partial\mathcal{B}_u$ and $\partial\mathcal{B}_t$ denote the partitions of the boundary ($\partial\mathcal{B}_0$) of the body, $\mathcal{B}_0$, where deformation and tractions are imposed, respectively, with $\partial\mathcal{B}_u \cap \partial\mathcal{B}_t = \emptyset$, $\overline{\partial\mathcal{B}_u \cup \partial\mathcal{B}_t} = \partial\mathcal{B}_0$. Equation (2.1) is solved by satisfying the weak form statement:

Find

$$\boldsymbol{\varphi} \in \mathcal{S} := \{\boldsymbol{\varphi} \mid \boldsymbol{\varphi} = \bar{\boldsymbol{\varphi}} \text{ on } \partial\mathcal{B}_u\},$$

such that

$$\int_{\mathcal{B}_0} \boldsymbol{P} \cdot \nabla(\delta\boldsymbol{\varphi})\, dV = \cancel{\int_{\mathcal{B}_0} \boldsymbol{B} \cdot \delta\boldsymbol{\varphi}\, dV} + \int_{\partial\mathcal{B}_t} \bar{\boldsymbol{t}} \cdot \delta\boldsymbol{\varphi}\, dA, \tag{2.6}$$

$$\forall \delta\boldsymbol{\varphi} \in \mathcal{V} := \{\delta\boldsymbol{\varphi} \mid \delta\boldsymbol{\varphi} = \boldsymbol{0} \text{ on } \mathcal{B}_u\},$$

where ρ_0 is the material density in $\mathcal{B}_0$ and we assume there is no body force $\boldsymbol{B}$. The FE solution begins with a tessellation of the domain (viz. Fig. 3.4) into a finite set of discrete nodes and elements. Letting the superscript g denote discretized parameters, and $N^A(\boldsymbol{x})$ denote interpolating shape functions in each element, we construct a Galerkin discretization as:

$$\mathcal{B}_0^h = \mathop{\mathsf{A}}_{e=1}^{n_{el}} \mathcal{B}_0^e, \quad \boldsymbol{u}^g = \sum_{A=1}^{n_n} N^A \boldsymbol{u}_A, \quad \delta\boldsymbol{u}^g = \sum_{A=1}^{n_n} N^A \delta\boldsymbol{u}_A, \tag{2.7}$$

where e indexes the n_{el} elements in the domain, $\boldsymbol{u}$ denotes displacements, $\delta\boldsymbol{u}$ denotes variational displacements, $\boldsymbol{u}_A$ denotes nodal displacements indexed by A over n_n nodes per element, and $\mathop{\mathsf{A}}_{\mathrm{e=1}}^{\mathrm{n_{el}}}$ is the assembly operator [188]. Substituting (2.7) into (2.6) leads to the nonlinear (static) equilibrium equations:

$$\boldsymbol{R}(\boldsymbol{u}_t) = \boldsymbol{f}_t - \mathop{\mathsf{A}}_{e=1}^{n_{el}} \int_{\mathcal{B}_0^e} \nabla \boldsymbol{N}_e^T \boldsymbol{P}_e\, dV_e = 0, \tag{2.8}$$

where $\boldsymbol{R}$ is the residual for a state of displacements $\boldsymbol{u}_t$ at time t, which must be in equilibrium with the applied nodal forces $\boldsymbol{f}_t$ at time t, and $\nabla\boldsymbol{N}$ is the matrix formed from derivatives of the shape functions $N^A(\boldsymbol{X})$ with respect to $\boldsymbol{X}$. The reader is referred to Zienkiewicz and Taylor [188] for a comprehensive treatment of the FE procedure.

We use an iterative Newton-Rhapson approach to solve (2.8). Given an initial state $\boldsymbol{u}_t^0$, the update equations are

$$\boldsymbol{u}_t^{k+1} \leftarrow \boldsymbol{u}_t^k - \boldsymbol{K}_T^{-1}(\boldsymbol{u}_t^k)\boldsymbol{f}_t, \tag{2.9}$$

where

$$\boldsymbol{K}_T = \frac{\partial \boldsymbol{R}}{\partial \boldsymbol{u}} = \mathop{\mathbf{A}}_{e=1}^{n_{el}} (\boldsymbol{k}_{e,\text{mat}} + \boldsymbol{k}_{e,\text{geom}}), \tag{2.10}$$

is the linearized tangent stiffness. The element material stiffness is

$$\boldsymbol{k}_{e,\text{mat}} = \int_{\mathcal{B}_e} \bar{\nabla} \boldsymbol{N}_e^T \boldsymbol{c} \bar{\nabla} \boldsymbol{N}_e \, dV, \tag{2.11}$$

where, $\bar{\nabla}$ is the gradient operator with respect to the spatial manifold, and $\boldsymbol{c}$ is the spatial material tangent, defined as

$$c_{ijkl} = \frac{1}{J} F_{iA} F_{jB} F_{kC} F_{lD} \mathbb{C}_{ABCD}, \tag{2.12}$$

the push-forward of the material tangent $\mathbb{C} = 2\partial \boldsymbol{S}/\partial \boldsymbol{C}$. The element geometric stiffness is

$$\boldsymbol{k}_{e,\text{geom}}^{AB} = \left(\int_{\mathcal{B}_e} N_{,i}^A T_{ij} N_{,j}^B \, dV \right) \boldsymbol{I}, \tag{2.13}$$

where summation convention is implied, with lower-case subscripts indicating the spatial coordinates, subscript commas indicating partial differentiation, upper-case subscripts indicating the reference coordinates, and upper-case superscripts indicating nodal numbers. Note that the integrals for the stiffnesses are taken over the deformed element. The iterations are carried out until a stopping criterion, such as the satisfaction of (2.8) within some tolerance. For the Newton-Rhapson strategy to converge, the initial guess must be in the neighborhood of the solution. This requirement poses an issue for the highly nonlinear AV tissue, particularly in the low stiffness regime.

To address this problem, we apply the load incrementally and adaptively. We start with a small load factor α_t ($\boldsymbol{f}_t = \alpha_t \boldsymbol{f}_0$) and adjust the factor heuristically based on the number of iterations (n_i) it takes for (2.9) to converge ($\alpha_t \propto n_i^{-1}$). In this manner, we are able to circumvent the use of unreasonably small load factors (i.e., excessive computational time) during the entire load path. If a load factor is too large and the Newton-Rhapson algorithm diverges, we appropriately scale the load factor down.

2.3 Consistent tissue model

Material model

For each individual layer we choose a Helmholtz free energy $\psi(I_1, J_4, J) := \hat{\psi}(\boldsymbol{F})$ of the form

$$\begin{aligned} \psi = C_{1m}\Big\{ \exp\big[C_{2m}(I_1 - 3)\big] - 1\Big\} + \sum_{i=1}^{n_f} \frac{C_{1f}}{2C_{2f}} \Big\{ \exp\big[C_{2f}(J_4^i - 1)_+^3\big] - 1 \Big\} \\ + c_1(I_1 - 3) + c_2(J^2 - 1) + c_3 \ln(J). \end{aligned} \tag{2.14}$$

The first term on the right hand side is a Fung-like [56] isotropic term, where $I_1 = \text{tr}(\boldsymbol{F}^T\boldsymbol{F})$ is the first invariant, and C_{1m}, C_{2m} are material parameters. The second term is a directional term in the spirit of Holzapfel [76, 77] to account for the n_f collagen fiber directions, where $J_4^i = \text{tr}(\boldsymbol{C}\boldsymbol{M}_i)$ is the first mixed invarient for the fiber direction indexed by i, with $\boldsymbol{M}_i = \boldsymbol{m}_i \otimes \boldsymbol{m}_i$, $||\boldsymbol{m}_i||_2 = 1$, as the rank-1 structure tensor. C_{1f}, C_{2f} are material parameters and $(x)_+ := \max(x, 0)$ guarantees that the fibers do not take compressive load. The last three terms represent a Neo-hookean ground substance (see [68]) with parameters c_1, c_2, c_3.

To establish the polyconvexity of (2.14), we turn to Appendices B and C of Schröder and Neff [144], namely, Lemmas B.9, C.2, and C.4. A necessary and sufficient condition for polyconvexity is then

$$C_{1m}, C_{2m}, C_{1f}, C_{2f}, c_1, c_2, -c_3 > 0. \tag{2.15}$$

Note that for the case $C_{1m}, C_{2m}, C_{1f}, C_{2f} = 0$, e.g., the spongiosa, the material is Neo-hookean, which is indeed polyconvex.

We impose that our material model, in the infinitesimal strain limit, recovers an isotropic linear elastic model.[4] Define the linearization operator as:

$$\text{Lin}\, \boldsymbol{f}(\boldsymbol{y})[\boldsymbol{u}] := \boldsymbol{f}(\boldsymbol{y}) + D\boldsymbol{f}(\boldsymbol{y})[\boldsymbol{u}], \tag{2.16}$$

where $D\boldsymbol{f}[\boldsymbol{u}]$ denotes the Fréchet differential in direction $\boldsymbol{u}$. We then linearize about $\boldsymbol{0}$ and impose that

$$\text{Lin}\, \boldsymbol{T}(\boldsymbol{0})[\boldsymbol{u}] = \boldsymbol{\sigma}_{\ell in}, \tag{2.17}$$

where $\boldsymbol{T}$ is the Cauchy stress tensor and $\boldsymbol{\sigma}_{\ell in}$ is the infinitesimal stress tensor. Equation (2.17) leads to the following conditions:

$$c_1 = \mu/2 - C_{1m}C_{2m}, \quad c_2 = K/4 - \mu/6 - C_{1m}C_{2m}^2, \quad c_3 = 2C_{1m}C_{2m}^2 - K/2 - 2\mu/3, \tag{2.18}$$

where μ and K are the infinitesimal-strain shear and bulk moduli, respectively. The stress and tangent are given by

$$\boldsymbol{T} = 2c_1\frac{\boldsymbol{b}}{J} + 2C_{1m}C_{2m}A_m\frac{\boldsymbol{b}}{J} + \sum_i^{n_f} 3C_{1f}(J_4^i - 1)_+^2 A_f \boldsymbol{b}_m/J + (2c_2 J + c_3/J)\boldsymbol{I}, \tag{2.19}$$

where, $A_f := \exp\left[C_{2m}(I_1 - 3)\right]$, $A_m := \exp\left[C_{2f}(J_4^i - 1)_+^3\right]$, and $\boldsymbol{b}_m = \boldsymbol{F}\boldsymbol{M}\boldsymbol{F}^T$. The material tangent (in the spatial configuration) is:

[4] By construction, the fibers have negligible contribution in the infinitesimal regime.

$$\begin{aligned}\boldsymbol{c} = \frac{1}{J}\Big[&4c_2J^2\boldsymbol{I}\otimes\boldsymbol{I} - 2(2c_2J^2+c_3)\mathbb{I}\\ &+ 4C_{1m}C_{2m}^2A_m\boldsymbol{b}\otimes\boldsymbol{b}\\ &+ 6C_{1f}A_f\big(2(J_4-1)_+ + \sum_i^{n_f} 3C_{2f}(J_4^i-1)_+^4\big)\boldsymbol{b}_m\otimes\boldsymbol{b}_m\Big],\end{aligned} \tag{2.20}$$

where $\boldsymbol{I}$ is the order-2 3×3 identity tensor and $(\mathbb{I})_{ijkl} = \frac{1}{2}(\delta_{ik}\delta_{jl}+\delta_{il}\delta_{jk})$, ($\delta_{ij}$ is the Kronecker delta).

In valve tissue, the collagen fibers are primarily aligned in the circumferential direction [16]. We define a locally *Cartesian* coordinate system (c, r, h) aligned with the circumferential, radial, and transmural directions, respectively (see Fig. 2.2 and/or [16]). In the spirit of Billiar and Sacks [16], we assume a normally distributed family of fibers lying in the $\boldsymbol{e}_c\otimes\boldsymbol{e}_r$ plane. The structure tensor for each fiber is fully defined by the direction

$$\boldsymbol{m}_i := \cos(\theta_i)\boldsymbol{e}_c + \sin(\theta_i)\boldsymbol{e}_r, \tag{2.21}$$

where $\theta_i \in \mathcal{N}(\mu_f, \sigma_f)$, a normal distribution with mean μ_f and standard deviation σ_f. Herein, we take $\mu_f = 0$ (i.e., mean alignment in the circumferential direction) and let σ_f be a free parameter.

Little information is available regarding the mechanical properties of the Spongiosa, and thus, we assume it behaves like a Neo-hookean material (i.e., $C_{1m} = C_{2m} = C_{1f} = C_{2f} = 0$).

Remark on the fiber model: We follow the discrete Holzapfel fiber model [76] as opposed to the continuous one [77] because it allows us to explicitly model the individual fiber directions. The latter gives the asymptotic response of the former (i.e., $\lim_{n_f\to\infty}$) in a computationally efficient manner. We recommend the continuous models (see also [57] and [52]) for larger problem sizes (e.g., full aortic valve geometry), but the discrete model provides a more accurate and insightful representation of the fiber micromechanics. Note that unlike the Holzapfel model, we have $(J_4-1)^3$, rather than $(J_4-1)^2$ so that ψ is smooth and twice differentiable in the presence of the hinge $(x)_+$.

Remark on viscoelasticity: AV tissue demonstrates viscoelastic behavior when subject to relaxation experiments [99]. Due to the slow nature of the loading in the referenced experiments, one can safely neglect viscoelasticity.

Parameter fitting

We consider calibrating the parameters in (2.14) to experimental data. We first begin by drawing and fixing a set of $n_f = 30$ fibers[5] from $\mathcal{N}(0,1)$, then scale appropriately by σ_f:

[5]Our choice of $n_f = 30$ is a balance between accuracy and computational efficiency.

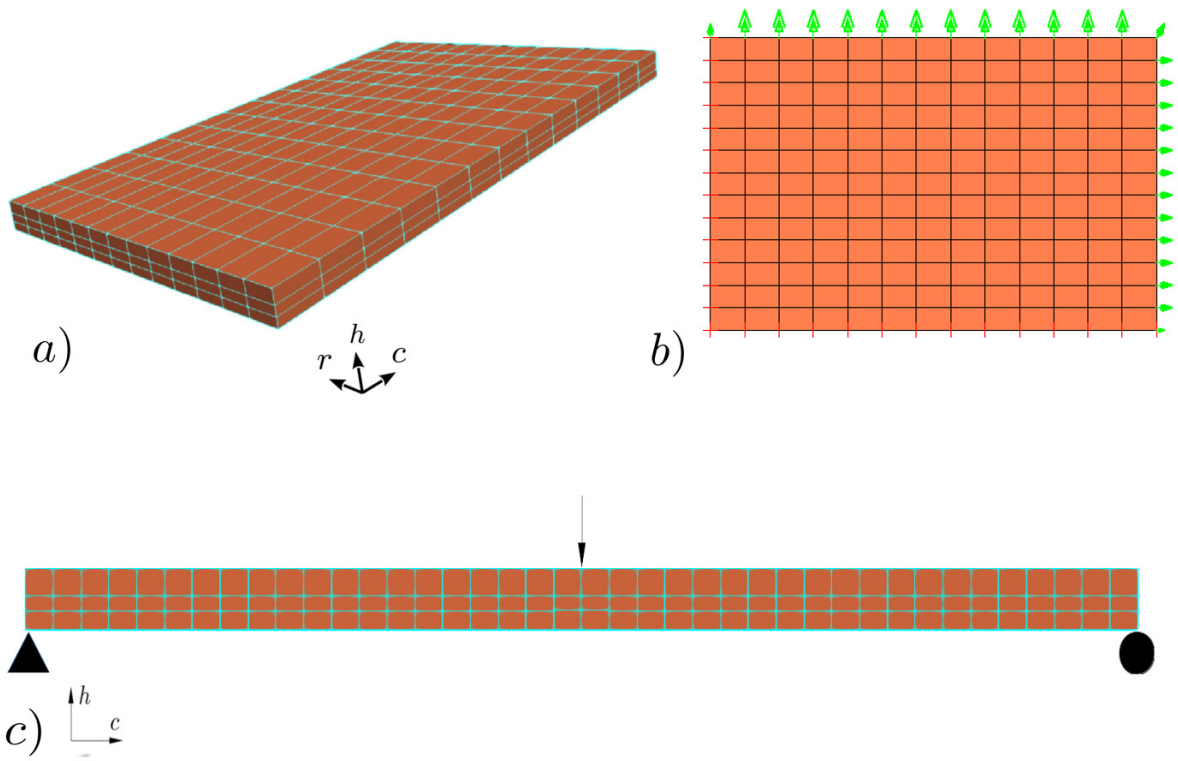

Figure 2.2: a) FEM trilayer tissue model generated with Paraview [1]. b) 1/4 symmetry FEAP model with boundary displacement and traction boundary conditions. c) FE bending simulation *a la* Sacks [137]

$\mathcal{N}(0, \sigma_f) = \sigma_f \mathcal{N}(0, 1)$. The finite-strain parameters $(C_{1m}, C_{2m}, C_{1f}, C_{2f}, \sigma_f)$ are, by construction, little effect for infinitesimal deformation. However, the prestressing engages these parameters and leads to a co-dependence between the finite-strain and infinitesimal-strain (μ and K) parameters. In light of this, we fit the full parameter set in an iterative manner between the small deformation bending and large deformation equibiaxial stretch experiments as follows:

1. Choose an initial value of μ (K is fixed) from Euler-Bernoulli beam bending theory.
2. Fit the finite-strain parameters for each layer with the procedure described in 2.3.
3. Determine the necessary prestress for the composite tissue with the procedure described in 2.3.

4. Determine μ with the procedure described in 2.3.

5. Repeat 2-4 until convergence.

We present a metric in (2.22) to assess the goodness of fit for the layers and the composite with respect to the equibiaxial stretch experiments.

Equibiaxial stretch

We define a residual sum of squares loss

$$\ell(C) := \sum_{i=1}^{n} (\lambda_c^e - \lambda_c^m(C))_i^2 + (\lambda_r^e - \lambda_r^m(C))_i^2, \tag{2.22}$$

where $C := (C_{1m}, C_{2m}, C_{1f}, C_{2f}, \sigma_f)$, λ is the stretch for a given membrane stress, obtained from the 1st Piola-Kirchhoff stress tensor, and n is the total number of data points; the subscript indicates the direction, and the superscripts e, m denote experimental and model, respectively. We seek the parameters that minimize the nonconvex loss:

$$C^* = \arg\min \ell(C) \text{ subject to } C > 0. \tag{2.23}$$

Despite the nonconvexity, we can converge to a sufficiently good local minimum using warm-start projected gradient descent with backtracking line-search ([124] Chap. 3) implemented in the MATLAB [113] package *minConf* [141]. Because $\ell(C)$ is not an analytical function ($\lambda^m(C)$ is computed from an FE model, detailed in Sec. 2.2), we estimate the gradients ($\nabla\ell$) with finite differences by probing the FE model with perturbed parameters:

$$\frac{\partial \lambda^m}{\partial C_j} \approx \frac{\lambda^m(C + \delta e_j) - \lambda^m(C)}{\delta}, \tag{2.24}$$

where $e_j \in \mathbb{R}^5$ is the standard Cartesian basis vector and δ is a suitable differential.

Bending

We fit the infinitesimal-strain parameters to the bending experiment of Sacks [137], where the AV tissue exhibits linear response over the range of applied deformation. Since we fix the "bulk modulus" $K = 2.2 \times 10^3$ kPa (see Sec. 2.3), all that remains is to fit the "shear modulus" μ such that the bending stiffness is consistent with the values measured by Sacks. Due to a lack of further experimental data, we assume all three layers have the same K and μ. Note that the interlayer heterogeneity is mostly a consequence of the collagen and elastin fiber content of each layer (or lack thereof) and thus it is not unreasonable to assume a homogeneous matrix otherwise.

Sacks' bending experiment consisted of $\sim$14$\times$3 $\times$ 0.4 mm strips of AV tissue that are subject to 3-point bending. Positive and negative midspan deflections were applied with a rigid rod attached to a load cell and the beam deformation field was measured with markers

along the edge. The moment-curvature (M versus κ) response was observed to be linear over the range of applied midspan deflections ($\sim \pm 1$ mm), with an effective Young's modulus $E = M/(I\kappa) \approx 5.3$ kPa. Our bending model is described in 2.3 where we choose μ such that $M/(I\kappa) \approx 5.3$ kPa. Note that due to the linearity of the response, only a single simulation is needed to determine μ once K has been fixed.

Models and boundary conditions

We consider four models: 1) equibiaxial stretch of the fibrosa, 2) equibiaxial stretch of the ventricularis, 3) equibiaxial stretch of the trilayer AV composite, and 4) beam bending of the trilayer AV composite. For all models, we tessellate the domain into 8-node linear brick elements (Fig. 2.2a) to obtain an approximate numerical solution to (2.6) using the FE software package FEAP [159].

The fibrosa and ventricularis equibiaxial stretch model dimensions ($c \times r \times h$) are $11.5 \times 6.3 \times 0.20$ mm and $8.0 \times 5.5 \times 0.15$ mm, respectively, with a mesh size of $13 \times 13 \times 1$. The AV composite equibiaxial stretch model dimensions are $\sim$9.0 $\times$6.0 $\times$ 0.46 mm with a mesh size of $13 \times 13 \times 3$. The AV composite beam dimensions are $14.0 \times 3.0 \times 0.46$ mm with a mesh size of $80 \times 4 \times 12$. A mesh convergence study is given in Fig. 2.4.

Equibiaxal stretch

Stella and Sacks applied equibiaxial membrane stresses[6] via four discrete points per side and measured the approximately homogeneous strain in the center of the tissue on the surfaces of the fibrosa and the ventricularis. The overall mechanical behavior of the tissue is not affected by the technical details of these boundary conditions. In fact, we can simply apply uniform normal tractions along the circumferential and radial edges with (1/4) symmetry boundary conditions on the respective opposite edges (Fig. 2.2b). To see this we take a closer look at the equibiaxial stretch experiment of Stella and Sacks [146] and discuss the appropriate use of boundary conditions when recreating the experiment with a finite element model. We refer the reader to [138] for details on the biaxial testing apparatus and [146] for details on preparation of the tissue samples.

The excised tissue samples are loaded in biaxial tension via four nylon strings per side, attached with surgical staples. The deformation is applied via load transducers such that the membrane stress (force divided by length) is equal on both the circumferential and radial axes. The deformation reported is obtained via strain imaging near the center of the specimen on the two surfaces: the fibrosa and ventricularis. The deformation in the fibrosa and the ventricularis are nearly identical. Prior to the main experiment, the samples are preconditioned with cyclic loading. The loading protocol begins with a small preload (0.5g) and the deformation is then measured with reference to the preloaded initial state.

[6]Membrane stress here is the force divided by the *initial* length of the edge the force is applied to, i.e., the 1st Piola-Kirchhoff membrane stress.

In our simulations, we apply the load as a uniform traction along two juxtaposed edges with boundary restraints in the same direction on the respective opposite edges. We then measure the deformation at the center of the specimen on the surface of both the fibrosa and the ventricularis. We use stiff springs on the edges to mimic the effect of the staples, i.e., the layers deform together under traction-controlled loading.

To demonstrate that our choice of boundary conditions does not change the overall behavior of the material, we fit additional models with the load applied at four discrete points per edge (Figure 2.3 right). We present the fit parameters for both models (uniform and discrete boundary conditions) in Table 2.1 and the deformed shape at maximum loading (60 N/m) in Figure 2.3. Note that the parameters for the "discrete" case are within the 95% confidence intervals in Table 2.2.

Model	C_{1m}	C_{2m}	C_{1f}	C_{2f}	σ_f
Fibrosa Uniform	4.38	8.82	18.0	1.53×10^3	6.28
Fibrosa Discrete	2.65	8.90	24.25	1.70×10^3	5.89
Ventricularis Uniform	1.13	4.11	8.68×10^{-2}	46.10	8.19
Ventrcularis Discrete	0.74	4.21	6.63×10^{-1}	27.81	9.51

Table 2.1: Material parameters for uniform and discrete boundary condition models.

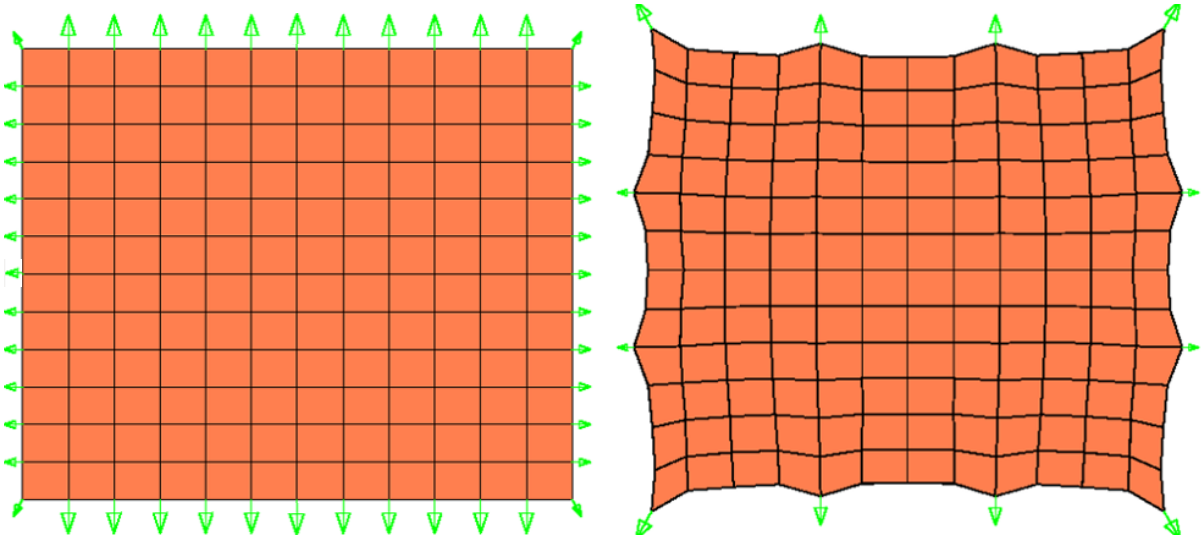

Figure 2.3: Loading and deformation of biaxial stretch models. **Left**: Uniform boundary conditions. **Right**: Discrete boundary conditions.

The nature of the biaxial testing rig forces the three layers to deform together, so we apply stiff spring constraints along the thickness on the boundaries where the traction is applied to ensure that the three layers deform homogeneously in the plane (but heterogeneously out of

plane). Motion in the h direction is restrained at the bottom (ventricularis) corners[7]. Note that the boundary conditions apply to the layer models as well as the composite model.

Bending

The simply supported bending model is depicted in Fig. 2.2c. We apply symmetry boundary conditions in the r direction. A midspan deflection is incrementally imposed on the beam and the resulting curvature is computed from a fourth order polynomial fit to the nodal displacements at mid-depth to mimic the experiments. The prestressing (see Sec. 2.4) results in an initial curvature κ_0, and thus the moment-curvature response is measured relative to the initial curvature (i.e., M versus $\Delta\kappa$, where $\Delta\kappa = \kappa - \kappa_0$).

Interconnecting fibers

The AV composite tissue is known to act as a single bonded unit [21]. Dissection of the layers reveals interconnecting fibers that span from the fibrosa to the ventricularis [146]. We model the effect of the interconnecting fibers with perfectly bonded interfaces (i.e., no slip) between adjacent layers.

Prestress

The average AV specimen dimensions from the experiments of Stella and Sacks are $\approx 9 \times 6 \times 0.5$ mm, $c \times r \times h$ respectively. When separated, the fibrosa (on average) expands to $11.5 \times 7 \times 0.4$ mm and the ventricularis (on average) contracts to $8 \times 5.5 \times 0.2$ mm. We perform the experiment in reverse: we prestress the native stress-free configurations of the layers and attach them (with rigid links) to form the AV composite. The prestressing procedure is summarized as follows:

1. The ventricularis and fibrosa are stretched from their "stress-free" configurations to (approximately) the AV dimensions (as reported by Stella and Sacks [146]).
2. The layers are then attached and allowed to equilibrate. The AV composite analysis (biaxial stretch and bending) is performed with reference to the attached and equilibriated state.

Remark on prestressing

The fibrosa exhibits a corrugated structure when part of the unloaded AV composite. This geometry is a consequence of a buckling phenomenon in the fibrosa which makes it difficult to determine its true stress-free configuration with the material model we consider here. Thus, we leave the stress-free configuration of the fibrosa as a free parameter in item 1 above. We return to this point in Sec. 2.5.

[7]The corner boundary conditions translate to only one of the four corners for the 1/4 symmetry model.

Quasi-incompressibility

AV tissue exhibits quasi-incompressiblity [139]. To obtain a numerically stable, quasi-incompressible material response, we choose a "bulk modulus" of $K = 2.2 \times 10^3$ kPa. Note from (2.18), K acts as a penalty-like enforcement of $J \approx 1$. We accordingly use $u - p - \vartheta$ mixed-formulation elements [109]. We observe a change of volume well below 1% for the biaxial stretch and bending simulations.

Remark on FE modeling

Note that although we can solve the biaxial stretch problem for the individual layers analytically, the prestressed trilayer AV composite requires a numerical approach.

2.4 Results

Mesh convergence

Figure 2.4 shows mesh convergence studies for our beam and equibiaxial models for the AV composite system, in both prestressed and non-prestressed states. The mesh densities we use in our study are consistent with converged mesh densities from these plots. The quantities we monitor for convergence are those relevant to the data analysis we are interested in. Note that for brevity we do not show the convergence study for the single layer equibiaxial cases, and simply note they are similar.

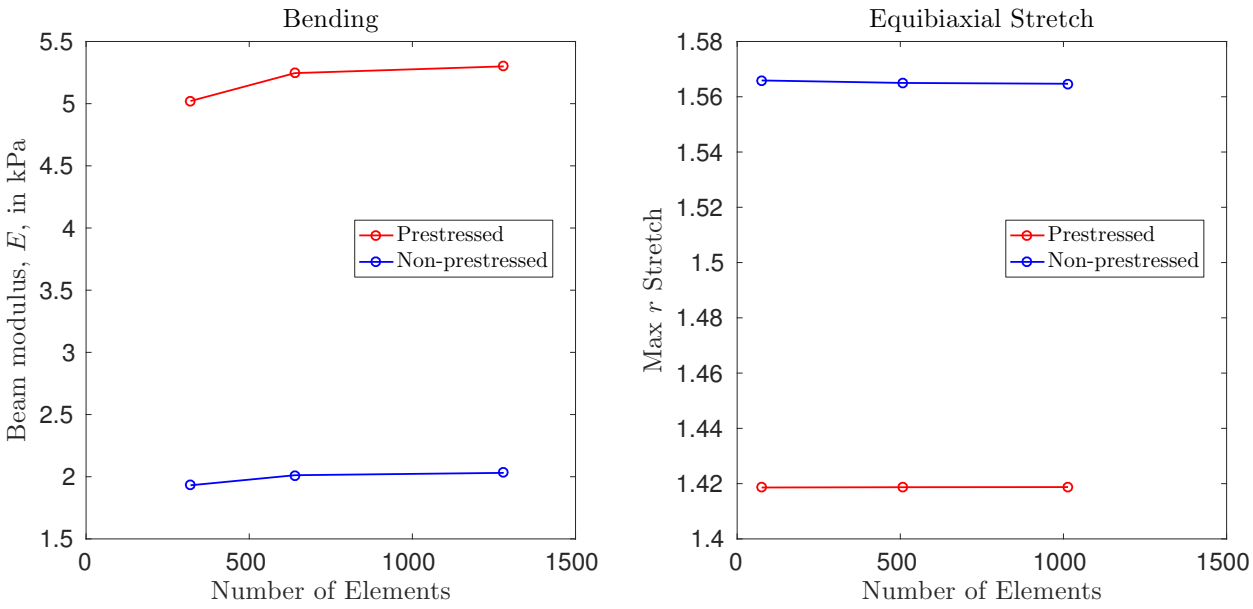

Figure 2.4: Convergence studies for AV trilayer FE meshes.

Parameter fitting

The parameter fitting is performed using the equibiaxial data for the AV composite plus the individual layers, together with the bending data. Table 2.2 summarizes each layer's calibrated finite-strain parameters. Also shown are 95% confidence intervals computed via bootstrap [43] and a sample $\ell(C)$ per (2.22) (the loss curves of both layers have the same characteristic shape). Figure 2.5 top demonstrates convergence of $\ell(C)$. Figure 2.5 bottom features a perturbation analysis of the fit parameters and demonstrates convergence to a local minimum. Note the relative sensitivity of C_{2m}. The individual layer load-deformation curves are presented in Fig 2.6 bottom.

Model	C_{1m} [Pa]	C_{2m} [-]	C_{1f} [Pa]	C_{2f} [-]	σ_f [°]
Fibrosa	4.38	8.82	18.0	1.53×10^3	6.28
	(1.15,7.15)	(8.20,10.40)	(5.11,50.72)	$(0.76,1.98)\times 10^3$	(5.87,7.59)
Ventricularis	1.13	4.11	8.68×10^{-2}	46.10	8.19
	(0.45,2.13)	(3.76,4.51)	$(0.24,40.1)\times 10^{-1}$	(25.06,58.67)	(7.21,10.53)

Table 2.2: Summary of calibrated model parameters for a normally distributed fiber model with $n_f = 30$ (see (2.14)). Fibrosa loss $\ell = 5.13 \times 10^{-4}$ and ventricularis loss $\ell = 8.01 \times 10^{-3}$. 95% confidence intervals computed via bootstrap are reported below the corresponding value. For all layers, $K = 2.2 \times 10^3$ kPa and $\mu = 478$ Pa.

We find the moment-curvature response of the bending simulation to be linear, for a midspan deflection loading of ± 1 mm, despite a prestressed initial state (per Sec. 2.4). We find $\mu = 478$ Pa results in $M/(I\Delta\kappa) \approx 5.3$ kPa.

Fiber distribution

To illustrate the significance of the fiber distribution model, we present two equibiaxial stretch results for the individual layers: 1) a single family of circumferentially oriented fibers ($n_f = 1$, $\sigma_f = 0°$ (2.14)) in Figure 2.6 top and 2) a normally distributed family of fibers with $n_f = 30$ in Figure 2.6 bottom. Unique parameters are fit for each model. Figure 2.7 is a close-up look at the response for low membrane stresses. We notice that the loss, $\ell(C)$, goes from 1.01×10^{-3} to 5.13×10^{-4} for the fibrosa and from 2.50×10^{-2} to 8.01×10^{-3} for the ventricularis, thus indicating a better fit.

We observe that the single fiber family model fails to capture the "kickback" response, despite being highly anisotropic. The distributed fiber model captures the "kickback" response and boasts a lower loss.

Trilayer composite biaxial stretch

Next, we look at the equibiaxial stretch response of the trilayer composite, with material parameters per Table 2.2 and no prestressing, presented in Figure 2.8 top. Note the poor fit

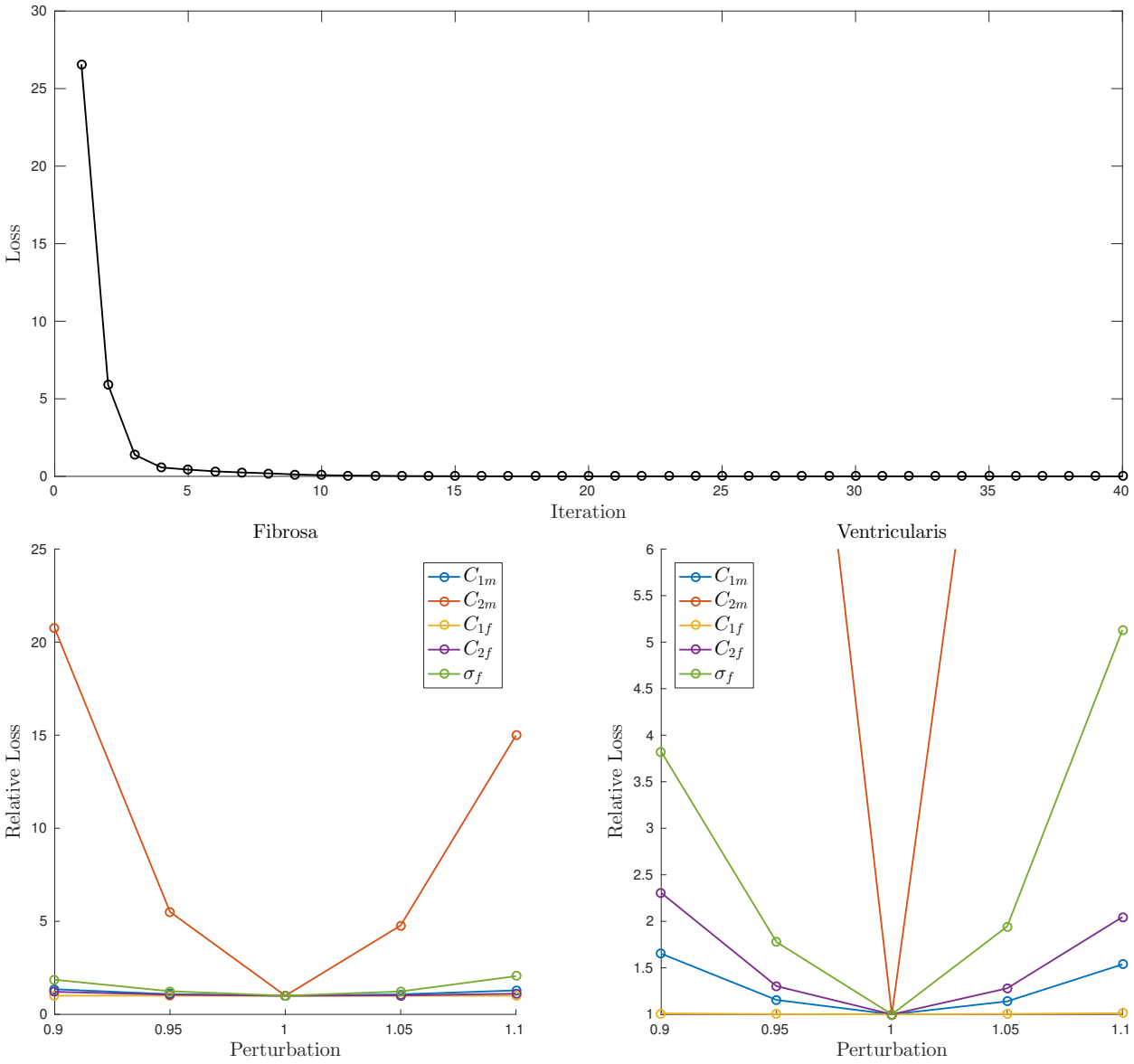

Figure 2.5: **Top**: Convergence of loss (2.22) using warm-start projected gradient descent with backtracking line-search. **Bottom** Perturbation analysis of parameters for fibrosa (left) and ventricularis (right). For clarity of exposition, the abscissa on the ventricularis plot is truncated.

despite each layer being consistent with its corresponding experiment.

We can reconcile this inconsistency by applying the prestressing procedure outlined in Sec. 2.3. We take the initial configuration of the fibrosa (i.e., the dimensions along the c and r directions) as a free parameter, which we tune to obtain the response in the bottom of Figure 2.8.

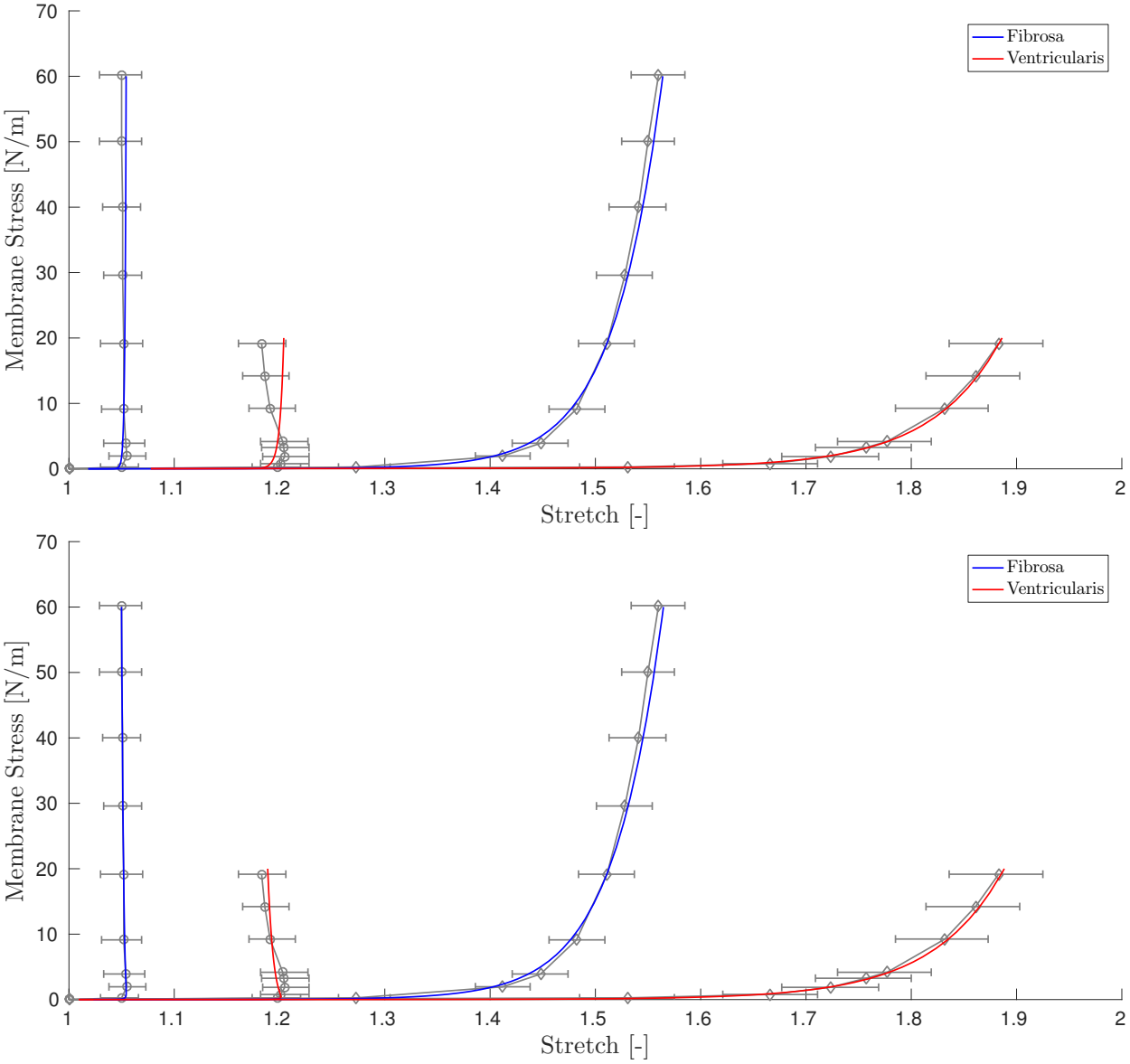

Figure 2.6: Equibiaxial stretch response of individual layers plotted against experimental data (gray with errorbars). The two left curves are the responses in the circumferential direction and the two right curves are the responses in the radial direction. **Top**: Single family of fibers: $n_f = 1$, $\sigma_f = 0°$. **Bottom**: Distributed family of fibers: $n_f = 30$, $\sim \mathcal{N}(0, \sigma_f)$, see Table 2.2 for σ_f values.

We find that an initial size of $9.05 \times 4.85 \times 0.145$ mm of the fibrosa results in the best response, with a loss $\ell = 1.71 \times 10^{-2}$ (as opposed to $\ell = 1.55 \times 10^{-1}$ for the non-prestressed case). It is worth remarking that due to the nature of our prestressing protocol, the "initial" (i.e., after prestressing but prior to loading) size of the AV specimen is $8.7 \times 5.3 \times 0.46$ mm.

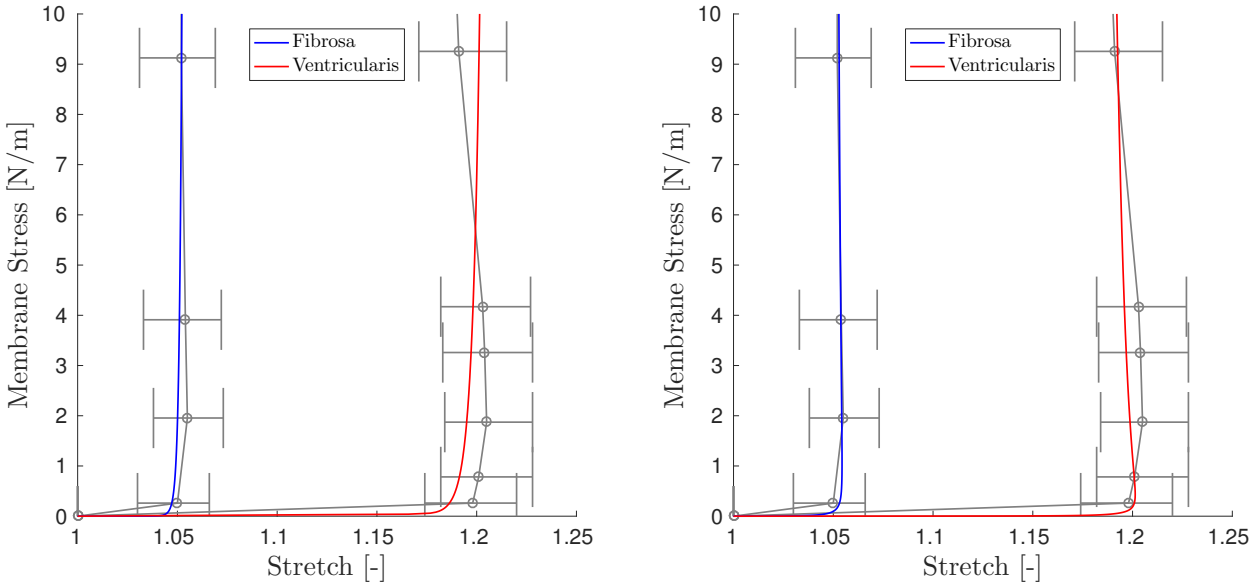

Figure 2.7: Close-up of circumferential response in Figure 2.6. **Left**: Single family of fibers: $n_f = 1$, $\sigma_f = 0°$. **Right**: Distributed family of fibers: $n_f = 30$, $\sim \mathcal{N}(0, \sigma_f)$.

2.5 Discussion

Fiber micromechanics

In Figure 2.6, we see that AV tissue exhibits a peculiar layer-scale "kickback" behavior in the circumferential direction, wherein increasing load initially results in increasing stretch, followed by a sustained decrease in stretch. We do not observe this behavior when the fibers are oriented in just the circumferential direction (top plot in Figure 2.6), despite an anisotropic material specification. We observe the "kickback" behavior in the bottom plot of Figure 2.6 when the distribution of fibers is explicitly included.

The "kickback" behavior is a result of the fibers, predominantly aligned in the circumferential direction, rotating into the radial direction, and "transfering" stiffness over. To see this more clearly, consider the deformation gradient at the maximum biaxial loading shown in Figure 2.1, $\boldsymbol{F} = \lambda_c \boldsymbol{e}_c \otimes \boldsymbol{e}_c + \lambda_r \boldsymbol{e}_r \otimes \boldsymbol{e}_r$, where $\lambda_c < \lambda_r$ are the circumferential and radial stretches, respectively. Take an arbitrary unit vector along a particular fiber, $\boldsymbol{m} = \cos(\theta)\boldsymbol{e}_c + \sin(\theta)\boldsymbol{e}_r$. The orientation of this fiber with respct to $\boldsymbol{e}_c$ is given by θ. The fiber transforms as $\boldsymbol{m}_t := \boldsymbol{F}\boldsymbol{m} = \lambda_c cos(\theta)\boldsymbol{e}_c + \lambda_r \sin(\theta)\boldsymbol{e}_r$ with the deformation. We can compute the deformed fiber's angle as:

$$|\theta_t| = \left|\text{atan}\left(\frac{\boldsymbol{e}_r \cdot \boldsymbol{m}_t}{\boldsymbol{e}_c \cdot \boldsymbol{m}_t}\right)\right| = \left|\text{atan}\left(\frac{\lambda_r}{\lambda_c}\tan(\theta)\right)\right| > |\theta|, \tag{2.25}$$

since $\lambda_r/\lambda_c > 1$ and arctangent is a monotonically increasing odd function. Thus, we see a geometric softening in the circumferential direction and a corresponding stiffening in the

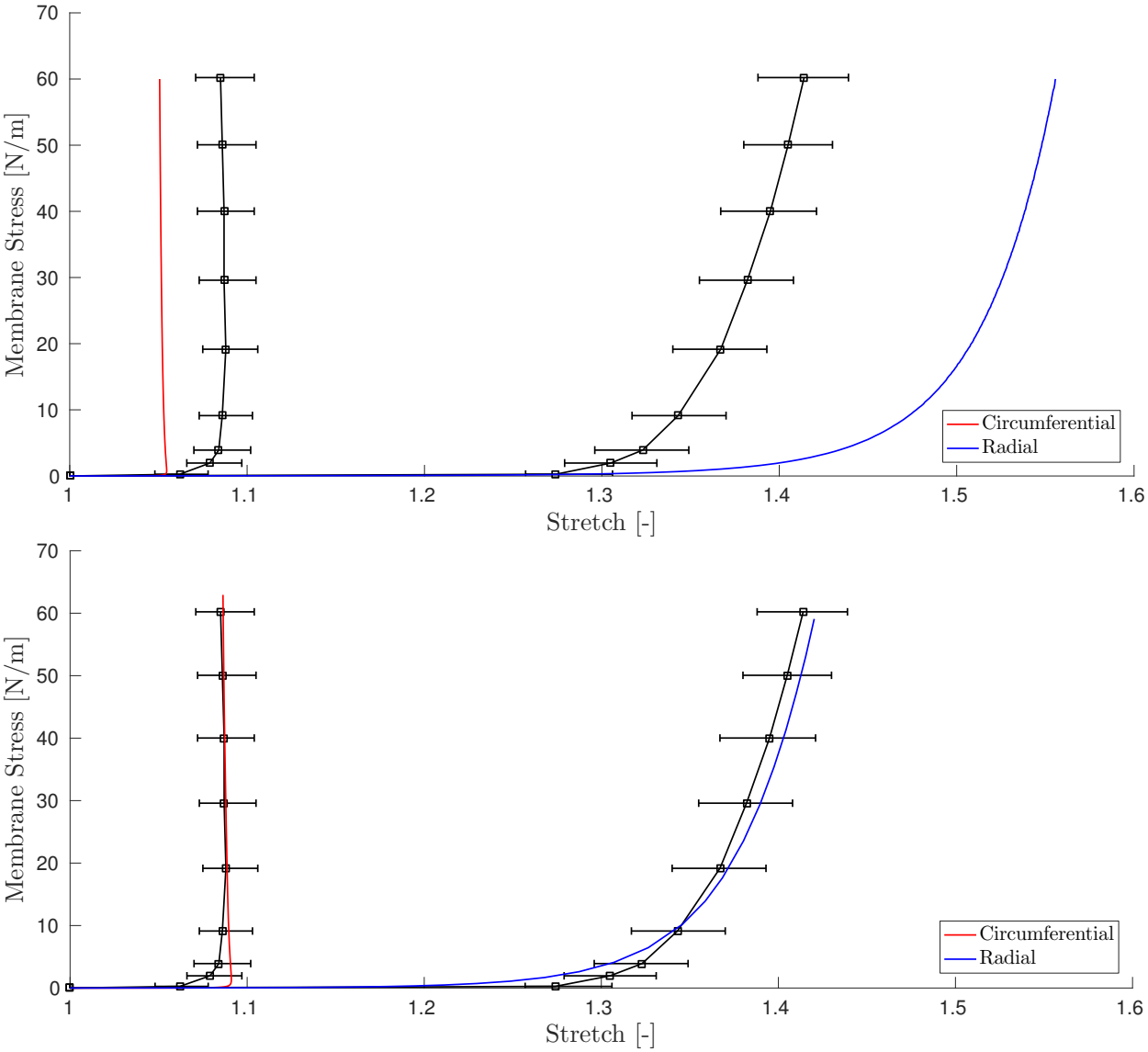

Figure 2.8: Equibiaxial stretch response of AV composite tissue with (bottom) and without (top) prestress.

radial directions, as the fibers rotate under the influence of the applied biaxial loading.

It is possible to capture this behavior with other models. For instance, the general Fung model [56] with appropriate choice of parameters can result in the same behavior for equibiaxial stretch. Our model, however, serves as an intuitive (and heuristic) understanding of the micromechanics by explicitly modeling the discrete fiber directions and tracking their respective rotations. Furthermore, this model allows us to model planar (span$\{\boldsymbol{e}_c, \boldsymbol{e}_r\}$) heterogeneity of the fibers.

Prestressing

Stella and Sacks [146] remark on a native prestress in AV tissue, as evidenced by the deformation of the fibrosa and ventricularis post-dissection. We observe that a model that lacks prestressing (Figure 2.8 top) fails to capture the AV composite behavior, despite consistent layer-scale behavior. When we apply a prestress (Figure 2.8 bottom), we observe a more consistent material response. We conclude that to properly model AV tissue response with layer-scale consistency, prestressing must be included.

Limitations

Prestressing

The main limitation of our model comes from the rather artificial prestressing, in the sense that we do not have the *exact* same before-and-after dimensions as in the experiments of [146]. The fibrosa exhibits a corrugated structure when part of the AV composite, but becomes flat when removed, indicating a buckling phenomenon. We contend that to have a fully consistent model, the buckling micromechanics of the collagen fibers in the fibrosa would need to be considered.

Affine fiber transport

We have assumed that the fibers deform affinely, but it is known that this is not always true [72, 25]. Further study is required to properly account for non-affine fiber transport.

Equibiaxial stretch

By restricting our attention to equibiaxial stretch experiments, we risk overfitting the model. Indeed, biaxial stretch experiments alone may be insufficient for fully characterizing material response [78]. However, the lack of consistent, layer-specific data for AV tissue leaves few options. Though we have incorporated the bending experiments to better capture the true material response. Note that our general modeling framework makes it relatively straightforward to efficiently fit to larger datasets, should they become available.

2.6 Conclusion

In this Chapter we presented we presented the continuum mechanics framework and a method to consistently model AV tissue. We demonstrated the significance of modeling the normal distribution of fibers in the microstructure (in corroboration of the findings of Billiar and Sacks [16]). We further demonstrated the need for appropriate prestressing of the AV composite to achieve consistent trilayer mechanical behavior. Our demonstration, however, did not investigate the complex stress state associated with the buckling of the fibrosa in the AV

composite, a point that warrants further study. In the sequel, we will apply our framework and methodology in a multiscale setting.

Chapter 3

Multiscale Leaflet Model

In Chapter 1 we introduced mechanotransduction, the process by which biological cells respond to mechanical stimuli and activate biochemical pathways, and we discussed the essential role of the valvular interstitial cells (VICs) in overall aortic valve (AV) function. Armed with the biomechanical modeling tools we developed in Chapter 2, we now move on to present a multiscale modeling technique (by way of computational homogenization, also known as FE^2), to incorporate the biomechanics of VICs into AV organ modeling.

Huang [79] proposed the VIC aspect ratio as a mechanical measure of cellular mechanotransduction activity and performed experiments that investigated the metric in response to loading of aortic valve leaflet tissue to *in vivo* physiological levels. Numerical simulations that mimic these experiments were carried out but limited to 2D and uncoupled 3D models (i.e., no interaction between the macroscale and microscale).

In this Chapter, we apply FE^2 to AV leaflet tissue in 3D to study the mechanical behavior of the VICs in response to organ-scale mechanical loading. Our simulations demonstrate a viable method for fully multiscale modeling of aortic valve tissue. We also find that the "apparent" VIC aspect ratio observed in experiments may not necessarily be consistent with the actual 3D deformations of the cells.

3.1 Introduction

Background

Aortic valve (AV) function and disease are a result of processes occurring at the cellular scale. Biochemical pathways are activated from mechanical feedback loops between the valvular interstitial cells (VICs) and the AV leaflet tissue.[158] In an effort to better understand the nature of AV disease, researchers have been exploring the central role of VICs (see Chapter 1). In particular, a series of studies pioneered by Huang *et al* have been aimed at modeling multiscale behavior of valve tissue [79, 80, 172, 82].

Huang et al [80] looked at the VIC deformation in 2D in response to physiological loading

at the tissue level. Weinberg and Mofrad [172] expanded to 3D and incorporated the aortic valve as an organ. Missing from the literature, however are coupled multiscale models, i.e., models that allow for two-way interaction between the disparate length scales. Naturally, a meaningful model of the full resolution of the AV, incorporating the cells that make up its microstructure, is a computationally intractable problem. An alternative is computational homogenization, sometimes known as FE^2, where a statistical representation of the microstructure (the so-called representative volume element) is embedded into a macroscale model.

Computational homogenization is a viable way of coupling multiscale behavior [91]. We use this approach to study the VIC aspect ratio (VICAR), proposed by Huang [79] as a suitable metric for VIC mechanotransduction, the process in which cells activate biochemical pathways in response to mechanical stimuli. We are able identify that the perceived aspect ratio from experiments may not be consistent with the actual 3D VIC deformations. Wth this methodology, we expose a framework for more complex multiscale and multiphysics AV models.

Aortic valve function

Details regarding AV physiology are given in Chapter 1. We briefly revisit them here. The AV complex consists of the aortic root, the sinus, the leaflets, and the ascending aorta, as depicted in Fig. 3.1. Our main focus here are the leaflets (or cusps), colored in Fig. 3.1.

Healthy AVs have three leaflets that open in close to allow blood flow from the ventricle into the ascending aorta and prevent retrograde flow. During the cardiac cycle (illustrated in Fig. 3.2), blood flows in from the left atrium into the left ventricle during diastole, and the AV leaflets open (close) at the beginning (end) of systole.

Huang carried out a series of *in vitro* experiments to measure the VIC aspect ratio (VICAR) in response to AV tissue loading during the cardiac cycle. AV leaflet samples were fixed in a tank and a pressure head was applied at five different levels per Table 3.1. The average VICAR was then measured at each pressure by image processing procedures of sections through the tissue section in the $c \times h$ plane. The authors note that the VICAR reported is the observed value, i.e., the apparent 2D elliptical aspect ratio that, in general, is not concentric with the presumed ellipsoidal shape. For further details regarding the experimental procedure, see [79].

Load step	1	2	3	4	5
Pressure	1	2	4	60	90

Table 3.1: Pressure loading protocol in mmHg.

Note that the net pressure load is on the *aortic* side of the leaflet. Physiologically this corresponds to the period between systole and diastole (Fig. 3.2), right after the valve closes and the transvalvular pressure is the greatest.

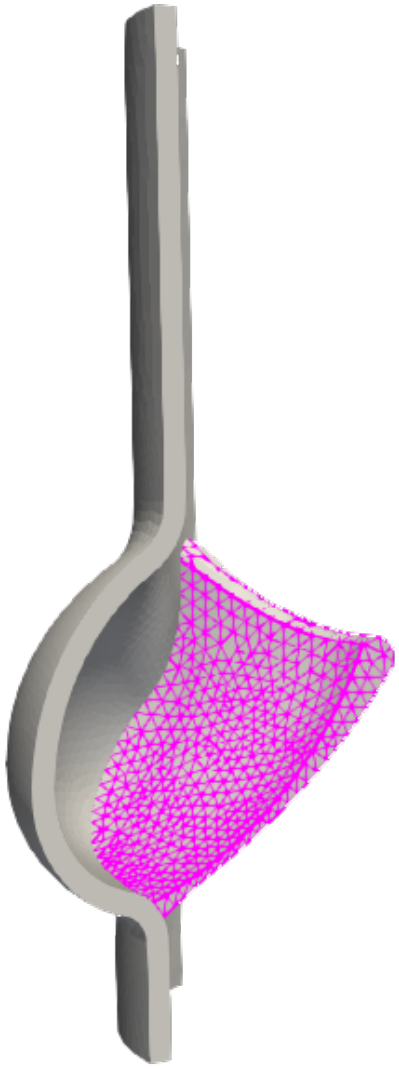

Figure 3.1: One-sixth of a symmetric idealized aortic valve geometry as obtained from Weinberg and Mofrad [172]. The leaflet is highlighted. Rendering generated with ParaView [1].

3.2 Multiscale Modeling

The assumptions made throughout are discussed in Sec. 3.4

Computational homogenization

We begin with (2.6), the weak form statement of the FE problem. The integrals in (2.6) are computed via numerical quadrature. At each quadrature point, $\boldsymbol{P}$ is generally obtained

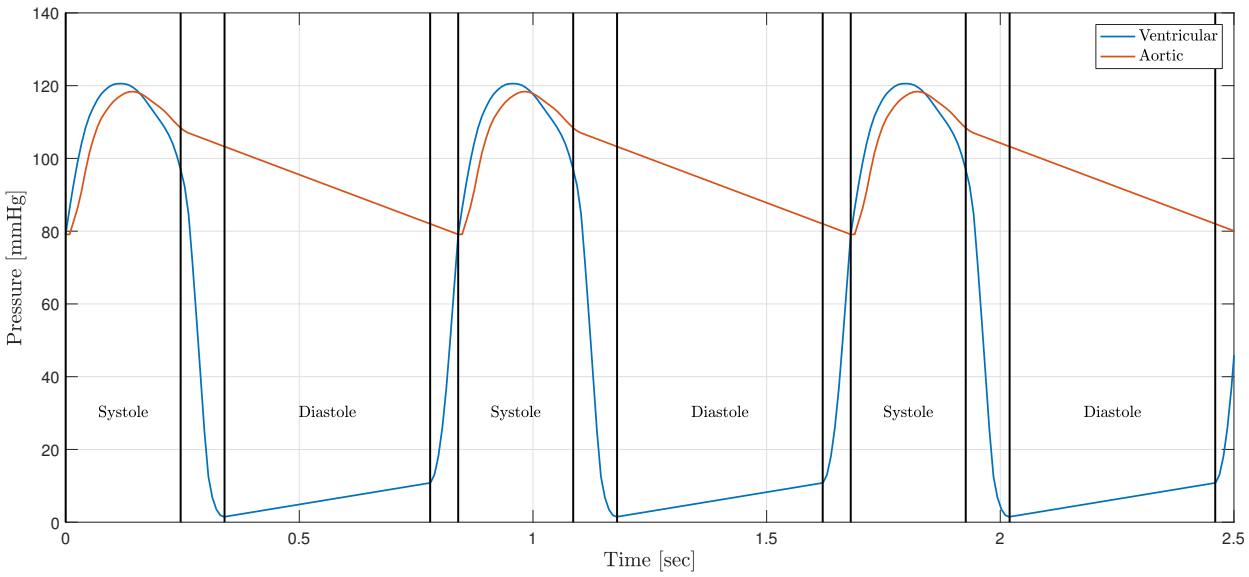

Figure 3.2: Aortic valve cardiac cycle pressures as adaptedfrom [160].

from a constitutive model (for hyperelastic materials, viz. (2.2)).

In computational homogenization, or FE^2, the macroscopic stress, now denoted $\boldsymbol{P}^M$, is obtained from an embedded FE problem representative of the microstructure of the material, referred to as the representative volume element (RVE). The macroscopic deformation gradient, now denoted as $\boldsymbol{F}^M$, is passed from the macroscale model to the RVE (with domain given by Ω) as a constraint condition, the energy of the RVE is minimized (e.g., an FE solution is obtained for the RVE) subject to the condition that the volume average of the pointwise RVE deformation gradient, $\boldsymbol{F}^m$, is equal to the imposed macroscopic deformation gradient $\boldsymbol{F}^M$. This procedure is depicted in Fig. 3.3. The resulting stress and tangent stiffness are computed from the Hill-Mandel principle:

$$\boldsymbol{P}^M \cdot \delta \boldsymbol{F}^M = \frac{1}{V(\Omega)} \int_\Omega \boldsymbol{P}^m \cdot \delta \boldsymbol{F}^m \, dV, \tag{3.1}$$

where, as introduced, the superscript M denotes macroscale and m denotes microscale.

We now outline the homogenization procedure (see Kouznetsova [91] for a comprehensive treatment). We begin by imposing $\boldsymbol{F}^M$ on $\partial\Omega$, the boundary of the RVE. We partition the displacements accordingly

$$\boldsymbol{u} = \overline{\boldsymbol{u}_d \cup \boldsymbol{u}_f}, \quad \boldsymbol{u}_d \cap \boldsymbol{u}_f = 0. \tag{3.2}$$

We refer to $\boldsymbol{u}_f$ as the free displacements in the RVE domain and

$$\boldsymbol{u}_d = (\boldsymbol{F}^M - \boldsymbol{I})\boldsymbol{X}, \quad \forall \boldsymbol{X} \in \partial\Omega. \tag{3.3}$$

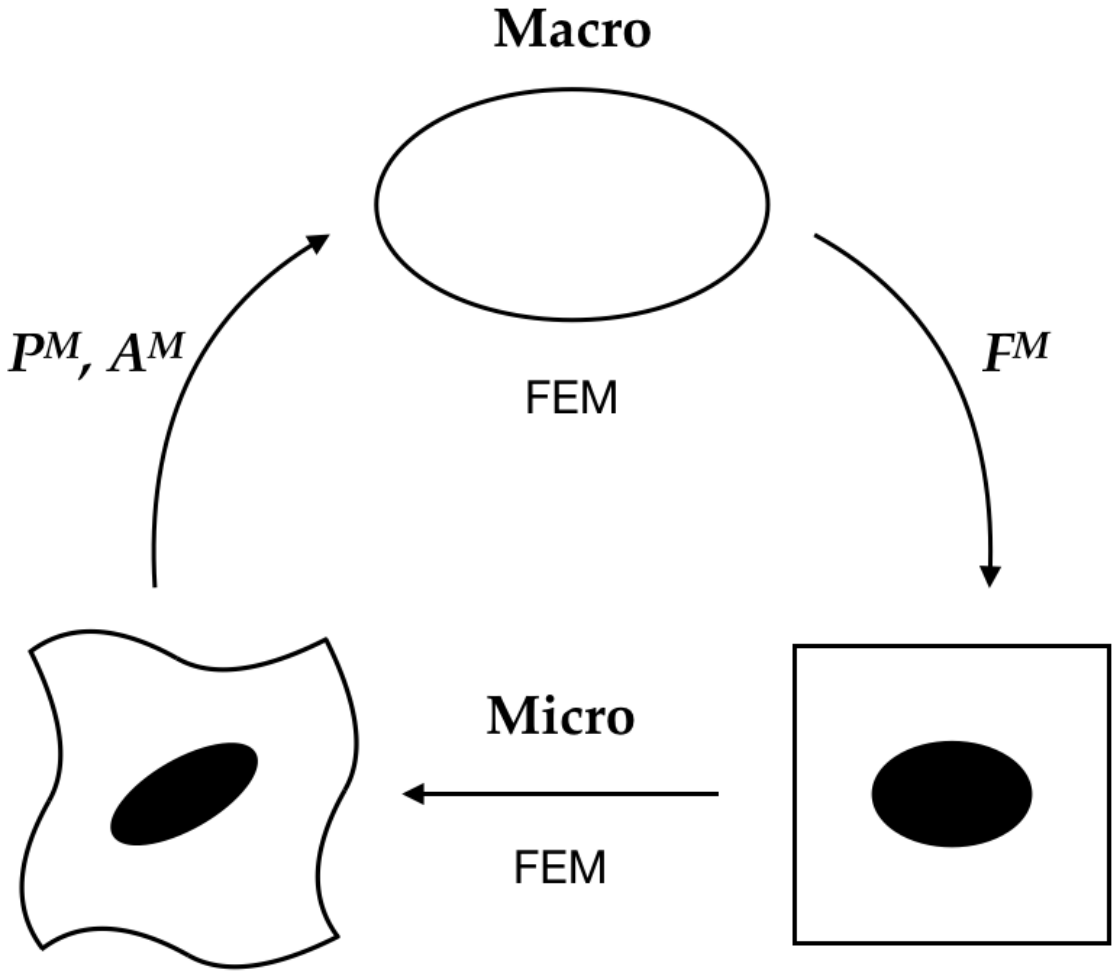

Figure 3.3: Computational homogenization, i.e. FE^2. The macro problem passes the deformation gradient $\boldsymbol{F}$ to the RVE (micro problem), where (2.1) is solved. The homogenized stress and tangent (as given by (3.4) and (3.7)) are then computed and passed up to the macro problem. The process is iterated typically as in (2.9). This graphic is adapted from Kouznetsova [91].

The free displacements are computed by satisfying (2.1) for the RVE, under the assumption of an appropriate material description[1] (e.g., hyperelasticity), using a standard FE procedure as in Sec. 2.2. Application of (3.1) leads to an expression for the homogenized stress:

$$\boldsymbol{P}^M = \frac{1}{V(\Omega)} \int_\Omega \boldsymbol{P}^m \, dV. \tag{3.4}$$

[1] An interesting extension is a two-stage FE^2 procedure with a "nanoscale" RVE.

Next we turn to an expression for the homogenized tangent stiffness. We begin by forming the Schur complement of the partitioned tangent stiffness as given by (3.2):

$$\boldsymbol{K}_c = \boldsymbol{K}^m_{dd} - \boldsymbol{K}^m_{df}(\boldsymbol{K}^m_{ff})^{-1}\boldsymbol{K}^m_{fd}. \tag{3.5}$$

We define the order-4 tangent stiffness $\boldsymbol{A}^M$ that satisfies the variational inner product

$$\delta\boldsymbol{P}^M = \boldsymbol{A}^M \cdot \delta\boldsymbol{F}^M. \tag{3.6}$$

It is not difficult to show that application of (3.1) reveals

$$\boldsymbol{A}^M = \frac{1}{V(\Omega)}\sum_{A=1}^{n_d}\sum_{B=1}^{n_d}\left(\boldsymbol{X}^A \otimes \boldsymbol{K}_c^{AB} \otimes \boldsymbol{X}^B\right)^L, \tag{3.7}$$

where n_d is the number of boundary nodes, and thus $\boldsymbol{K}_c^{AB}$ refers to the 3 degrees of freedom at nodes A, B leading to $\boldsymbol{A}^M \in \mathbb{R}^{3\times3\times3\times3}$. $(D_{ijkl})^L = D_{jikl}$ is the left conjugation of a 4-tensor $\boldsymbol{D}$.

RVE boundary conditions

The Dirichlet boundary condition specified in (3.3) is not unique. In fact, any boundary conditions that are compatible with (3.1) are feasible. Other examples include traction, periodic, and Taylor boundary conditions (where $\boldsymbol{F}^M$ is imposed everywhere in Ω, not just the boundary). As a rule of thumb, Taylor and Dirichlet boundary conditions tend to overestimate the stiffness of the RVE, traction boundary conditions tend to underestimate the stiffness, and periodic boundary conditions seem to be closer to the ground truth. The latter, however, demands a structured mesh which may not be possible (as in our case).

Taylor boundary conditons are used in the remainder of this chapter and so we discuss briefly. In (3.2) we have $\boldsymbol{u}_f = \emptyset$ and thus in (3.5) $\boldsymbol{K}_c = \boldsymbol{K}^m_d = \boldsymbol{K}^m_T(\boldsymbol{F}^M)$, the ordinary tangent stiffness of the global micro problem at the deformation state $\boldsymbol{F}^M$ (see (2.10)). See Sec. 3.4 for further discussion of the RVE boundary conditions.

FE model

We use FEAP[159] to conduct the FE^2 analysis. The macroscale model is the AV leaflet and the RVE is a VIC embedded in the extracellular matrix (ECM).

Macroscale model

Our geometric representation of the AV leaflet is shown in Fig. 3.4 via the mesh. Dimensions are obtained from Hajali et al [69], Weinberg and Mofrad [172], Huang [79], and Stella and Sacks [146]. Eight node mixed-formulation elements are used in a hexahedral mesh generated with FEAP built-in tools and a custom algorithm. We exploit symmetry and model only half

of the leaflet with appropriate boundary conditions at the symmetry plane. The remaining edges around the leaflet are fixed as in the experiments.

As is typical in AV leaflet literature, we define the circumferential, radial, and transmural (CRT) curvilinear basis. Referencing Fig. 3.4, the circumferential direction is tangential to the curved surface and orthogonal to the symmetry plane, the radial direction is tangential to the curved surface and orthogonal to the circumferential direction, and the transmural direction is orthogonal to the curved surface through the thickness of the leaflet.

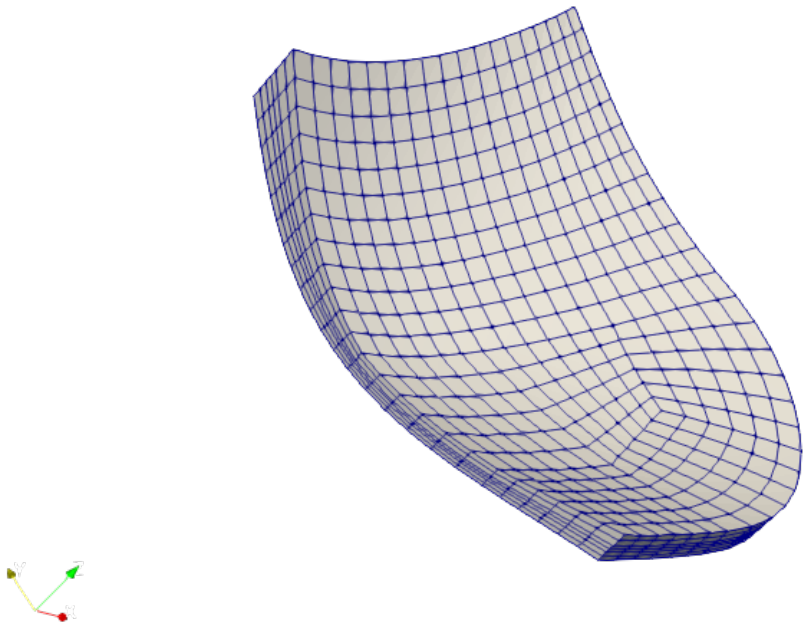

Figure 3.4: Macroscale AV leaflet (symmetric) mesh generated with a custom algorithm and FEAP built-in tools. Paraview is used for visualization [1].

An important characteristic of the AV leaflet is its natural curvature (hence the name cusp). Exact data on the curvature of the cusp used in the experiments of Huang is not available, so we approximate the surface curvature with the following out-of-plane (OOP) surface deformation:

$$\omega(x,y) = \frac{r\rho^2}{\pi^2}\left(\cos\left(\frac{\pi}{\rho}\left(x-x_0\right)\right)+1\right)\left(\cos\left(\frac{\pi}{\rho}\left(y-y_0\right)\right)+1\right), \tag{3.8}$$

where r, ρ are parameters that control the shape and are dictated by the experimental geometry. (x_0, y_0) is the planar center of curvature in a Cartesian system. We define $x_0 = 0$ for symmetry, leaving y_0 as a free parameter. Note that (3.8) defines a mapping between the Cartesian basis and the CRT basis.

The trilayer structure of the AV leaflet tissue is explicitly modeled with three discrete layers (ventricularis, spongiosa, and fibrosa). Interconnecting fibers through the thickness are modeled with perfectly bonded layers [21, 139]. The in-plane fibers are embedded in the RVE via (2.14), but the OOP orientations are computed from (3.8) in the macro-scale mesh and passed down to each RVE. Note that due to lack of available data, we do not prestress the layers as in Sec. 2.4.

Microscale model (RVE)

The geometric representation of the RVE is shown in Fig. 3.5 via the mesh. Mixed-formulation four node tetrahedral elements are used in an unstructured mesh generated with the open-source package Iso2mesh [47]. A coarse mesh (Fig. 3.5 right) is chosen for computational efficiency (see Sec. 3.4 for a discussion).

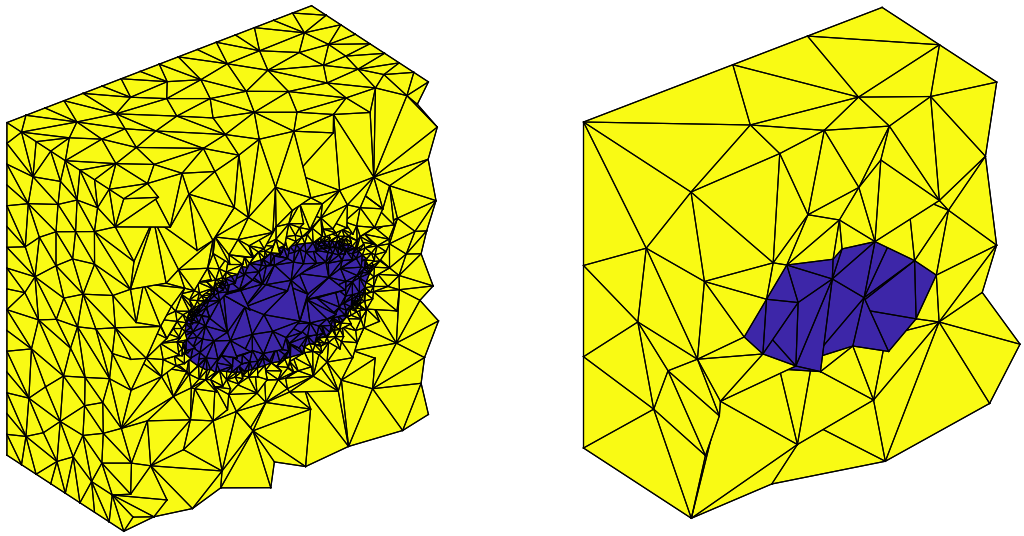

Figure 3.5: **Right**: Low-fidelity RVE mesh used for FE^2 computation. **Left**: High-fidelity RVE mesh used for post-processing calculation. Both meshes enforce the same volume ratio. Meshes generated and visualized with Iso2mesh [47].

The VIC is approximated as an ellipsoid, with aspect ratios (in CRT coordinates): $C/T = 1.8$, $C/R = 1.3$, and a major axis length of 9.6 μm. The VIC volume ratio (VR) is approximated from Huang et al [80] but allowed to vary (see Sec. 3.3). We assume the cell behaves as a Neohookean material, i.e., (2.14) with $C_{1m} = C_{2m} = C_{1f} = C_{2f} = 0$, $\mu = 400$ Pa and $K = 2.2$ MPa [79] and is perfectly bonded with the ECM. The ECM material is given by (2.14) with parameters defined in Table 3.2. We use Taylor boundary conditions (see the previous section), i.e., the deformation gradient is imposed everywhere in the domain. Let $\boldsymbol{F}_t^k$ be the deformation gradient t and iteration k passed to an RVE (Ω). Then the displacement field is

$$\boldsymbol{u}_t^k(\boldsymbol{X}) = (\boldsymbol{F}_t^k - \boldsymbol{I})\boldsymbol{X}, \quad \forall \boldsymbol{X} \in \Omega. \tag{3.9}$$

VICAR computation

In the spirit of the experiments, we fix the macroscale model around the edges (with the exception of the symmetry boundary conditions) and apply a uniform pressure loading (Table 3.1) on the aortic side (with the curvature). Note that the large deformation necessitates the use of convecting "follower" pressure loads [188].

We compute the VICAR by tracking the deformation of nodes at the ends of the major and minor axes (circumferential and transmural directions, respectively) of the VIC during the loading. To simulate the "apparent" ratio, we track nodes at the ends of the major and minor axes of the elliptical projection of the ellipsoidal VIC on a cutting plane (Fig. 3.6). The cutting plane is a subset of the circumferential-transmural plane and convects with the deformed to maintain the same reference configuration. The initial cutting plane is defined with a random (normal) perturbation from the center of the ellipsoid.

Let $\mathcal{P}_0$ define the reference cutting plane, then

$$\mathcal{P}_t = \boldsymbol{\varphi}_t(\mathcal{P}_0). \tag{3.10}$$

We compute the VICAR in a post-processing step.of the analysis. The deformation gradients at each quadrature point in space and time are applied to a higher fidelity RVE mesh (a la Fig. 3.6). Furthermore, we randomly perturb the location and orientation of the VIC inside the RVE for each quadrature point. We assume the major axis of the ellipsoid is randomly oriented in a normal cone about the circumferential direction. Let

$$\boldsymbol{\mathcal{E}} = [\boldsymbol{a}_c, \boldsymbol{a}_r, \boldsymbol{a}_t], \tag{3.11}$$

represent the axes of the ellipsoid with $\boldsymbol{\mathcal{E}}^T\boldsymbol{\mathcal{E}} = \boldsymbol{\mathcal{E}}\boldsymbol{\mathcal{E}}^T = \boldsymbol{I}$. Then we define the rotated axes as,

$$\boldsymbol{\mathcal{E}}' = \boldsymbol{R}_{cr}(\theta_2)\boldsymbol{R}_{ct}(\theta_1)\boldsymbol{\mathcal{E}}\boldsymbol{R}_{ct}(\theta_1)^T\boldsymbol{R}_{cr}(\theta_2)^T, \tag{3.12}$$

where

$$\boldsymbol{R}(\theta)_{ab} := \cos(\theta)(\boldsymbol{e}_a \otimes \boldsymbol{e}_a + \boldsymbol{e}_b \otimes \boldsymbol{e}_b) + \sin(\theta)(\boldsymbol{e}_b \otimes \boldsymbol{e}_a - \boldsymbol{e}_a \otimes \boldsymbol{e}_b), \tag{3.13}$$

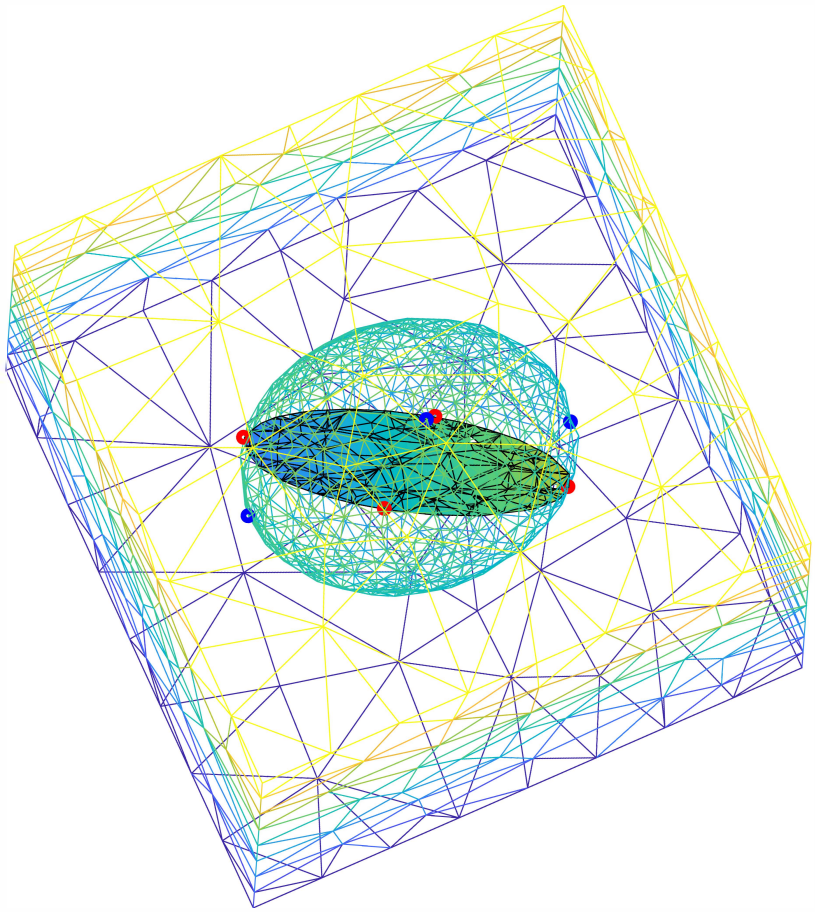

Figure 3.6: Visualization [47] of VICAR measurement. Blue circles indicate actual VICAR while red circles indicate "apparent" VICAR as measured via the projection of the ellipsoidal cell on thecutting plane that convects with the deformation.

is a counterclockwise planar rotation matrix and

$$\theta_i \sim \mathcal{N}(0, \sigma_\theta), \tag{3.14}$$

are angles drawn from a zero-mean normal distribution. The parameters σ_θ and the volume ratio of the cell VR are discussed in the sequel.

Remark

Note that with Taylor boundary conditions, we only need to track the extrema of the VIC ellipsoid during the deformation. We include the RVE mesh to illustrate a more general

procedure for VICAR computations.

3.3 Results

RVE material parameter fitting

We fit the hyperelastic material in the RVE ECM, given by (2.14), to experimental tissue equibiaxial stretch data [79]. The fitting procedure is described in Sec. 2.3. Fig. 3.7 demonstrates the fit and Table 3.2 summarizes the parameters. Note that the layers are not prestressed as in Sec. 2.3.

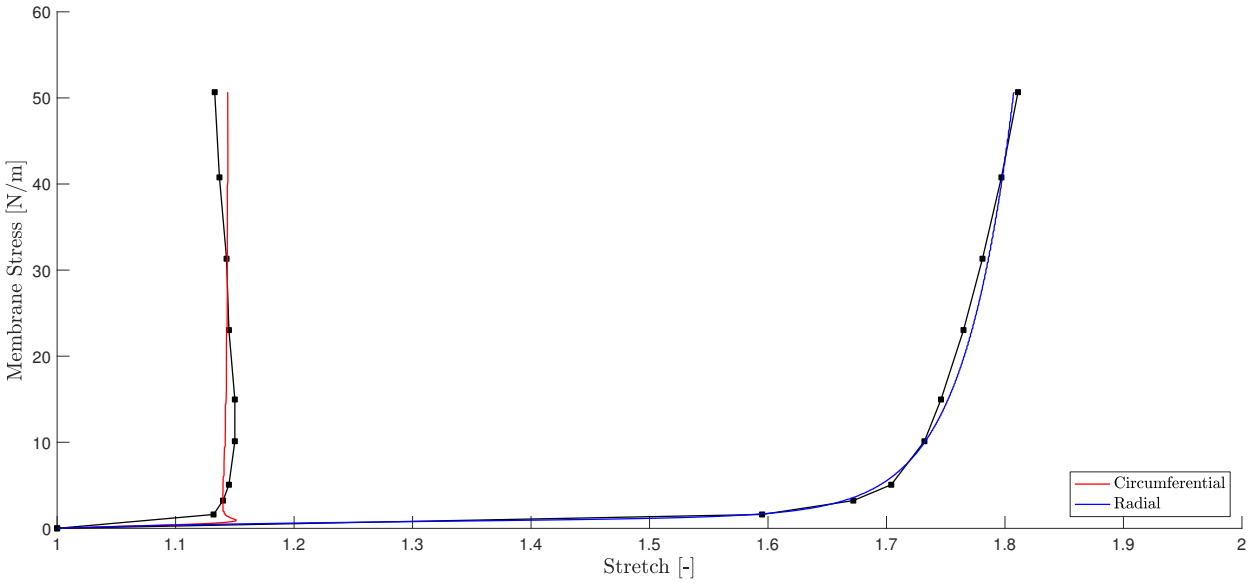

Figure 3.7: Equibiaxial membrane stress vs stretch for RVE material (colored: red is circumferential and blue is radial) and experimental data (black). See Sec. 2.3 for details regarding the fitting experiment and procedure.

Model	C_{1m} [Pa]	C_{2m} [-]	C_{1f} [Pa]	C_{2f} [-]	σ_f [°]
Fibrosa	4.72×10^{-2}	6.7	16.31	43.19	0.64
Ventricularis	0.25	0.39	1.51	3.63	9.71

Table 3.2: Summary of calibrated model parameters (see (2.14)). $\mu = 1.62$ kPa and $K = 2.2$ MPa. $C_{1m} = C_{2m} = C_{1f} = C_{2f} = 0$ for the spongiosa.

Mesh convergence

Macroscale

A mesh objectivity study is summarized in Fig. 3.8. The sufficiently converged mesh size represented by the middle point is chosen for computational considerations.

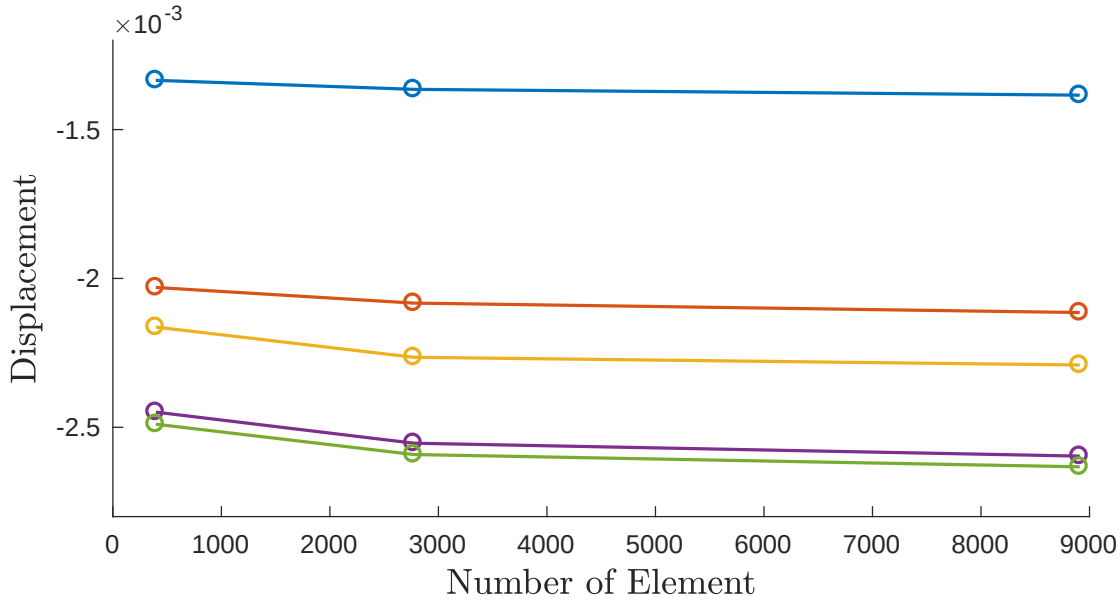

Figure 3.8: Convergence study for the macroscale mesh. Each curve represents displacements (in the belly region of the leaflet) at the load steps in Table 3.1. The mesh size represented by the middle point is chosen for computational considerations.

Microscale

Convergence of the embedded RVE (Fig. 3.5 right) in the FE^2 procedure is not of interest as it is intentionally downsampled. The postprocessing high-fidelty mesh (Fig. 3.5 left) mesh is relatively straightforward because we impose deformations everywhere in the domain (Taylor boundary conditions). Our quantity of interest is the VICAR, so the mesh must be sufficiently dense such that there is high probability that nodes are close enough to the apexes of the ellipsoid in the (randomized) unstructured tetrahedral mesh generation. We control the mesh density with a parameter that enforces a maximum element area on the surface of the ellipsoid, A_{max}, in the Delauanay triangulation [170].

FE^2 result

Simulations were tested on an in-house 32 processor cluster, Iron, and run on 60 processors of the 8,109 cluster SAVIO.[2] Each simulation ran for approximately 20 hours on the latter.

Fig. 3.9 shows the deformed shape at the five steps of the loading protocol defined in Table 3.1. We compute an average Jacobian in all the elements throughout the loading of $J \approx 1$, within 1.5%, indicating the desired quasi-incompressible behavior.

VICAR result

The VICAR plots are computed from the RVEs at every gauss point in the elements along the symmetry plane: a total of $144 \times 8 = 1152$ RVEs. The average is reported, and where shown, error bars represent standard deviation. Note that the authors of the experimental data do not specify whether their error bars represent one standard deviation or one standard error.

Throughout this discussion, a two-tailed t-test is used to test significant differences in means. We use the term *significant* to indicate that the p-value is $p < 0.05$ for the t-test, i.e., the difference in means is statistically significant

Fig. 3.10 shows the VICAR for $\sigma_\theta = 5^\circ$ and volume ratio VR=0.01. The red curve indicates "apparent" VICAR and blue curve is the actual VIC aspect ratio (see Fig. 3.6 and the corresponding discussion). The black curve is experimental data [80]..

Fig. 3.11 demonstrates the effect of varying the parameters σ_θ and volume ratio (VR) on the "apparent" VICAR. We only observe a *significant* for $\sigma_\theta = 20^\circ$ vs $\sigma_\theta = \{5^\circ, 10^\circ\}$, with a remarkable decrease in the former. No *significant* variation is found for the VR over two orders of magnitude.

Next we briefly look at the initial cusp curvature defined by (3.8). Fig. 3.12 demonstrates the VICAR for y_0, as a fraction of the size parameter r (e.g., an offset of 10% $\implies$ $y_0 = 0.1r$). *Significant* but small differences are observed throughout. We note that for large values of y_0, convergence issues in the FE problem are encountered.

Finally, Fig. 3.13 demonstrates the VICAR in each layer. *Significant* differences are observed everywhere except between the spongiosa and ventricularis at low pressures. The fibrosa demonstrates a larger VICAR, consistent with experimental findings.

3.4 Discussion

Macroscale model

We have designed a set of simulations to mimic the experiments of Huang [79], namely, the pressurization of a "fixed" valve leaflet, loaded from the aortic side. This corresponds to the

[2] http://research-it.berkeley.edu/services/high-performance-computing

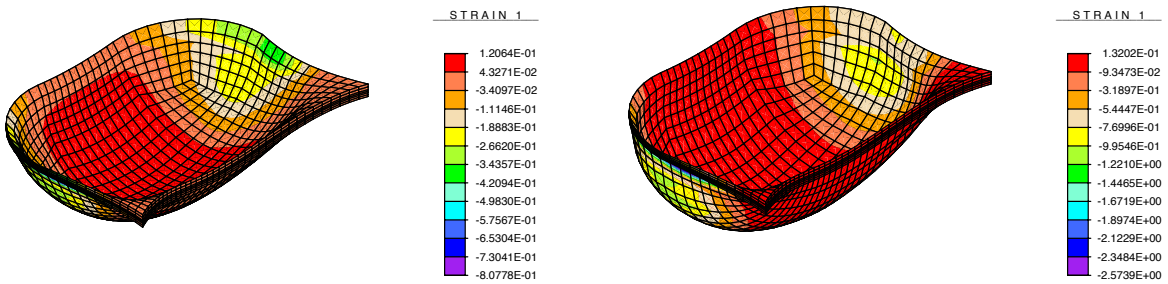

(a) 1 mmHg. (b) 2 mmHg.

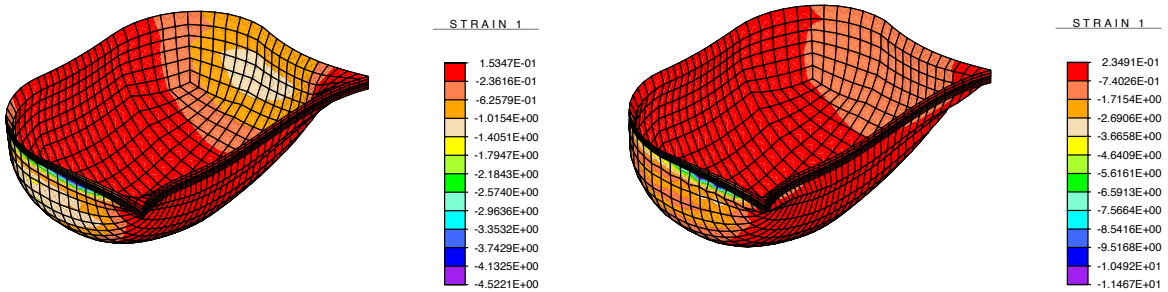

(c) 4 mmHg. (d) 60 mmHg.

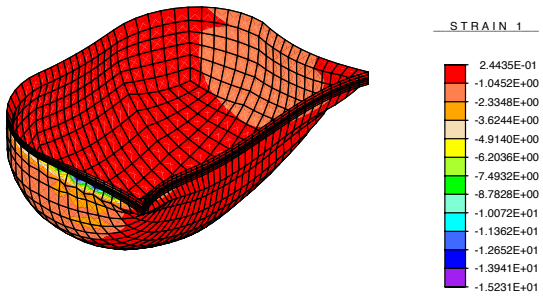

(e) 90 mmHg.

Figure 3.9: Leaflet deformation under load protocol defined in Table 3.1.

region in the cardiac style between systole and diastole (Fig. 3.2) where the transvalvular pressure is the largest.

These boundary conditions represent *in vitro* experiments rather than the proper *in vivo* conditions. They allow us to simulate physiological states in the laboratory. The nature of

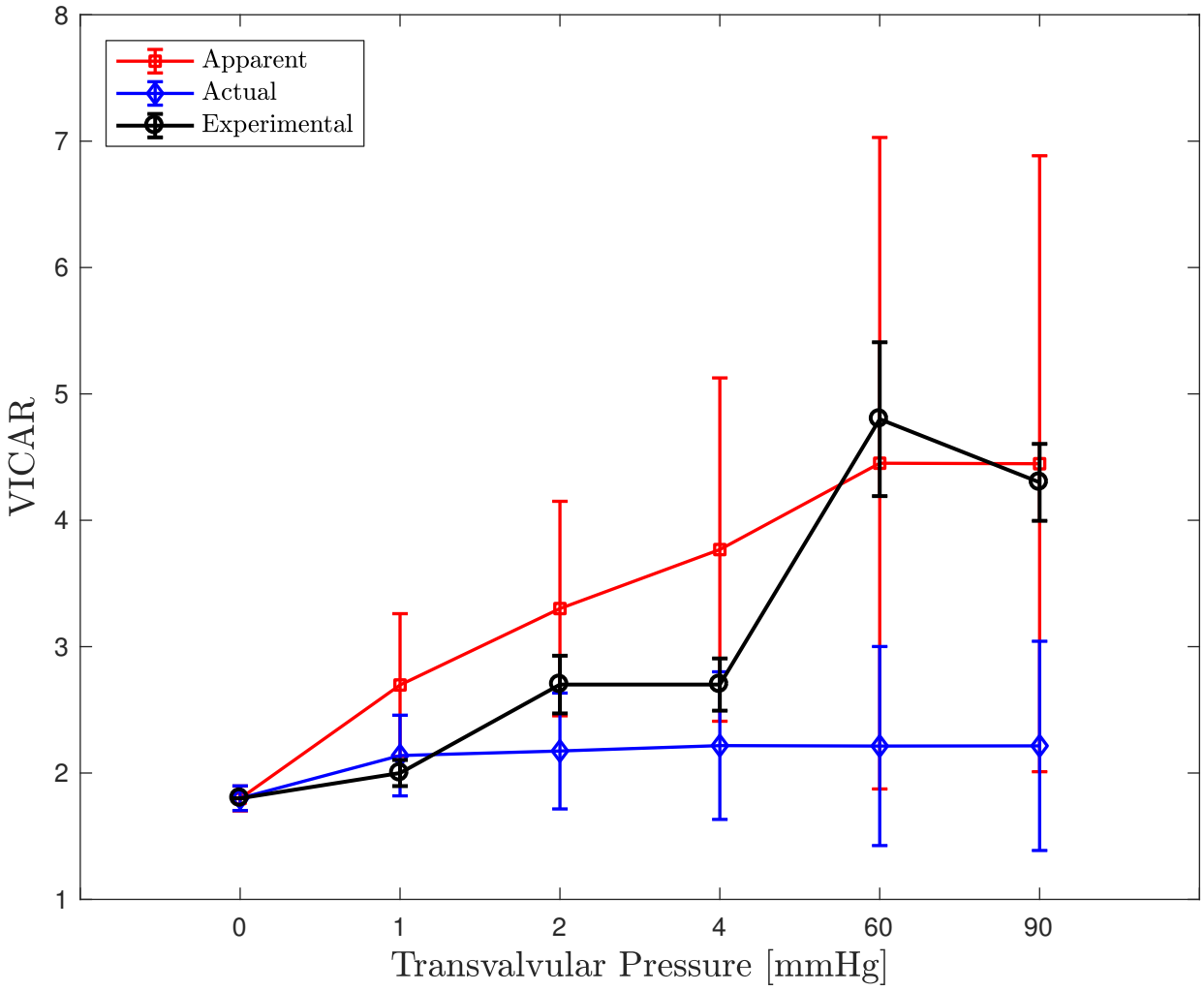

Figure 3.10: VICAR result as an average of 1156 RVEs measured along the radial direction in the center of the leaflet. One standard deviation errorbars are shown. Red curve indicates "apparent" VIC aspect ratio as measured *a la* Sec. 3.2 and blue curve is the actual VIC aspect ratio. Black curve is experimental data from Huang [80].

the fixed boundary conditions, including the "free" coaptation edge, results in a "balloon-inflation" like response, as seen in Fig. 3.9. The response is consistent with the material response in Fig 3.7. Low pressure (load) results in large deformation in the compliant regime. The tissue quickly stiffens and we see only small changes in deformation for larger increasing loads. Note that the tissue is not prestressed as in Chapter 2, but we saw similar behavior in Sec. 2.4 for prestressed tissue.

The initial curvature also plays a role in the response of the tissue. In particular, we encountered convergence issues for variations of the parameters in (3.8). However, without "patient-specifc" geometry, the best we can hope for is an aggregate consistent result, which

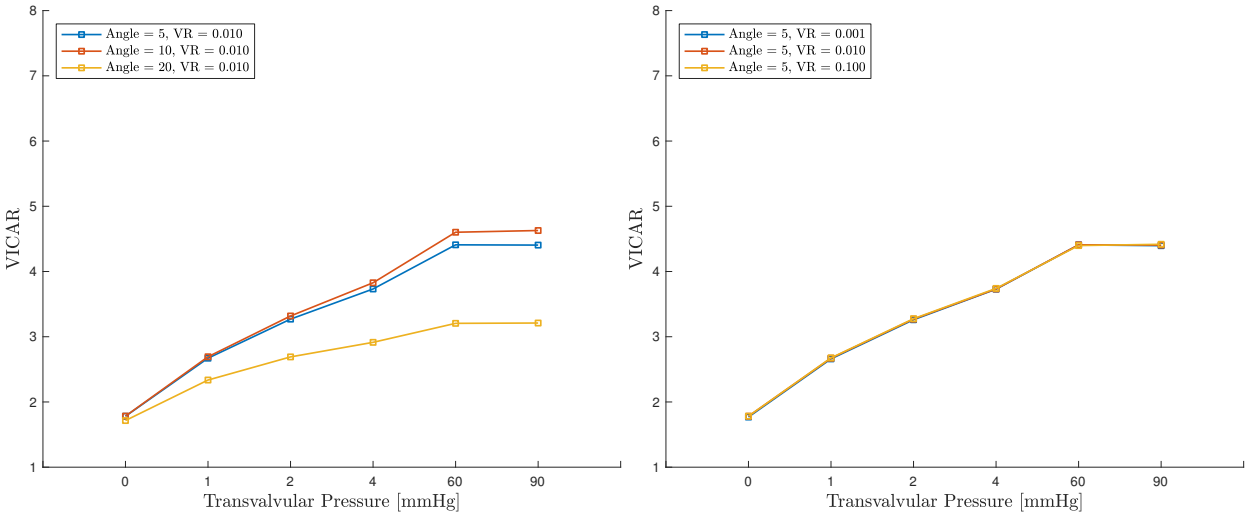

(a) Volume ratio (VR) fixed, varying angle.

(b) Angle (σ_θ) fixed, varying volume ratio.

Figure 3.11: Effect of VIC orientation and size on "apparent" aspect ratio. We note only a *significant* difference for 60/90 mmHg with the standard deviation of angle of the VIC.

we observe in Fig. 3.10.

RVE

At the heart of our model is the RVE. We first discuss several important assumptions we have made. Miehe *et al* [116] argue that due to the averaging process in homogenization, the details of the RVE do not greatly impact the macroscale problem, something we also observe. To facilitate computational efficiency, we downsample the RVE mesh and use an auxiliary high-fidelity mesh to extract details in a post-processing step (Fig. 3.5)

Again, for efficiency purposes we assume Taylor boundary conditions, which results in an overestimation of stiffness response [102]. We use the rather inaccurate boundary conditions because we are not interested in accuracy of the model, but rather, consistency. Naturally, we also use Taylor boundary conditions in the VICAR post-processing.

Fig 3.14 illustrates the difference in VICAR with Taylor and Dirichlet boundary conditions. As expected, the Dirichlet VICAR is on average lower. This is a result of only imposing motions on the boundaries, allowing for a relaxation of the VIC. Note that although the difference is large of the "apparent" VICAR, the actual VICAR does not differ by much.

Finally, we assume the VIC bonds perfectly with the ECM, which is not a physiologically realistic assumption (see Sec. 1.1). Modeling the discrete attachments via focal adhesions of the VIC requires special attention and is left as a limitation of the study.

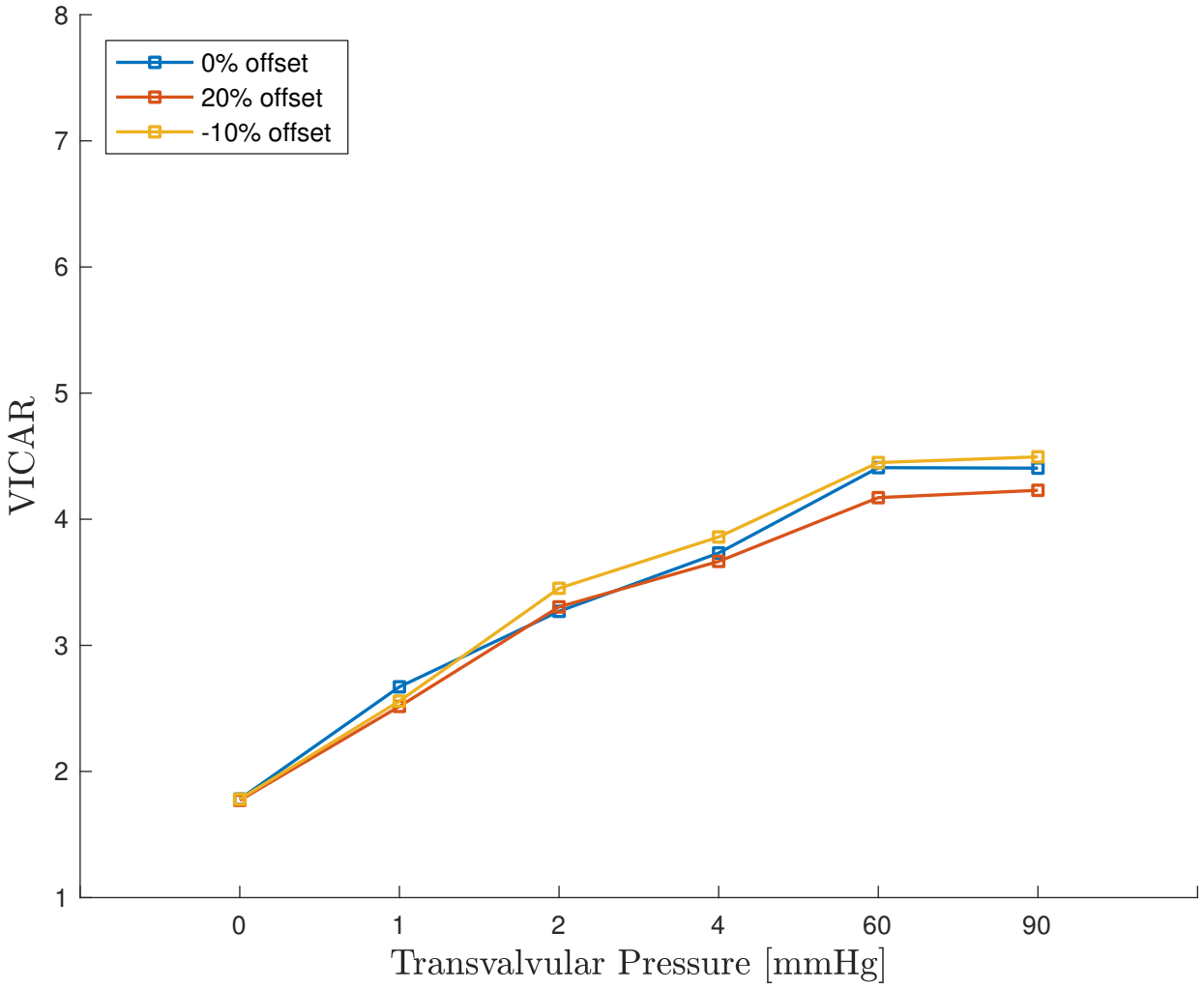

Figure 3.12: The effect of the initial cusp curvature on the VICAR. "Offset" y_0 viz. (3.8) is reported as a fraction of the size parameter r (e.g., an offset of 10% $\implies y_0 = 0.1r$). *Significant* but small differences are observed throughout.

VICAR

The aspect ratio being measured in the experiments is that of the nucleus, not the cell. We do not make a distinction between the nucleus and the cell in this analysis, i.e., we neglect the cytoskeleton. This is in line with previous analyses [80, 172]. We acknowledge that a more detailed model should incorporate this distinction, and we leave this to a future study.

The most notable result above is the large discrepancy between actual and "apparent" VICAR, as seen in Fig. 3.10. We observe that the (arithmetic) mean "apparent" response is more consistent with the experimental results. We note that there is also large variation in the "apparent" ratio.

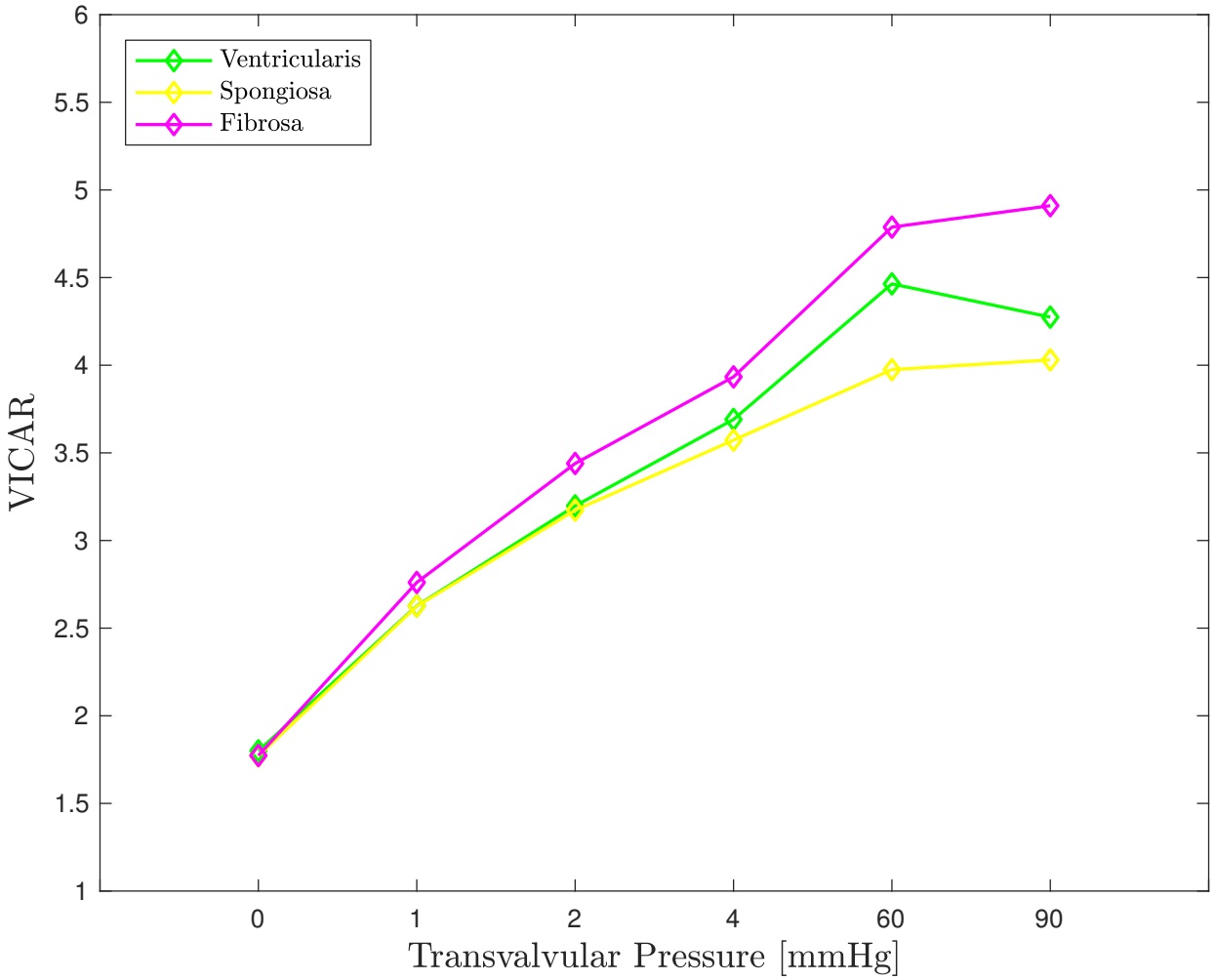

Figure 3.13: VICAR as measured in each of the three layers. *significant* differences are observed everywhere except low pressures between the spongiosa and ventricularis.

The procedure used to determine the "apparent" value, as depicted in Fig. 3.6, is representative of the experiments but naturally not exactly identical. They stand to show that the observed cellular deformation *may* be significantly different than the true deformation. This is of great importance when developing mechanotransduction models calibrated from experiments.

Figs 3.10, 3.11 and 3.12 show that the "apparent" response is not highly sensitive to the RVE (or macroscale) configuration, and that the largest source of discrepancy between the apparent and actual response comes from the "perspective" used to measure (i.e., the projection of the ellipsoid on the cutting plane). Thus, the orientation of the cutting plane has the greatest impact.

In Fig. 3.11 we observe "apparent" VICAR closer to the actual VICAR for $\sigma_\theta = 20°$.

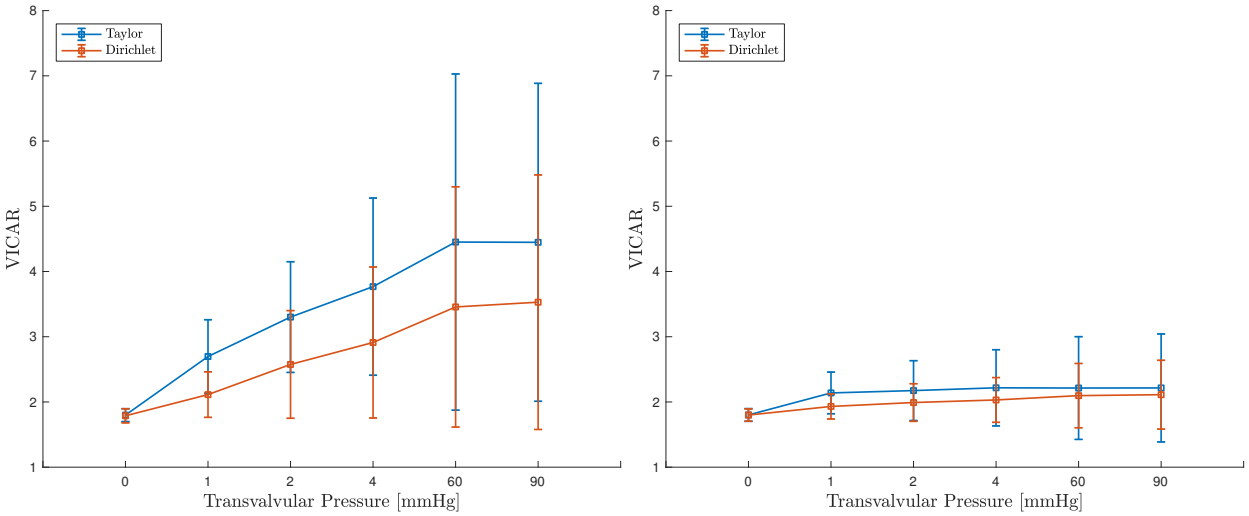

(a) "Apparent" VICAR. (b) Actual VICAR.

Figure 3.14: Effect of RVE boundary conditions on VICAR response. Taylor boundary conditions impose motion everywhere in the domain and Dirichlet boundary conditions only impose motion on the boundary.

However, the true distribution of the cell orientation is closer to $\sigma_\theta \leq 10°$, due to the consistency of the "apparent" VICAR with the experiments. We can interpret the larger spread as more control over the cutting plane orientation (i.e. the "perspective") to argue our previous claim regarding the largest source of discrepancy between the "apparent" and actual VICAR.

Finally, Fig. 3.13 shows that the greatest deformation in the tissue occurs in the fibrosa, consistent with previous findings [80, 172]. Indeed, the prevalence of calcification in the top layer of the fibrosa, a process driven by circumferential strain in the VIC, is consistent with this (see Chapter 4).

Computational considerations

As we mentioned, one full day of computation on 60 nodes of a compute cluster are required for a quasi-static analysis with simplified RVE boundary conditions. This is representative of only one small part of the cardiac cycle. Indeed, more relevant cyclic dynamic problems with more suitable RVE boundary conditions can prove to be challenging. This emphasizes the strict need for efficient implementation of FE^2. Nevertheless, the method is computationally tractable, and the abundant availability of large computing resources, as of the time of this study, render this issue an inconvenience.

3.5 Conclusion

We have demonstrated the feasibility of using computational homogenization, or FE^2, for modeling the multiscale behavior of aortic valve tissue. The method is, however, computationally expensive and required a large number of computing resources to run small static simulations in a reasonabe amount of time. Indeed, modeling full aortic valve geometry with dynamics and even fluids remains a daunting task.

As we argued in Chapter 1, multiscale modeling is necessary for understanding AV behavior and the method we have presented provides the first feasible way of achieving a fully coupled multiscale analysis for aortic valves. Furthermore, the RVEs can be used to develop cellular driven models. In the sequel, we will take a look at modeling calcification driven at the cellular scale.

Chapter 4

Multiscale Analysis of Calcified Tissue

The ultimate goal of aortic valve biomechanical models is to ameliorate, and prevent, disease. As discussed in Chapter 1, aortic valve disease is regulated by processes occurring at the cellular scale, hence the motivation for developing the multiscale model in Chapter 3. We developed an approach for simultaneously capturing organ-scale and cellular-scale biomechanics that is computationally tractable.

In this chapter, we will extend our multiscale model to study aortic valve disease. We consider the most prevalent of disease: calcification. The aim here is to understand relationship between the valvular interstitial cell aspect ratios, a metric established for characterizing cellular mechanotransduction, and calcification.

4.1 Aortic valve tissue calcification

We will begin by expanding on some of the concepts introduced in Sec. 1.2. As previously discussed, calcified aortic stenosis (CAS) is the most prevalent AV disease, affecting about 25% of adults over 65 years of age [148]. It is characterized by a failure of the valve leaflets to fully open due to the formation of calcified lesions similar to bone tissue [120].

The calcification process is hypothesized to begin with differentiation of VIC phenotype into osteoblast-like cells that alter the structure of the ECM [132]. The calcified legions begin as nodules that grow into non-random patterns [173]. A few common patterns were identified, with the two most common being“arc” and “partial arc” patterns (Fig 4.1) [161, 70]. Halevi et al [70]. used reverse CT to classify these patterns and how they progressed temporally and spatially. The calcification occurs more frequently on the aortic side of the valve (fibrosa) and the stiffening results in altered valve function [127, 174, 182, 58].

The underlying cause of calcification is still under investigation, but tissue strain and hemodynamic shear stresses have been identified as the main biomechanical factors driving their growth [10, 19, 35, 53, 181]. These factors result in a biochemical signaling processes between the endothelial cells and the VICs, promoting VIC differentiation into a calcific phenotype [51].

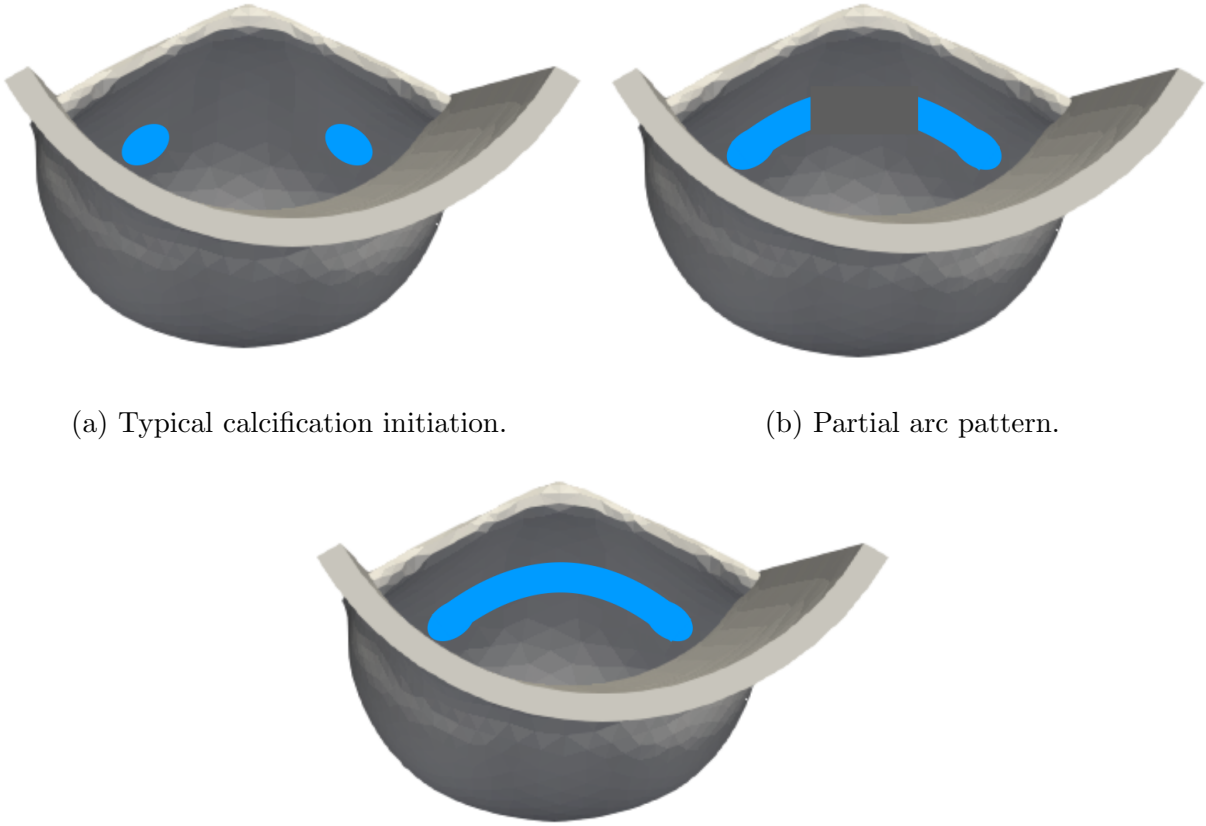

(a) Typical calcification initiation.

(b) Partial arc pattern.

(c) Mature arc pattern.

Figure 4.1: Prevalent calcification patterns on the aortic valve. Note calcification is typically found on the aortic side of the leaflet as shown in blue [161, 70]..

4.2 Multiscale modeling

We make use of the same model specified in Sec. 3.2 with the exception of pre-defined calcified elements. These elements follow the patterns depicted in Fig. 4.1 and the macro scale meshes are shown in Fig. 4.2. Only the topmost layer of elements in the fibrosa are calcified. The calcification-free RVEs are exactly as in Sec. 3.2, with parameters as given in Table 3.2. The material for the calcified RVEs is identical to the fibrosa but with $\mu = 1$ GPa, based on fully-developed bone tissue [135]. Furthermore, the bulk parameter K was scaled to 22 GPa to improve conditioning and guarantee convergence of the nonlinear equation solving.

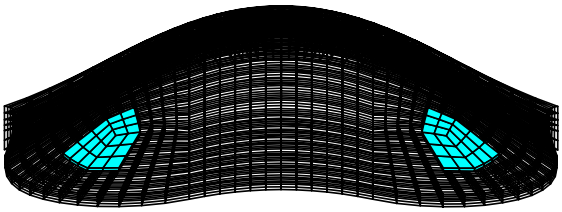

(a) Early-stage calcified nodules.

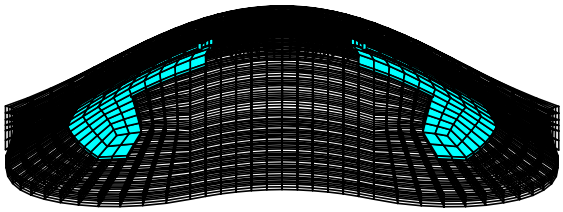

(b) Partial arc pattern.

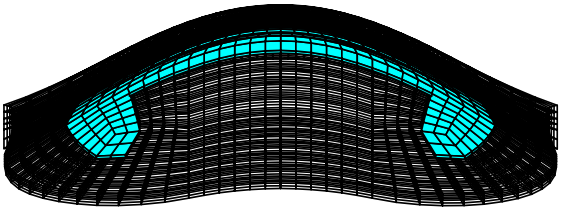

(c) Mature "arc" pattern.

Figure 4.2: Macro-scale leaflet meshes with calcified regions highlighted.

4.3 Results

Early-stage nodules

Fig. 4.3 shows the deformed shape at the five steps of the loading protocol outlined in Table 3.1, similar to Fig 3.9 but with calcified nodules present. We maintain quasi-incompressible behavior as in the calcification-free model. The strain plotted is in a Cartesian system and a mapping to the CRT coordinates (via (3.8) is required to recover circumferential strain. Note the kinking of deformation in the belly region at high pressures.

VICAR

In Fig. 4.4 we see the VIC aspect ratio (VICAR) measured as in Fig. 3.10 with the presence of calcified nodules (Fig. 4.2a). Note that the calculation excludes VICs in the calcified regions. The "apparent" VICAR (Fig. 4.4a) in the belly region of the leaflet is slightly smaller than the healthy case (*significant* only at 60 and 90 mmHg). The actual VICAR is, however, *higher* (*significant*) than the healthy case (Fig. 4.4b).

Partial arc pattern

Fig. 4.5 shows the deformed shape at the five steps of the loading protocol outlined in Table 3.1, similar to Fig 3.9 but with a partial arc calcification pattern. We maintain quasi-incompressible behavior as in the calcification-free model.

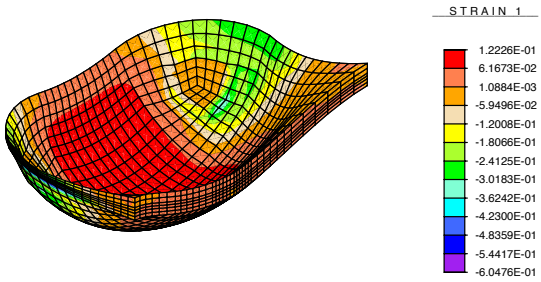

(a) 1 mmHg.

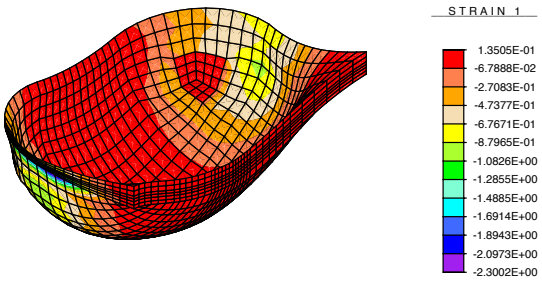

(b) 2 mmHg.

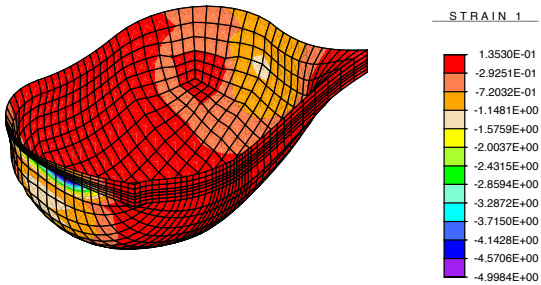

(c) 4 mmHg.

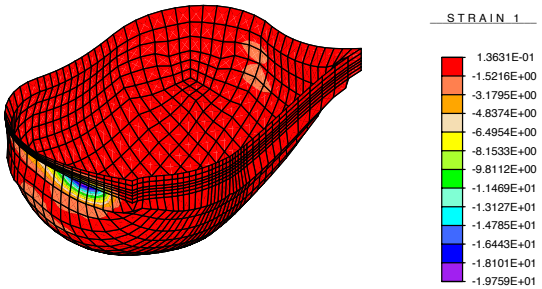

(d) 60 mmHg.

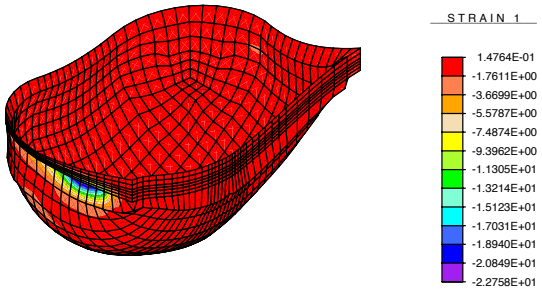

(e) 90 mmHg.

Figure 4.3: Leaflet deformation under load defined in Table 3.1 with nodule pattern.The strain plotted is in a Cartesian system and not the circumferential strain.

VICAR

In Fig. 4.6 we see the VIC aspect ratio (VICAR) measured as in Fig. 3.10 with the presence of calcified nodules (Fig. 4.2b). Note that the calculation excludes VICs in the calcified regions.

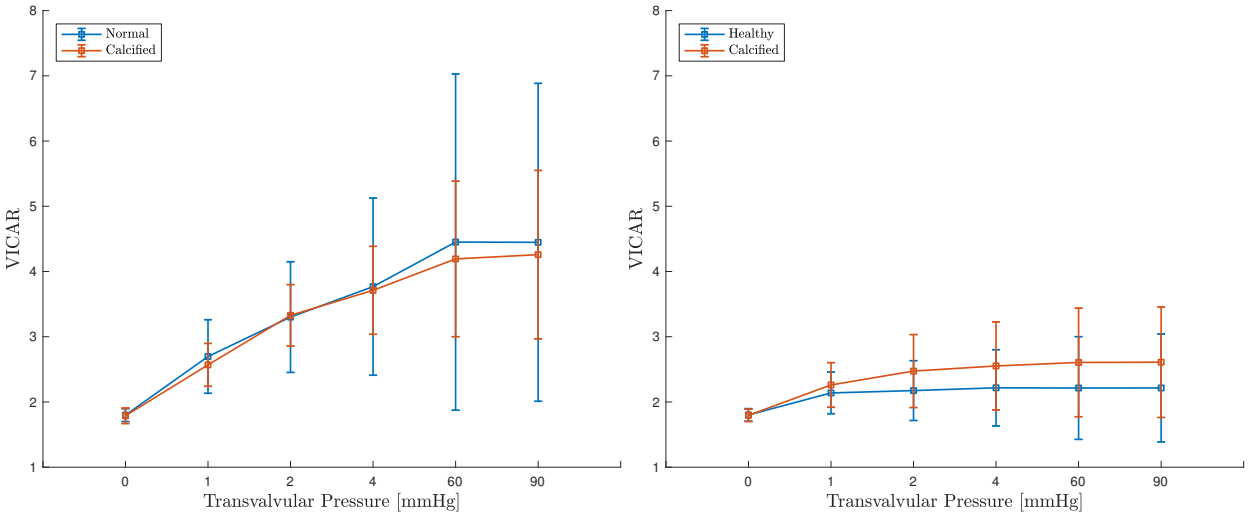

(a) "Apparent" VICAR. (b) Actual VICAR.

Figure 4.4: VICAR for early stage calcified nodules.

The "apparent" VICAR (Fig. 4.6a) along the belly is slightly smaller than the healthy case (*significant* only at 60/90 mmHg). The actual VICAR is, however, *higher* (*significant*) than the healthy case (Fig. 4.6b).

Mature arc pattern

Fig. 4.7 shows the deformed shape at the five steps of the loading protocol outlined in Table 3.1, similar to Fig 3.9 but with a mature arc pattern. We maintain quasi-incompressible behavior as in the calcification-free model.

VICAR

In Fig. 4.8 we see the VICAR measured as in Fig. 3.10 with the presence of a mature calcified arc pattern (Fig. 4.2c). The "apparent" VICAR (Fig. 4.8a) along the belly is noticeably smaller than the healthy case (*significant*). The actual VICAR is, unlike the nodules, slightly lower (*significant*) than the healthy case (Fig. 4.8b).

4.4 Discussion

Early-stage nodules

Although not clear from Fig. 4.3, the average Almansi circumferential, strain in the belly region of the calcified leaflet is on average $\sim 20\%$ larger than the healthy leaflet (Table 4.1). Conversely, the radial strain is on average $\sim 17\%$ of the healthy model.

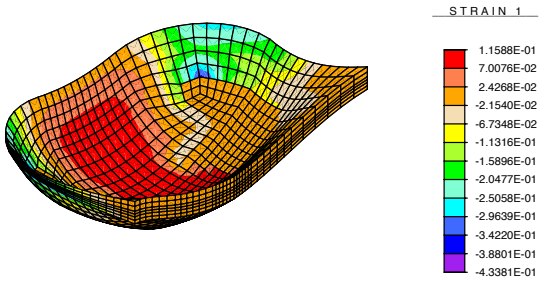

(a) 1 mmHg.

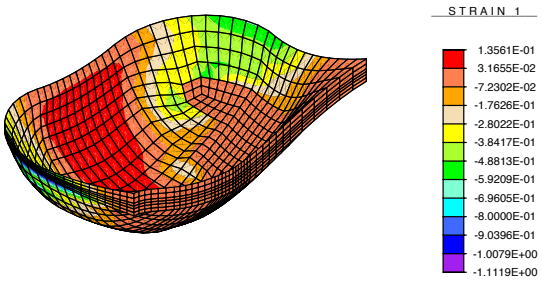

(b) 2 mmHg.

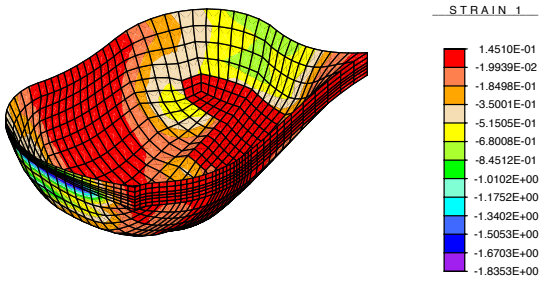

(c) 4 mmHg.

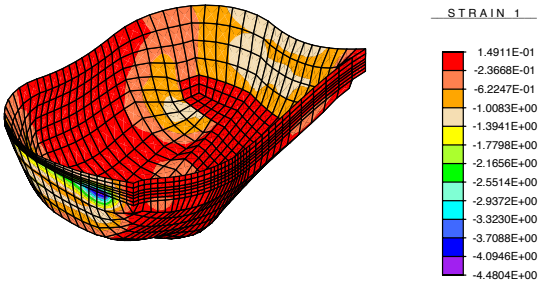

(d) 60 mmHg.

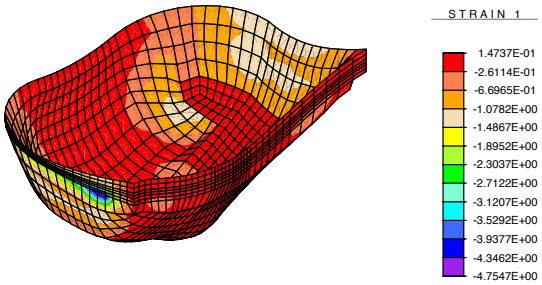

(e) 90 mmHg.

Figure 4.5: Leaflet deformation under loading defined in Table 3.1 with partial arc pattern. Note the calcified regions on the surface. The strain plotted is in a Cartesian system and not the circumferential strain.

Taking a closer look at the microscale response of the VICs in Fig 4.4b, we note that indeed the average VIC experiences a larger (*significant*) aspect ratio than the healthy case.

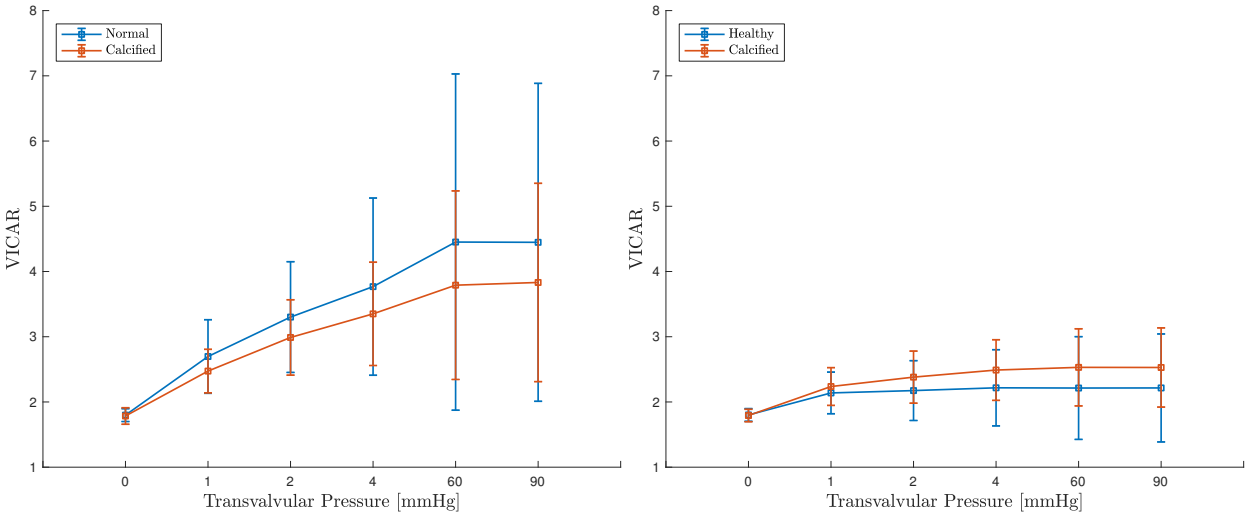

(a) "Apparent" VICAR. (b) Actual VICAR.

Figure 4.6: VICAR for partial arc pattern.

Load [mmHg]	1 mmHg	2 mmHg	4 mmHg	60 mmHg	90 mmHg
Circumf Strain Ratio	0.96	1.19	1.32	1.26	1.21
Radial Strain Ratio	-0.39	0.14	0.31	0.42	0.41

Table 4.1: Average ratio of calcific nodule leaflet to healthy circumferential Almansi strain in belly region.

Interestingly, we observe little difference in the "apparent" VICAR in Fig 4.4a. In fact, we only see a slight (*significant*) *decrease* in the VICAR at 60 mmHg.

Note the increased circumferential strain (VICAR) due to the presence of calcified nodules. Previous studies indicate that the increased circumferential strain results in calcification growth [3, 70]. Thus, one would expect the nodules would grow into more mature patterns with the increased circumferential strain.

Partial arc pattern

The partial arc serves as both a different "mature" pattern example, and as a midway stage between the nodule and the full arc. We see a disturbed deformed state via the kink in the belly region, where there is a large discontinuity in stiffness from the calcified region (Fig. 4.5). Indeed, calcified valves exhibit abnormal (and inefficient) dynamics, such as in stenosis or regurgitation. Furthermore, the larger VICAR indicates further progression of the calcification.

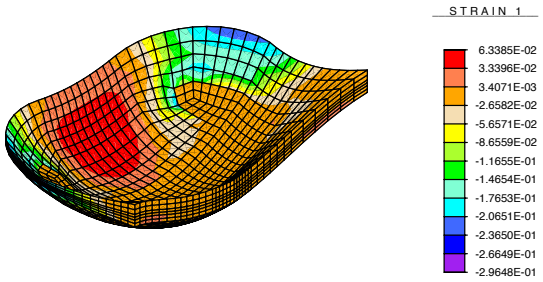

(a) 1 mmHg.

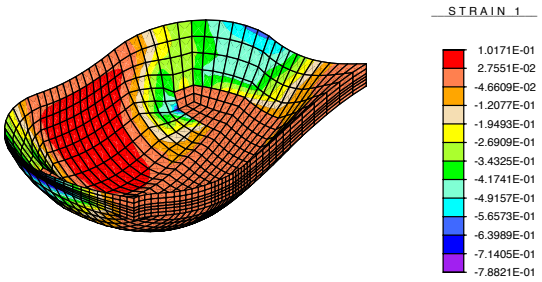

(b) 2 mmHg.

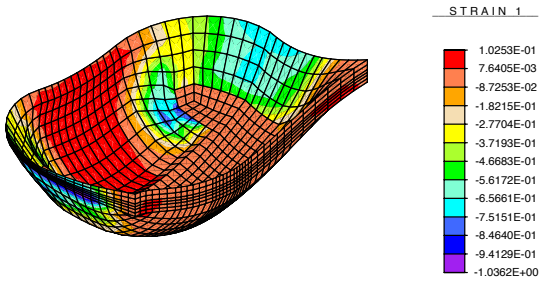

(c) 4 mmHg.

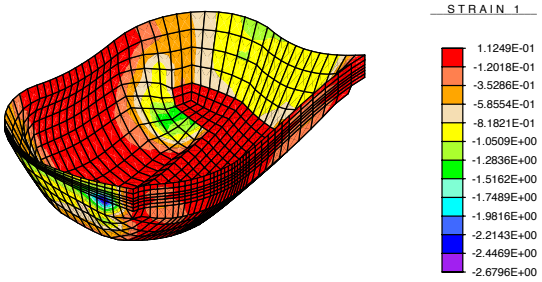

(d) 60 mmHg.

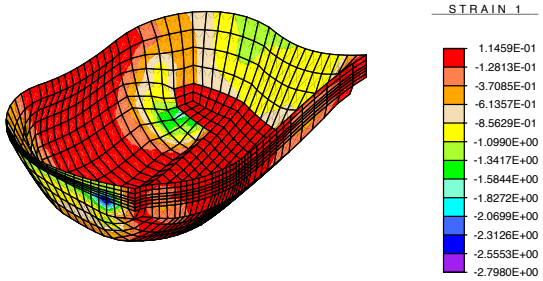

(e) 90 mmHg.

Figure 4.7: Leaflet deformation under load defined in Table 3.1 with arc pattern. Note the calcified regions on the surface. The strain plotted is in a Cartesian system and not the circumferential strain.

Mature arc pattern

It is clear from Fig. 4.7 that the calcified leaflet experiences significantly lower strain. In fact, we see an average $\sim 43\%$ reduction in the circumferential strain, and an inversion of the

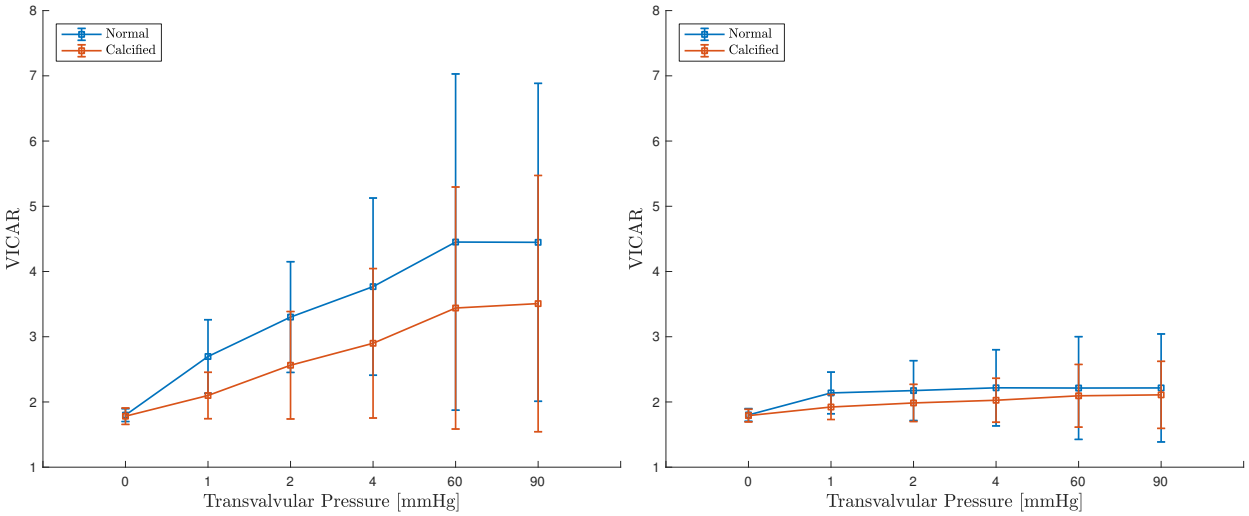

(a) "Apparent" VICAR. (b) Actual VICAR.

Figure 4.8: VICAR for arc along edge.

radial strain for low (<60mmHg) pressures. One can argue that the decreased circumferential pattern limits the development of further calcification, resulting in a natural "saturation" of the calcification.

Taking a closer look at the microscale response of the VICs in Fig 4.8 we note that indeed the average VIC experiences a decreased aspect ratio (i.e., relative to the VIC ellipsoid principal axes), for both the "apparent" (*significant*) and actual (*significant* for 1-4 mmHg) calculations.

4.5 Conclusion

In this chapter we utilized the multiscale AV leaflet model developed in the prequel to study three calcification topologies: early-stage nodules, a partial arc and a mature arc pattern. In the former, we saw the presence of the nodules led to a larger circumferential strain and VIC aspect ratio that presumably drives further calcification growth in a positive-feedback loop manner. Furthermore, we noticed that the "apparent" aspect ratio, as measured by slicing a section of the tissue and observing the 2D aspect ratio of the cell cross-section, did not necessarily exhibit the true aspect ratio.

In the latter cases, we observed disturbed biomechanics of the leaflet that presumably results in stenoic behavior. The lower aspect ratio is consistent with a natural "saturation" of the calcification typical of mature calcified valves.

Limitations

We wrap up the study with a brief discussion on the main limitations of our approach. First, our model follows the experiments of Huang [79] by using a static loading with fixed boundary conditions around the leaflet. Ideally, a followup study should be performed with dynamic and cyclic loading using appropriate boundary conditions of the *in vivo* AV leaflet.

Second, the stochastic nature of the patterns was not captured by three predefined and symmetric patterns. Further elaboration is required to look at slight variations of the patterns with asymmetry. We note that our main goal was to take a look at the overall behavior uncovered in Chapter 3 with calcifications present rather than study the behavior and evolution of the calcification.

Chapter 5

Closure

Summary and conclusions

Aortic valve disease is a public health concern with few and limited treatment options. Over the last few decades, researchers have applied the tools of biomechanical analysis and computational modeling in an effort to understand the elusive nature of aortic valve function, in health and disease. Despite much progress, traditional single-scale modeling approaches have not provided answers to some of the most important questions.

Recent findings in the laboratory have uncovered the significance of valvular interstitial cells in healthy and diseased aortic valves. These findings underscore the importance of not only modeling the cellular scale, but coupling it to the well-studied organ-scale biomechanics. In the preceding work, we developed a fully coupled multiscale model of aortic valve tissue that simultaneously combines organ-scale and cellular-scale biomechanics in a computationally tractable manner.

In Chapter 2 we presented the continuum mechanics framework and a method to consistently model aortic valve tissue. We demonstrated the significance of modeling the normal distribution of fibers in the microstructure (in corroboration of the findings of Billiar and Sacks [16]). We further demonstrated the need for appropriate prestressing of the AV composite to achieve consistent trilayer mechanical behavior.

As we argued in Chapter 1, multiscale modeling is necessary for understanding AV behavior. In Chapter 3 we demonstrated the feasibility of using computational homogenization, or FE^2, for modeling the multiscale behavior of aortic valve tissue. The method provides the first feasible way of achieving a fully coupled multiscale analysis for aortic valves. We focused on the cellular aspect ratio as a metric for mechanotransduction and noticed that the "apparent" aspect ratio, as measured experimentally by slicing a section of the tissue and observing the 2D aspect ratio of the cell cross-section, did not necessarily exhibit the true aspect ratio.

Finally, in Chapter 4 we utilized the multiscale model to study three calcification topologies: early-stage nodules, a partial arc and a mature arc pattern. In the former, we saw the presence of the nodules led to a larger circumferential strain and VIC aspect ratio that

presumably drives further calcification growth in a positive-feedback loop manner. In the latter cases, we observed disturbed biomechanics of the leaflet that presumably results in stenoic behavior. The lower aspect ratio is consistent with a natural "saturation" of the calcification typical of mature calcified valves.

Limitations

Our goal here was to introduce (and validate) a multiscale model of aortic valve tissue. We highlight several simplifications we made along the way:

1. *Geometry*: We used a greatly simplified geometry that also did not account for the aortic root and sinus.
2. *Boundary condition*: We used boundary conditions in Chapters 3 and 4 that were consistent with *in vitro* experiments but not necessarily representative of the *in vivo* aortic valve.
3. *Prestressing*: The prestressing introduced in Chapter 2 was left out of the following chapters.
4. *Physic*: We only looked at static loading of the valve. To better model physiological *in vivo* conditions, we need to include dynamics and fluid-structure interaction.
5. *Cell*: Our model of the cell was rather simple and used simple RVE boundary conditions.
6. *Computation*: Although computationally tractable, the approach is still computationally expensive and requires significant computing resources.

Future work

By addressing the simplifications just described, we define several next steps for study. In addition, the following problems are of great interest and challenge.

Patient-specific geometries

Idealized geometry is just that: ideal. More realistic geometries of actual diseased valves derived through medical imagery, can provide more useful insight on the function of the diseased valve. Moreover, such models can be used to study treatment options.

Calcification growth models

Calcification growth models *a la* Arzani and Mofrad [3] and Halevi *et al* [70]. have proven a useful tool for understanding disease progression. Simple strain-based rules are a first step, but more sophisticated chemical models are more interesting, particularly when driven at the cellular scale (see below).

Sophisticated RVE models

The motivation for multiscale models is to understand how the valvular interstitial cells interact with valve function. Computational modeling allows us to simulate *in vivo* behavior where we can "observe" VIC function. To obtain interesting results, more sophisticated mechanotransduction models are needed at the RVE. Examples include focal adhesions, mechanochemical driven calcification growth, extracellular matrix remodeling, and poroelasticity.

Fluid-structure interaction

The significance of the hemodynamics in valve function and disease demands incorporating a (non-Newtonian) fluid interacting with the tissue, *a la* Weinberg and Mofrad [172]. Furthermore, an extension of the computational homogenization technique to the *fluid* can provide some novel insights.

Bibliography

[1] J Ahrens et al. "Paraview: An End-user Tool for Large-data Visualization". In: *The Visualization Handbook* (2005), p. 717.

[2] G Argento et al. "Multi-scale Mechanical Characterization of Scaffolds for Heart Valve Tissue Engineering". In: *Journal of Biomechanics* 45.16 (2012), pp. 2893–2898.

[3] A Arzani and M Mofrad. "A Strain-based Finite Element Model for Calcification Progression In Aortic Valves". In: *Journal of Biomechanics* 65 (2017), pp. 216–220.

[4] S Atkins et al. "Bicuspid Aortic Valve Hemodynamics Induces Abnormal Medial Remodeling In the Convexity of Porcine Ascending Aortas". In: *Biomechanics and Modeling In Mechanobiology* 13.6 (2014), pp. 1209–1225.

[5] F Auricchio et al. "A Computational Tool To Support Pre-operative Planning of Stentless Aortic Valve Implant". In: *Medical Engineering and Physics* 33.10 (2011), pp. 1183–1192.

[6] F Auricchio et al. "Patient-specific Simulation of a Stentless Aortic Valve Implant: the Impact of Fibres on Leaflet Performance." In: *Comput. Methods Biomech. Biomed. Engin.* 17.3 (2014), pp. 277–85.

[7] F Auricchio et al. "Simulation of Transcatheter Aortic Valve Implantation: a Patient-specific Finite Element Approach." In: *Comput. Methods Biomech. Biomed. Engin.* 17.12 (2014), pp. 1347–57.

[8] D Bach. "Prevalence and Characteristics of Unoperated Patients With Severe Aortic Stenosis." In: *The Journal of Heart Valve Disease* 20.3 (2011), pp. 284–291.

[9] A Bakhaty and M Mofrad. "Coupled Simulation of Heart Valves: Applications To Clinical Practice". In: *Annals of Biomedical Engineering* 43.7 (2015), pp. 1626–1639.

[10] K Balachandran et al. "Elevated Cyclic Stretch Alters Matrix Remodeling In Aortic Valve Cusps: Implications for Degenerative Aortic Valve Disease". In: *American Journal of Physiology-heart and Circulatory Physiology* 296.3 (2009), H756–H764.

[11] A Balguid et al. "Stress Related Collagen Ultrastructure In Human Aortic Valves - Implications for Tissue Engineering". In: *Journal of Biomechanics* 41.12 (2008), pp. 2612–2617.

[12] J Ball. "Convexity Conditions and Existence Theorems In Nonlinear Elasticity". In: *Archive for Rational Mechanics and Analysis* 63.4 (1976), pp. 337–403.

[13] D Balzani et al. "A Polyconvex Framework for Soft Biological Tissues. Adjustment To Experimental Data". In: *International Journal of Solids and Structures* 43.20 (2006), pp. 6052–6070.

[14] A Barker and M Markl. *The Role of Hemodynamics In Bicuspid Aortic Valve Disease.* 2011.

[15] V Barocas and R Tranquillo. "An Anisotropic Biphasic Theory of Tissue-equivalent Mechanics: the Interplay Among Cell Traction, Fibrillar Network Deformation, Fibril Alignment, and Cell Contact Guidance". In: *Journal of Biomechanical Engineering* 119.2 (1997), pp. 137–145.

[16] K Billiar and M Sacks. "Biaxial Mechanical Properties of the Natural and Glutaraldehyde Treated Aortic Valve Cusp – Part I: Experimental Results". In: *Journal of Biomechanical Engineering* 122.1 (2000), pp. 23–30.

[17] P Blaha et al. "Full-potential, Linearized Augmented Plane Wave Programs for Crystalline Systems". In: *Computer Physics Communications* 59.2 (1990), pp. 399–415.

[18] R Bonow et al. "2008 Focused Update Incorporated Into the Acc/aha 2006 Guidelines for the Management of Patients With Valvular Heart Disease". In: *Circulation* 118.15 (2008), e523–e661.

[19] R Bouchareb et al. "Mechanical Strain Induces the Production of Spheroid Mineralized Microparticles In the Aortic Valve Through a Rhoa/rock-dependent Mechanism". In: *Journal of Molecular and Cellular Cardiology* 67 (2014), pp. 49–59.

[20] N Boudreau and P Jones. "Extracellular Matrix and Integrin Signalling: The Shape of Things To Come". In: *Biochemical Journal* 339.3 (1999), pp. 481–488.

[21] R Buchanan and M Sacks. "Interlayer Micromechanics of the Aortic Heart Valve Leaflet". In: *Biomechanics and Modeling In Mechanobiology* 13.4 (2014), pp. 813–826.

[22] G Cacciola et al. "Development and Testing of a Synthetic Fiber Reinforced Three-leaflet Heart Valve". In: *EUROMAT 97: 5th European Conference on Advanced Materials and Processes and Applications.* Vol. 3. 1997, pp. 547–550.

[23] A Cataloglu, P Gould, and R Clark. "Validation of a Simplified Mathematical Model for the Stress Analysis of Human Aortic Heart Valves". In: *Journal of Biomechanics* 8.5 (1975), pp. 347–348.

[24] K Chan et al. "A Multiscale Modeling Approach To Scaffold Design and Property Prediction". In: *Journal of the Mechanical Behavior of Biomedical Materials* 3.8 (2010), pp. 584–593.

[25] P Chandran and V Barocas. "Affine Versus Non-affine Fibril Kinematics in Collagen Networks: Theoretical Studies of Network Behavior". In: *Journal of Biomechanical Engineering* 128.2 (2006), pp. 259–270.

[26] A Chester, M Misfeld, and M Yacoub. "Receptor-mediated Contraction of Aortic Valve Leaflets." In: *The Journal of Heart Valve Disease* 9.2 (2000), pp. 250–4.

[27] G Christie and B Barratt-Boyes. "Biaxial Mechanical Properties of Explanted Aortic Allograft Leaflets". In: *The Annals of Thoracic Surgery* 60 (1995), S160–S164.

[28] G Christie and R Stephenson. "Modelling the Mechanical Role of the Fibrosa and Ventricularis In the Porcine Bioprosthesis". In: *International Symposium on Surgery for Heart Valve Disease*. 1989, pp. 815–824.

[29] R Cloots et al. "Multi-scale Mechanics of Traumatic Brain Injury: Predicting Axonal Strains From Head Loads". In: *Biomechanics and Modeling In Mechanobiology* 12.1 (2013), pp. 137–150.

[30] C Conti et al. "Biomechanical Implications of the Congenital Bicuspid Aortic Valve: a Finite Element Study of Aortic Root Function From In Vivo Data". In: *The Journal of Thoracic and Cardiovascular Surgery* 140.4 (2010), pp. 890–896.

[31] A Cribier et al. "Percutaneous Transcatheter Implantation of An Aortic Valve Prosthesis for Calcific Aortic Stenosis: First Human Case Description". In: *Circulation* 106.24 (2002), pp. 3006–3008.

[32] L Croft and M Mofrad. *Computational Modeling In Biomechanics*. Ed. by Suvranu De, Farshid Guilak, and Mohammad Mofrad R. K. Dordrecht: Springer Netherlands, 2010.

[33] B Dacorogna. *Direct Methods In the Calculus of Variations*. New York, NY: Springer Science & Business Media, 2007.

[34] L Dasi et al. "Fluid Mechanics of Artificial Heart Valves". In: *Clinical and Experimental Pharmacology and Physiology* 36.2 (2009), pp. 225–237.

[35] W David Merryman. "Mechano-potential Etiologies of Aortic Valve Disease." In: *Journal of Biomechanics* 43.1 (Jan. 2010), pp. 87–92.

[36] T David and C Feindel. "An Aortic Valve-sparing Operation for Patients With Aortic Incompetence and Aneurysm of the Ascending Aorta." In: *The Journal of Thoracic and Cardiovascular Surgery* 103.4 (1992), pp. 617–21.

[37] C Doumanidis. "Nanomanufacturing of Random Branching Material Architectures". In: *Microelectronic Engineering* 86.4-6 (2009), pp. 467–478.

[38] N Driessen, C Bouten, and F Baaijens. "Improved Prediction of the Collagen Fiber Architecture In the Aortic Heart Valve". In: *Journal of Biomechanical Engineering* 127.2 (2005), pp. 329–336.

[39] N Driessen et al. "Computational Analyses of Mechanically Induced Collagen Fiber Remodeling In the Aortic Heart Valve". In: *Journal of Biomechanical Engineering* 125.4 (2003), pp. 549–557.

[40] N Driessen et al. "Modeling the Mechanics of Tissue-engineered Human Heart Valve Leaflets". In: *Journal of Biomechanics* 40.2 (2007), pp. 325–334.

[41] N Driessen et al. "Remodelling of the Angular Collagen Fiber Distribution In Cardiovascular Tissues". In: *Biomechanics and Modeling In Mechanobiology* 7.2 (2008), p. 93.

[42] K Dumont et al. "Validation of a Fluid–structure Interaction Model of a Heart Valve Using the Dynamic Mesh Method In Fluent". In: *Computer Methods In Biomechanics and Biomedical Engineering* 7.3 (2004), pp. 139–146.

[43] B Efron. "Computers and the Theory of Statistics: Thinking the Unthinkable". In: *Siam Review* 21.4 (1979), pp. 460–480.

[44] G Engelmayr Jr et al. "A Novel Bioreactor for the Dynamic Flexural Stimulation of Tissue Engineered Heart Valve Biomaterials". In: *Biomaterials* 24.14 (2003), pp. 2523–2532.

[45] G Engelmayr et al. "A Novel Flex-stretch-flow Bioreactor for the Study of Engineered Heart Valve Tissue Mechanobiology". In: *Annals of Biomedical Engineering* 36.5 (2008), pp. 700–712.

[46] R Fan et al. "Optimal Elastomeric Scaffold Leaflet Shape for Pulmonary Heart Valve Leaflet Replacement". In: *Journal of Biomechanics* 46.4 (2013), pp. 662–669.

[47] Q Fang and D Boas. *Iso2mesh: a 3d Surface and Volumetric Mesh Generator for Matlab/octave*. 2010.

[48] O Farokhzad and R Langer. "Impact of Nanotechnology on Drug Delivery". In: *ACS Nano* 3.1 (2009), pp. 16–20.

[49] P Fedak et al. "Clinical and Pathophysiological Implications of a Bicuspid Aortic Valve". In: *Circulation* 106.8 (2002), pp. 900–904.

[50] D Filip, A Radu, and M Simionescu. "Interstitial Cells of the Heart Valves Possess Characteristics Similar To Smooth Muscle Cells." In: *Circulation Research* 59.3 (1986), pp. 310–320.

[51] C Fisher, J Chen, and W Merryman. "Calcific Nodule Morphogenesis By Heart Valve Interstitial Cells Is Strain Dependent". In: *Biomechanics and Modeling In Mechanobiology* 12.1 (2013), pp. 5–17.

[52] A Freed. "Anisotropy In Hypoelastic Soft-tissue Mechanics, I: Theory". In: *Journal of Mechanics of Materials and Structures* 3.5 (2008), pp. 911–928.

[53] R Freeman and C Otto. "Spectrum of Calcific Aortic Valve Disease: Pathogenesis, Disease Progression, and Treatment Strategies". In: *Circulation* 111.24 (2005), pp. 3316–3326.

[54] M Freutel et al. "Finite Element Modeling of Soft Tissues: Material Models, Tissue Interaction and Challenges". In: *Clinical Biomechanics* 29.4 (2014), pp. 363–372.

[55] J Friedrichs et al. "Cellular Remodelling of Individual Collagen Fibrils Visualized By Time-lapse Afm". In: *Journal of Molecular Biology* 372.3 (2007), pp. 594–607.

[56] Y Fung. "Biomechanical Aspects of Growth and Tissue Engineering". In: *Biomechanics: Motion, Flow, Stress, and Growth*. New York, NY: Springer New York, 1990, pp. 499–546.

[57] T Gasser, R Ogden, and G Holzapfel. "Hyperelastic Modelling of Arterial Layers With Distributed Collagen Fibre Orientations". In: *Journal of the Royal Society Interface* 3.6 (2006), pp. 15–35.

[58] L Ge and F Sotiropoulos. "Direction and Magnitude of Blood Flow Shear Stresses on the Leaflets of Aortic Valves: Is There a Link With Valve Calcification?" In: *Journal of Biomechanical Engineering* 132.1 (2010), p. 014505.

[59] S Gharacholou et al. "Aortic Valve Sclerosis and Clinical Outcomes: Moving Toward a Definition". In: *The American Journal of Medicine* 124.2 (2011), pp. 103–110.

[60] A Go. *Heart Disease and Stroke Statistics–2014 Update: a Report From the American Heart Association.* Vol. 129. 3. Jan. 2014, e28–e292.

[61] S Göktepe et al. "A Multiscale Model for Eccentric and Concentric Cardiac Growth Through Sarcomerogenesis". In: *Journal of Theoretical Biology* 265.3 (2010), pp. 433–442.

[62] K Grande et al. "Mechanisms of Aortic Valve Incompetence: Finite Element Modeling of Aortic Root Dilatation". In: *Annals of Thoracic Surgery* 69.6 (2000), pp. 1851–1857.

[63] K Grande et al. "Stress Variations In the Human Aortic Root and Valve: the Role of Anatomic Asymmetry". In: *Annals of Biomedical Engineering* 26.4 (1998), pp. 534–545.

[64] K Grande-Allen et al. "Re-creation of Sinuses Is Important for Sparing the Aortic Valve: a Finite Element Study". In: *Journal of Thoracic and Cardiovascular Surgery* 119.4 (2000), pp. 753–763.

[65] J Grashow et al. "Planar Biaxial Creep and Stress Relaxation of the Mitral Valve Anterior Leaflet". In: *Annals of Biomedical Engineering* 34.10 (2006), pp. 1509–1518.

[66] S Grbic et al. "Image-based Computational Models for Tavi Planning: From Ct Images To Implant Deployment". In: *International Conference on Medical Image Computing and Computer-Assisted Intervention*. Springer. 2013, pp. 395–402.

[67] G Grunkemeier. "Artificial Heart Valves". In: *Annual Review of Medicine* 41 (1990), pp. 251–263.

[68] N Gundiah, M Ratcliffe, and L Pruitt. "Determination of Strain Energy Function for Arterial Elastin: Experiments Using Histology and Mechanical Tests". In: *Journal of Biomechanics* 40.3 (2007), pp. 586–594.

[69] R Haj-Ali et al. "A General Three-dimensional Parametric Geometry of the Native Aortic Valve and Root for Biomechanical Modeling". In: *Journal of Biomechanics* 45.14 (2012), pp. 2392–2397.

[70] R Halevi et al. "Progressive Aortic Valve Calcification: Three-dimensional Visualization and Biomechanical Analysis". In: *Journal of Biomechanics* 48.3 (2015), pp. 489–497.

[71] H Henninger et al. "Validation of Computational Models In Biomechanics". In: *Proceedings of the Institution of Mechanical Engineers, Part H: Journal of Engineering In Medicine* 224.7 (2010), pp. 801–812.

[72] D Hepworth et al. "Affine Versus Non-affine Deformation In Soft Biological Tissues, Measured By the Reorientation and Stretching of Collagen Fibres Through the Thickness of Compressed Porcine Skin". In: *Journal of Biomechanics* 34.3 (2001), pp. 341–346.

[73] R Hinton and K Yutzey. "Heart Valve Structure and Function In Development and Disease". In: *Annual Review of Physiology* 73 (2011), pp. 29–46.

[74] B Hinz et al. "Recent Developments In Myofibroblast Biology: Paradigms for Connective Tissue Remodeling". In: *The American Journal of Pathology* 180.4 (2012), pp. 1340–1355.

[75] G Holzapfel. *Nonlinear Solid Mechanics*. Wiley Chichester, UK, 2000.

[76] G Holzapfel, T Gasser, and R Ogden. "A New Constitutive Framework for Arterial Wall Mechanics and a Comparative Study of Material Models". In: *Journal of Elasticity and the Physical Science of Solids* 61.1-3 (2000).

[77] G Holzapfel and R Ogden. "Constitutive Modelling of Arteries". In: *Proceedings of the Royal Society of London A: Mathematical, Physical and Engineering Sciences* 466.2118 (2010), pp. 1551–1597.

[78] G Holzapfel and R Ogden. "Constitutive Modelling of Passive Myocardium: A Structurally Based Framework for Material Characterization". In: *Philosophical Transactions of the Royal Society of London A: Mathematical, Physical and Engineering Sciences* 367.1902 (2009), pp. 3445–3475.

[79] H Huang. "Micromechanical Simulations of Heart Valve Tissues". PhD thesis. University of Pittsburgh, 2004.

[80] H Huang, J Liao, and M Sacks. "In-situ Deformation of the Aortic Valve Interstitial Cell Nucleus Under Diastolic Loading". In: *Journal of Biomechanical Engineering* 129 (2007), pp. 880–889.

[81] S Huang. "Virtualisation of Stress Distribution In Heart Valve Tissue." In: *Computational Methods In Biomechanics and Biomedical Engineering* 17.15 (Nov. 2014), pp. 1696–704. URL: http://www.ncbi.nlm.nih.gov/pubmed/23477432.

[82] S Huang and H Huang. "Virtual Experiments of Heart Valve Tissues." In: *Conference Proceedings of Ieee Engineering In Medical and Biolology Society* 2012 (Jan. 2012), pp. 6645–8.

[83] J Humphrey. *Cardiovascular Tissue Mechanics: Cells, Tissues, and Organs*. 2002.

[84] D Ingber. *Opposing Views on Tensegrity As a Structural Framework for Understanding Cell Mechanics-rebuttals*. 2000.

[85] Z Jahed et al. "Mechanotransduction Pathways Linking the Extracellular Matrix To the Nucleus". In: *International Review of Cell and Molecular Biology*. Vol. 310. Elsevier, 2014, pp. 171–220.

[86] P Jermihov et al. "Effect of Geometry on the Leaflet Stresses In Simulated Models of Congenital Bicuspid Aortic Valves". In: *Cardiovascular Engineering and Technology* 2.1 (2011), pp. 48–56.

[87] S Katayama et al. "Bicuspid Aortic Valves Undergo Excessive Strain During Opening: A Simulation Study." In: 145.6 (2013), pp. 1570–6.

[88] H Kim et al. "Dynamic Simulation of Bioprosthetic Heart Valves Using a Stress Resultant Shell Model." In: *Annals of Biomedical Engineering* 36 (2008), pp. 262–75.

[89] T Koch et al. "Aortic Valve Leaflet Mechanical Properties Facilitate Diastolic Valve Function". In: *Computer Methods In Biomechanics and Biomedical Engineering* 13.2 (2010), pp. 225–234.

[90] K Kolahi and M Mofrad. "Mechanotransduction: a Major Regulator of Homeostasis and Development". In: *Systems Biology and Medicine* 2.6 (2010), pp. 625–639.

[91] V Kouznetsova. "Computational Homogenization for the Multi-scale Analysis of Multi-phase Materials". PhD thesis. 2002.

[92] S Krucinski et al. "Numerical Simulation of Leaflet Flexure In Bioprosthetic Valves Mounted on Rigid and Expansile Stents". In: *Journal of Biomechanics* 26.8 (1993), pp. 929–943.

[93] G Kumar et al. "Design and Finite Element-based Fatigue Prediction of a New Self-expandable Percutaneous Mitral Valve Stent". In: *Computer-aided Design* 45.10 (2013), pp. 1153–1158.

[94] K Kunzelman, M Reimink, and R Cochran. "Annular Dilatation Increases Stress In the Mitral Valve and Delays Coaptation: a Finite Element Computer Model". In: *Cardiovascular Surgery* 5.4 (1997), pp. 427–434.

[95] M Labrosse et al. "Modeling Leaflet Correction Techniques In Aortic Valve Repair: A Finite Element Study." In: *Journal of Biomechanics* 44.12 (2011), pp. 2292–8.

[96] D Lasseux et al. "A Macroscopic Model for Species Transport During In Vitro Tissue Growth Obtained By the Volume Averaging Method". In: *Chemical Engineering Science* 59.10 (2004), pp. 1949–1964.

[97] N Latif et al. "Characterization of Molecules Mediating Cell-cell Communication In Human Cardiac Valve Interstitial Cells". In: *Cell Biochemistry and Biophysics* 45.3 (2006), pp. 255–264.

[98] R Leask, N Jain, and J Butany. "Endothelium and Valvular Diseases of the Heart". In: *Microscopy Research and Technique* 60.2 (2003), pp. 129–137.

[99] J Lee, D Courtman, and D Boughner. "The Glutaraldehyde-stabilized Porcine Aortic Valve Xenograft. I: Tensile Viscoelastic Properties of the Fresh Leaflet Material". In: *Journal of Biomedical Materials Research* 18.1 (1984), pp. 61–77.

[100] C Li, S Xu, and A Gotlieb. "The Progression of Calcific Aortic Valve Disease Through Injury, Cell Dysfunction, and Disruptive Biologic and Physical Force Feedback Loops". In: *Cardiovascular Pathology* 22.1 (2013), pp. 1–8.

[101] J Li, X Luo, and Z Kuang. "A Nonlinear Anisotropic Model for Porcine Aortic Heart Valves". In: *Journal of Biomechanics* 34.10 (2001), pp. 1279–1289.

[102] S Li and G Wang. *Introduction To Micromechanics and Nanomechanics*. World Scientific Publishing Company, 2008.

[103] L Lilly. *Pathophysiology of Heart Disease: a Collaborative Project of Medical Students and Faculty*. Lippincott Williams & Wilkins, 2012.

[104] A Liu, V Joag, and A Gotlieb. "The Emerging Role of Valve Interstitial Cell Phenotypes In Regulating Heart Valve Pathobiology". In: *The American Journal of Pathology* 171 (2007), pp. 1407–1418.

[105] H Liu, Y Sun, and C Simmons. "Determination of Local and Global Elastic Moduli of Valve Interstitial Cells Cultured on Soft Substrates." In: *Journal of Biomechanics* 46.11 (July 2013), pp. 1967–71.

[106] X Luo, W Li, and J Li. "Geometrical Stress-reducing Factors In the Anisotropic Porcine Heart Valves". In: *Journal of Biomechanical Engineering* 125.5 (2003), pp. 735–744.

[107] X Luo et al. "Multiscale Computation for Bioartificial Soft Tissues With Complex Geometries". In: *Engineering With Computers* 25.1 (2009), p. 87.

[108] Z Luo et al. "Intra-operative 2-d Ultrasound and Dynamic 3-d Aortic Model Registration for Magnetic Navigation of Transcatheter Aortic Valve Implantation". In: *Ieee Transactions on Medical Imaging* 32.11 (2013), pp. 2152–2165.

[109] D Malkus and T Hughes. "Mixed Finite Element Methods - Reduced and Selective Integration Techniques: A Unification of Concepts". In: *Computer Methods In Applied Mechanics and Engineering* 15.1 (1978), pp. 63–81.

[110] T Mansi et al. "An Integrated Framework for Finite-element Modeling of Mitral Valve Biomechanics From Medical Images: Application To Mitralclip Intervention Planning". In: *Medical Image Analysis* 16.7 (2012), pp. 1330–1346.

[111] C Martin and W Sun. "Simulation of Long-term Fatigue Damage In Bioprosthetic Heart Valves: Effects of Leaflet and Stent Elastic Properties". In: *Biomechanics and Modeling In Mechanobiology* 13.4 (2014), pp. 759–770.

[112] G Matalanis, W Shi, and P Hayward. "Correction of Leaflet Prolapse Extends the Spectrum of Patients Suitable for Valve-sparing Aortic Root Replacement". In: *European Journal of Cardio-thoracic Surgery* 37.6 (2010), pp. 1311–1316.

[113] MATLAB. *version 7.10.0 (R2010a)*. Natick, Massachusetts: The MathWorks Inc., 2010.

[114] A Mayne et al. "An Assessment of the Mechanical Properties of Leaflets From Four Second-generation Porcine Bioprostheses With Biaxial Testing Techniques." In: *The Journal of Thoracic and Cardiovascular Surgery* 98.2 (1989), pp. 170–180.

[115] W Merryman et al. "The Effects of Cellular Contraction on Aortic Valve Leaflet Flexural Stiffness". In: *Journal of Biomechanics* 39.1 (2006), pp. 88–96.

[116] C Miehe, J Schröder, and J Schotte. "Computational Homogenization Analysis In Finite Plasticity Simulation of Texture Development In Polycrystalline Materials". In: *Computer Methods In Applied Mechanics and Engineering* 171.3-4 (1999), pp. 387–418.

[117] J Min et al. "Diagnostic Accuracy of Fractional Flow Reserve From Anatomic Ct Angiography". In: *JAMA* 308.12 (2012), pp. 1237–1245.

[118] M Mofrad and R Kamm. *Cellular Mechanotransduction: Diverse Perspectives From Molecules To Tissues*. Cambridge University Press, 2009.

[119] H Mohammadi, F Bahramian, and W Wan. "Advanced Modeling Strategy for the Analysis of Heart Valve Leaflet Tissue Mechanics Using High-order Finite Element Method". In: *Medical Engineering and Physics* 31.9 (2009), pp. 1110–1117.

[120] E Mohler et al. "Bone Formation and Inflammation In Cardiac Valves". In: *Circulation* 103.11 (2001), pp. 1522–1528.

[121] C Morrey. "Quasi-convexity and the Lower Semicontinuity of Multiple Integrals". In: *Pacific Journal of Mathematics* 2.1 (1952), pp. 25–53.

[122] L Moura et al. "Rosuvastatin Affecting Aortic Valve Endothelium To Slow the Progression of Aortic Stenosis". In: *Journal of the American College of Cardiology* 49.5 (2007), pp. 554–561.

[123] D Mulholland and A Gotlieb. "Cardiac Valve Interstitial Cells: Regulator of Valve Structure and Function". In: *Cardiovascular Pathology* 6.3 (1997), pp. 167–174.

[124] J Nocedal and S Wright. *Numerical Optimization*. New York, NY: Springer Science & Business Media, 2006.

[125] B Nørgaard et al. "Diagnostic Performance of Noninvasive Fractional Flow Reserve Derived From Coronary Computed Tomography Angiography In Suspected Coronary Artery Disease: the Nxt Trial (analysis of Coronary Blood Flow Using Ct Angiography: Next Steps)". In: *Journal of the American College of Cardiology* 63.12 (2014), pp. 1145–1155.

[126] C Otto. *Calcification of Bicuspid Aortic Valves*. 2002.

[127] C Otto et al. "Characterization of the Early Lesion Of'degenerative'valvular Aortic Stenosis. Histological and Immunohistochemical Studies." In: *Circulation* 90.2 (1994), pp. 844–853.

[128] S Park, T Klein, and V Pande. "Folding and Misfolding of the Collagen Triple Helix: Markov Analysis of Molecular Dynamics Simulations." In: *Biophysical Journal* 93.12 (2007), pp. 4108–15.

[129] V Prot and B Skallerud. "Nonlinear Solid Finite Element Analysis of Mitral Valves With Heterogeneous Leaflet Layers". In: *Computational Mechanics* 43.3 (2009), pp. 353–368.

[130] E Rabkin et al. "Activated Interstitial Myofibroblasts Express Catabolic Enzymes and Mediate Matrix Remodeling In Myxomatous Heart Valves". In: *Circulation* 104.21 (2001), pp. 2525–2532.

[131] B Rahmani et al. "Manufacturing and Hydrodynamic Assessment of a Novel Aortic Valve Made of a New Nanocomposite Polymer". In: *Journal of Biomechanics* 45.7 (2012), pp. 1205–1211.

[132] N Rajamannan et al. "Human Aortic Valve Calcification Is Associated With An Osteoblast Phenotype". In: *Circulation* 107.17 (2003), pp. 2181–2184.

[133] S Raman et al. "Role of Aspartic Acid In Collagen Structure and Stability: A Molecular Dynamics Investigation." In: *The Journal of Physical Chemistry. B* 110.41 (2006), pp. 20678–85.

[134] M Rausch et al. "Mechanics of the Mitral Valve". In: *Biomechanics and Modeling In Mechanobiology* 12.5 (2013), pp. 1053–1071.

[135] J Rho, M Hobatho, and R Ashman. "Relations of Mechanical Properties To Density and Ct Numbers In Human Bone". In: *Medical Engineering & Physics* 17.5 (1995), pp. 347–355.

[136] M Sacks. "Incorporation of Experimentally-derived Fiber Orientation Into a Structural Constitutive Model for Planar Collagenous Tissues". In: *Journal of Biomechanical Engineering* 125.2 (2003), pp. 280–287.

[137] M Sacks. "The Biomechanical Effects of Fatigue on the Porcine Bioprosthetic Heart Valve". In: *Journal of Long-term Effects of Medical Implants* 11.3 (2001).

[138] M Sacks, D Smith, and E Hiester. "The Aortic Valve Microstructure: Effects of Transvalvular Pressure". In: *Journal of Biomedical Materials Research* 41.1 (1998), pp. 131–141.

[139] M Sacks and A Yoganathan. "Heart valve function: A Biomechanical Perspective". In: *Philosophical Transactions of the Royal Society B: Biological Sciences* 362.1484 (2007), pp. 1369–1391.

[140] R Salsas-Escat and C Stultz. "The Molecular Mechanics of Collagen Degradation: Implications for Human Disease". In: *Experimental Mechanics* 49.1 (2009), pp. 65–77.

[141] M Schmidt. *Minconf*. 2008. URL: `http://www.cs.ubc.ca/~schmidtm/Software/minConf.html`.

[142] F Schoen and R Levy. "Tissue Heart Valves: Current Challenges and Future Research Perspectives". In: *Journal of Biomedical Materials Research Part A* 47.4 (1999), pp. 439–465.

[143] P Schoenhagen et al. "In Vivo Imaging and Computational Analysis of the Aortic Root. Application In Clinical Research and Design of Transcatheter Aortic Valve Systems". In: *Journal of Cardiovascular Translational Research* 4.4 (2011), pp. 459–469.

[144] J Schroder and P Neff. "Invariant Formulation of Hyperelastic Transverse Isotropy Based on Polyconvex Free Energy Functions". In: *International Journal of Solids and Structures* 40.2 (2003), pp. 401–445.

[145] M Soncini et al. "Aortic Root Performance After Valve Sparing Procedure: a Comparative Finite Element Analysis". In: *Medical Engineering and Physics* 31.2 (2009), pp. 234–243.

[146] J Stella and M Sacks. "On the Biaxial Mechanical Properties of the Layers of the Aortic Valve Leaflet". In: *Journal of Biomechanical Engineering* 129.5 (2007), pp. 757–766.

[147] M Stevanella et al. "Mitral Leaflet Modeling: Importance of In Vivo Shape and Material Properties". In: *Journal of Biomechanics* 44.12 (2011), pp. 2229–2235.

[148] B Stewart et al. "Clinical Factors Associated With Calcific Aortic Valve Disease Fn1". In: *Journal of the American College of Cardiology* 29.3 (1997), pp. 630–634.

[149] D Stopak and A Harris. "Connective Tissue Morphogenesis By Fibroblast Traction: I. Tissue Culture Observations". In: *Developmental Biology* 90.2 (1982), pp. 383–398.

[150] C Sun and R Vaidya. "Prediction of Composite Properties From a Representative Volume Element". In: *Composites Science and Technology* 56.2 (1996), pp. 171–179.

[151] W Sun and P Lal. "Recent Development on Computer Aided Tissue Engineering: A Review". In: *Computer Methods and Programs In Biomedicine* 67.2 (2002), pp. 85–103.

[152] W Sun, C Martin, and T Pham. "Computational Modeling of Cardiac Valve Function and Intervention". In: *Annual Review of Biomedical Engineering* 16 (2014), pp. 53–76.

[153] W Sun and M Sacks. "Finite Element Implementation of a Generalized Fung-elastic Constitutive Model for Planar Soft Tissues". In: *Biomechanics and Modeling In Mechanobiology* 4.2-3 (2005), pp. 190–199.

[154] T Tadros, M Klein, and O Shapira. "Ascending Aortic Dilatation Associated With Bicuspid Aortic Valve: Pathophysiology, Molecular Biology, and Clinical Implications". In: *Circulation* 119.6 (2009), pp. 880–890.

[155] J Tan et al. "Cells Lying on a Bed of Microneedles: An Approach To Isolate Mechanical Force". In: *Proceedings of the National Academy of Sciences* 100.4 (2003), pp. 1484–1489.

[156] D Tang et al. "Two-layer Passive/active Anisotropic FSI Models With Fiber Orientation: MRI-based Patient-specific Modeling of Right Ventricular Response To Pulmonary Valve Insertion Surgery". In: *Molecular and Cellular Biomechanics* 4.3 (2007), p. 159.

[157] C Taylor, T Fonte, and J Min. "Computational Fluid Dynamics Applied To Cardiac Computed Tomography for Noninvasive Quantification of Fractional Flow Reserve: Scientific Basis". In: *Journal of the American College of Cardiology* 61.22 (2013), pp. 2233–2241.

[158] P Taylor et al. "The Cardiac Valve Interstitial Cell". In: *The International Journal of Biochemistry & Cell Biology* 35.2 (2003), pp. 113–118.

[159] R Taylor. *Feap - Finite Element Analysis Program*. 2014. URL: `http://www.ce.berkeley/feap`.

[160] M Thubrikar. *The Aortic Valve*. CRC press, 1989.

[161] M Thubrikar, J Aouad, and S Nolan. "Patterns of Calcific Deposits In Operatively Excised Stenotic Or Purely Regurgitant Aortic Valves and Their Relation To Mechanical Stress". In: *American Journal of Cardiology* 58.3 (1986), pp. 304–308.

[162] S Tzamtzis et al. "Numerical Analysis of the Radial Force Produced By the Medtronic-corevalve and Edwards-sapien After Transcatheter Aortic Valve Implantation (TAVI)." In: *Medical Engineering & Physics* 35.1 (2013), pp. 125–30.

[163] G Unnikrishnan, V Unnikrishnan, and J Reddy. "Constitutive Material Modeling of Cell: a Micromechanics Approach." In: *Journal of Biomechanical Engineering* 129.3 (June 2007), pp. 315–23.

[164] D Vader et al. "Strain-induced Alignment In Csollagen Gels". In: *Plos One* 4.6 (2009), e5902.

[165] I Vesely. "The Role of Elastin In Aortic Valve Mechanics". In: *Journal of Biomechanics* 31.2 (1997), pp. 115–123.

[166] I Vesely and R Noseworthy. "Micromechanics of the Fibrosa and the Ventricularis In Aortic Valve Leaflets". In: *Journal of Biomechanics* 25.1 (1992), pp. 101–113.

[167] E Votta et al. "Toward Patient-specific Simulations of Cardiac Valves: State-of-the-art and Future Directions". In: *Journal of Biomechanics* 46.2 (2013), pp. 217–228.

[168] G Walker et al. "Valvular Myofibroblast Activation By Transforming Growth Factor-β: Implications for Pathological Extracellular Matrix Remodeling In Heart Valve Disease". In: *Circulation Research* 95.3 (2004), pp. 253–260.

[169] H Wang, L Leinwand, and K Anseth. "Cardiac Valve Cells and Their Microenvironment: Insights From In Vitro Studies". In: *Nature Reviews Cardiology* 11.12 (2014), p. 715.

[170] N Weatherill and O Hassan. "Efficient Three-dimensional Delaunay Triangulation With Automatic Point Creation and Imposed Boundary Constraints". In: *International Journal for Numerical Methods In Engineering* 37.12 (1994), pp. 2005–2039.

[171] E Weinberg and M Kaazempur Mofrad. "A Multiscale Computational Comparison of the Bicuspid and Tricuspid Aortic Valves In Relation To Calcific Aortic Stenosis." In: *Journal of Biomechanics* 41.16 (2008), pp. 3482–7.

[172] E Weinberg and M Mofrad. "Transient, Three-dimensional, Multiscale Simulations of the Human Aortic Valve". In: *Cardiovascular Engineering* 7.4 (2007), pp. 140–155.

[173] E Weinberg, F Schoen, and M Mofrad. "A Computational Model of Aging and Calcification In the Aortic Heart Valve." In: *Plos One* 4.6 (2009), e5960.

[174] E Weinberg, D Shahmirzadi, and M Mofrad. "On the Multiscale Modeling of Heart Valve Biomechanics In Health and Disease." In: *Biomechanics and Modeling In Mechanobiology* 9.4 (2010), pp. 373–87.

[175] T Wynn and T Ramalingam. "Mechanisms of Fibrosis: Therapeutic Translation for Fibrotic Disease". In: *Nature Medicine* 18.7 (2012), p. 1028.

[176] C Xu et al. "A Novel Approach To In Vivo Mitral Valve Stress Analysis". In: *American Journal of Physiology-heart and Circulatory Physiology* 299.6 (2010), H1790–H1794.

[177] M Yacoub and L Cohn. "Novel Approaches To Cardiac Valve Repair: From Structure To Function: Part Ii". In: *Circulation* 109.9 (2004), pp. 1064–1072.

[178] K Yan, K Nair, and W Sun. "Three Dimensional Multi-scale Modelling and Analysis of Cell Damage In Cell-encapsulated Alginate Constructs". In: *Journal of Biomechanics* 43.6 (2010), pp. 1031–1038.

[179] C Yang et al. "Mri-based Patient-specific Computational Modeling of Right Ventricular Response To Pulmonary Valve Insertion Surgery: A Passive Anisotropic Fsi Model With Fiber Orientation". In: *Biomedical Engineering and Informatics, 2008. BMEI 2008. International Conference on*. Vol. 2. IEEE. 2008, pp. 160–167.

[180] Z Yang et al. "Determining Substrate Displacement and Cell Traction Fields: A New Approach". In: *Journal of Theoretical Biology* 242.3 (2006), pp. 607–616.

[181] C Yap et al. "Experimental Measurement of Dynamic Fluid Shear Stress on the Aortic Surface of the Aortic Valve Leaflet". In: *Biomechanics and Modeling In Mechanobiology* 11.1-2 (2012), pp. 171–182.

[182] C Yip and C Simmons. "The Aortic Valve Microenvironment and Its Role In Calcific Aortic Valve Disease". In: *Cardiovascular Pathology* 20.3 (2011), pp. 177–182.

[183] C Yip et al. "Calcification By Valve Interstitial Cells Is Regulated By the Stiffness of the Extracellular Matrix". In: *Arteriosclerosis, Thrombosis, and Vascular Biology* 29.6 (2009), pp. 936–942.

[184] J Yvonnet, D Gonzalez, and Q He. "Numerically Explicit Potentials for the Homogenization of Nonlinear Elastic Heterogeneous Materials". In: *Computer Methods In Applied Mechanics and Engineering* 198.33-36 (2009), pp. 2723–2737.

[185] J Yvonnet, E Monteiro, and Q He. "Computational Homogenization Method and Reduced Database Model for Hyperelastic Heterogeneous Structures". In: *International Journal for Multiscale Computational Engineering* 11.3 (2013).

[186] C Zarins, C Taylor, and J Min. "Computed Fractional Flow Reserve (CFFT) Derived From Coronary CT Angiography". In: *Journal of Cardiovascular Translational Research* 6.5 (2013), pp. 708–714.

[187] X Zeng and S Li. "Multiscale Modeling and Simulation of Soft Adhesion and Contact of Stem Cells". In: *Journal of the Mechanical Behavior of Biomedical Materials* 4.2 (2011), pp. 180–189.

[188] O Zienkiewicz and R Taylor. *The Finite Element Method: Solid Mechanics*. Vol. 2. Butterworth-heinemann, 2000.